

Titel

Defined Structured Cemented Carbide Tools for Abrasive Machining Processes

Dissertation

zur Erlangung des Grades
des Doktors der Ingenieurwissenschaften
der Naturwissenschaftlich-Technischen Fakultät
der Universität des Saarlandes

von

方诗琪
FANG Shiqi

Saarbrücken
2016

Tag des Kolloquiums: 15.12.2016
Dekan: Prof. Dr.-Ing. D. Bähre
Berichterstatter: Prof. Dr.-Ing. D. Bähre
Prof. Dr. C. Daul
Vorsitz: Prof. Dr.-Ing. G. Frey
Akad. Mitarbeiter: Dr.-Ing. F. Soldera
Weiteres Mitglied: Prof. E. Jiménez Piqué

Abstract

The challenge of this dissertation concerns the surface structuration of the WC-CoNi hardmetal with defined geometry, despite the fact that the embedded WC grains have irregular geometrical properties and distribution. An advanced method should be found and applied to structure the WC-CoNi hardmetal tool surface. The structured surfaces should be favorable and beneficial to reduce friction or to remove material in abrasive machining processes. Based upon the surface topography characterization of existing abrasive tools, e.g., CBN honing stone, geometrical properties of abrasives can be measured and quantified. The obtained geometrical information can contribute to the reproduction of the abrasive tool surface on WC-CoNi hardmetal. Laser surface texturing is an advanced machining method with high precision and it can effectively avoid some common thermal damage. Therefore, this method is implemented to machine WC-CoNi hardmetal surfaces. It is found that the structured WC-CoNi hardmetal tool can effectively remove material and improve surface quality of the counterpart (workpiece). These surface patterned hardmetal tools emerge then as potential alternative to conventional abrasive tools. Meanwhile, other patterns have also been produced on the hardmetals, and they can be used in the tribological system to reduce friction and improve wear resistance. It is a methodological and technical innovation to fabricate abrasive machining tools using laser to produce defined structures on a hardmetal surface, because it not only expands the utilization of hardmetal as an abrasive tool material but also enables the control and design of abrasive tool surface topography with high precision.

Kurzzusammenfassung

Die Herausforderung dieser Arbeit besteht in der geometrischen Strukturierung von WC-CoNi-Hartmetall-Oberflächen, wobei die eingebetteten WC-Körner geometrische unbestimmte Eigenschaften sowie zufällige Verteilungen aufweisen. Es sollen neue Methoden gefunden und angewendet werden, um WC-CoNi Hartmetallwerkzeugoberflächen zu strukturieren. Mit Hilfe dieser Strukturen soll die Reibung reduziert oder Material durch abrasive Bearbeitung gezielt abgetragen werden. Durch eine geeignete Charakterisierung der Oberflächentopographie vorhandener Abrasivwerkzeuge können die geometrischen Eigenschaften von abrasiven Körnern ermittelt und quantifiziert werden. Die erworbenen geometrischen Informationen können zur Reproduktion der Oberflächen von Abrasivwerkzeugen auf Hartmetalloberflächen genutzt werden. Die Laseroberflächenstrukturierung ist ein innovatives Bearbeitungsverfahren mit hoher Präzision und Effizienz. Diese Methode kann wirksam die üblichen thermischen Schäden vermeiden. Daher ist dieses Verfahren zur Bearbeitung von WC-CoNi Hartmetall vorteilhaft. Es konnte bestätigt werden, dass die neuartigen strukturierten WC-CoNi Hartmetallwerkzeuge die Materialien der Werkstücke abtragen und die Oberflächenqualität dieser verbessern. Diese oberflächenstrukturierten Hartmetallwerkzeuge können als potentielle Alternative zu konventionellen abrasiven Werkzeugen dienen. Parallel hierzu wurden weitere Strukturmuster auf Hartmetalloberflächen erzeugt. Die Strukturen können in einem tribologischen System angewendet werden, um Reibung zu reduzieren und Verschleißbeständigkeit zu verbessern. Die definiert erzeugten Strukturen können nicht nur bei Hartmetallen als Schleifwerkzeugmaterial eingesetzt werden, sondern ermöglichen auch eine gezielte Einstellung der Werkzeugoberflächentopographie.

Acknowledgment

The dissertation has been carried out in cooperation between the Institute of Production Engineering (LFT), Saarland University (Uds) and the Structural Integrity and Materials Reliability Center (CIEFMA), within the Materials Science and Metallurgical Engineering Department of Universitat Politècnica de Catalunya (UPC), in the framework of the European Joint Doctoral Program in Materials Science and Engineering (DocMASE) funded by the European Union's Erasmus Mundus Program. I wish to thank the European Commission for offering me the distinguished fellowship, covering my living expenses, academic research and business travel. My work has also received personal, material and financial support from the following institutions and academic bodies. Kadia GmbH, Saar Hartmetall, Werkzeug GmbH and ML Lubrication GmbH supplied the studying materials and some related equipment. Some important experiments have been conducted at the Chair of Functional Materials (FuWe), i.e. Material Engineering Center Saarland (MECS) in Uds, Photonik-Zentrum Kaiserslautern e.V., Centre for Research in Nano-engineering (Crne) in UPC, Fraunhofer IZFP Saarbrücken and Lehrstuhl für Materialwissenschaft und Werkstofftechnik (MWW) in Uds. Funding for experiments was also partly supplied by the Spanish MINECO (Grant No. MAT2015-70780-C4-3-P). DAAD (German Academic Exchange Service) and Gradus Program of Saarland University offered me financial support for some conference participations. I am grateful to the above institutions.

I wish to express my warm gratitude to my dissertation advisors: Prof. Dr.-Ing Dirk Bähre (Dean of Faculty 8 of Uds, Head of LFT) and Prof. Luis Llanes (Dean of Barcelona East School of Engineering and Senior Research Fellow at CIEFMA, UPC), not only for their distinguished academic and professional supervision, but also for their motivational and enthusiastic attitude towards life and work. I am convinced that figures and numbers are the best language for engineers and mastering research methods is somehow more meaningful than the research itself.

I wish to thank the colleagues in both institutes LFT and CIEFMA for their useful and critical advice pertaining to my doctoral pursuit and to the cultural integration, especially for their kind-hearted help when I settled down and started my research in Saarbrücken and Barcelona: Mr. Bernd Schmitt, Mr. Stefan Wilhelm, Mr. Alexander Ernst, Mr. Sven Klein, Mrs. Kirsten Trapp, Mrs. Nataliya Lyubenova, Mrs. Maria Cumbo, Mr. Romain Schieber, Dr. Yang Jing, Dr. Fernando Marro, Dr. Juan Roa, Dr. Jose Maria Tarrago and Ms. Erika Roitero. I wish also to thank my student assistants, graduate students, and interns for their contribution to my work and the nice time spent together with them: Mr. Steffen Gimmler, Mr. Jonas Hubertus, Mr. Yassine Afryad, Mr. Thomas Balaud, Mr. Saifeddine Bel Haj Khalifa and Mr. Loïc Mouelle.

Special gratitude should be given to Prof. Dr.-Ing Mücklich, head of FuWe. His institute FuWe is in charge of the DocMASE program management and offered me some important experimental installations. Some academic publications have been achieved in collaboration with the colleagues from FuWe: Prof. Dr.-Ing Carsten

Gachot (now Professor in the Vienna University of Technology), Dr.-Ing Andreas Rosenkranz, Dr.-Ing Flavio Soldera and Mr. Michael Engstler. Special gratitude should also be given to Dr. Thomas Herrmann from Photonik-Zentrum Kaiserslautern e.V., who gave me some cherished academic advice and offered me also some important experimental facilities. Dr. -Ing Micah Hodgins and Dr. Adam Yuile helped me a lot with English writing for some publications and with the dissertation revising. Their efficient work and thorough knowledge are appreciated.

Lastly and most importantly, I wish to thank my parents, my relatives and my friends. My gratefulness to them is beyond any words.

方诗琪
FANG Shiqi

二零一六年十月一日 于巴塞罗那
Barcelona, October 1, 2016

子曰：“博学之，审问之，慎思之，明辨之，笃行之。”

— 《中庸·哀公问政》

The Master [Confucius] said, "To this attainment there are requisite the extensive study of what is good, accurate inquiry about it, careful reflection on it, the clear discrimination of it, and the earnest practice of it."

- The duke Âi asked about government, *the Doctrine of the Mean* [1]

[1] The Doctrine of the Mean [Zhong Yong Chung Yung], attrib. to Confucius, trans. in Wing-Tsit Chan, *A Sourcebook in Chinese Philosophy*, (Princeton NJ: Princeton University Press, 1963), 95-115

Curriculum Vitae

方诗琪 FANG Shiqi

Born in Hunan, China, August 1987

Academic Qualifications

- | | |
|-------------------|--|
| Nov.2012-present | Ph.D., Institute of Production Engineering, Saarland University, Saarbrücken, Germany
Department of Materials Science and Metallurgical Engineering, Universitat Politècnica de Catalunya, Barcelona, Spain
(Fellowship, funded by ERASMUS MUNDUS DocMASE Program) |
| Aug.2010-Oct.2012 | M.Sc., Surface and Friction Engineering, Ecole Centrale de Lyon, Lyon, France
(Scholarship, funded by ERASMUS MUNDUS TANDEM Program) |
| Sep.2008-Jan.2009 | Exchange, Mechanical Engineering, National Taipei University of Technology, Taipei, Taiwan |
| Sep.2005-Jun.2010 | B.Sc. Mechanical Engineering, University of Science and Technology Beijing, Beijing, China
(Outstanding University Graduate of Beijing Municipality) |

Professional Experience

- | | |
|-------------------|--|
| Apr.2012-Oct.2012 | Industrial Internship, R&D, Danfoss Commercial Compressor, Reyrieux, France |
| Dec.2011-Mar.2012 | Laboratory Internship, Research Assistant, Tribology and System Dynamics Laboratory (LTDS), Ecully, France |
| Jul.2012-Aug.2011 | Industrial Internship, Production Services, Garlimard Perfumery, Grasse, France |

Contents

LIST OF ABBREVIATIONS	I
LIST OF SYMBOLS	III
LIST OF TABLES	VI
LIST OF FIGURES	VIII
1 INTRODUCTION	1
1.1 MOTIVATION	1
1.2 METHODOLOGY	3
2 STATE OF THE ART	5
2.1 OUTLINE OF STUDIED MATERIALS	5
2.1.1 Introduction of CBN composite and WC-CoNi hardmetal	5
2.1.2 Metallographic preparation of WC-CoNi hardmetal	6
2.1.3 Metallographic preparation of CBN composite.....	8
2.2 SIGNIFICANCE AND APPROACHES OF CBN COMPOSITE CHARACTERIZATION.....	9
2.3 APPROACHES OF HARDMETAL SURFACE MODIFICATION	12
2.3.1 Comparison of hardmetal surface modification methods: EDM and LST	12
2.3.2 Basics of laser surface texturing (LST) and its feasibility on hardmetal.....	13
2.4 EVALUATION AND TESTING OF PATTERNED TOOL SURFACES	16
2.4.1 Testing workbench for friction and abrasive testing	18
2.4.2 Nano-tribometer.....	20
2.4.3 Calowear test.....	21
3 TOOL MATERIAL CHARACTERIZATION	23
3.1 SURFACE TOPOGRAPHY QUANTIFICATION OF SUPER HARD ABRASIVE TOOLS (CBN COMPOSITE) IN 2D	23
3.1.1 Materials and assessment parameters	23
3.1.2 Experimental procedure	27
3.1.3 Results and discussion.....	29
3.1.4 Summary and conclusion	36
3.2 VOLUME QUANTIFICATION OF SUPER HARD ABRASIVE TOOLS (CBN COMPOSITE) IN 3D	37
3.2.1 Experimental procedures	37
3.2.2 Results and discussion.....	38
3.2.3 Summary and conclusion	41
3.3 COMPARISON OF THE TWO-DIMENSIONAL AND THE THREE-DIMENSIONAL QUANTIFICATIONS	42
4 TOOL SURFACE MODIFICATION	44
4.1 WC-CoNi HARDMETAL SURFACE MODIFICATION BY LST	44
4.1.1 WC-CoNi Hardmetal surface modification for tribological application.....	44
4.1.2 WC-CoNi Hardmetal surface modification for abrasive application	47
4.2 SURFACE INTEGRITY ASSESSMENT AFTER SURFACE MODIFICATION	50
4.2.1 Surface integrity assessment of the patterns for tribological application	51
4.2.2 Surface integrity assessment of the patterns for abrasive application.....	62

5	TOOL TESTING	72
5.1	TOOL TESTING FOR TRIBOLOGICAL APPLICATION	73
5.1.1	Friction tests on the workbench.....	73
5.1.2	Friction tests on Nano-tribometer	77
5.1.3	Wear tests on Calowear set-up	81
5.2	TOOL TESTING FOR ABRASIVE APPLICATION	87
5.2.1	Experimental parameters	87
5.2.2	Testing results and discussion	89
5.2.3	Noticeable observations	95
6	CONCLUSION AND PROSPECTIVE WORK	97
	REFERENCES	100

List of Abbreviations

2D	Two dimension
3D	Three dimension
AE	Area below the line of equality
AL	Area below the Lorenz curve
Al ₂ O ₃	Corundum
C	Diamond
CBN	Cubic boron nitride
CIEFMA	Structural Integrity and Materials Reliability Center (CIEFMA), within the Materials Science and Metallurgical Engineering Department of Universitat Politecnica de Catalunya (UPC)
Co	Cobalt
COF	Coefficient of friction
Crne	Centre for Research in Nano-Engineering in UPC
CT	Computed tomography
CVD	Chemical vapor deposition
DocMASE	European Joint Doctoral Program in Materials Science and Engineering
EDM	Electrical discharge machining
EDS	Energy-dispersive X-ray spectroscopy
FEPA	Federation of the European Producers of Abrasives
FIB	Focused ion beam
Fuwe	Chair of Functional Materials, Saarland University
L_L	Patterned & lubricated surfaces
L_NL	Patterned & non-lubricated surfaces
LFT	Institute of Production Engineering, Saarland University
LIMET	Laser-Interference Metallurgy

LIPPSSs	Laser-induced periodic surface structures
LSM	Laser scanning microscope
LST	Laser surface texturing
MECS	Material Engineering Center Saarland
MWW	Lehrstuhl für Materialwissenschaft und Werkstofftechnik, Saarland University
Ni	Nickel
ns-/ps-/fs-	Nano-second/pico-second/femto-second
P_L	Polished & lubricated surfaces
P_NL	Polished & non-lubricated surfaces
PRF	Pulse repetition frequency
PVD	Physical vapor deposition
SEM	Scanning electron microscope
SiC	Silicon carbide
TFC	Tangential force coefficient
WC	Tungsten carbide
WC-CoNi	Cobalt-nickel based cemented tungsten carbide hardmetal
W-EDM	Wire electrical discharge machining
WLI	White light interferometer

List of Symbols

Symbol	Explanation	Unit
a_1	Bottom side length of the hexagonal pyramid	μm
a_2	Top side length of the hexagonal pyramid	μm
b	Wear crater diameter	μm
∂b	Boundary of the grain	
D	Particle density	mm^{-2}
d	Ball diameter	mm
d_1	Interval between two adjacent hexagonal pyramids along the X-axis	μm
d_2	Interval between two adjacent hexagonal pyramids along the Y-axis	μm
ds	Surface element of the grain	
D_{eq}	Equivalent spherical diameter of grains	μm
$F_{(i)}$	Cumulative share of components of the system	%
f, f_1, f_2, f_3	Shape factor	
$F_{\text{max}}/F_{\text{min}}$	Max/min Feret diameter	μm
\bar{F}	Mean Feret diameter	μm
f_b	Binder volume fraction	%
f_g	Grain volume fraction	%
F_n	Normal force along the X-axis	N
F_o	Oscillation force along the Z-axis	N
F_t	Tangential force along the Y-axis	N
H	Homogeneity	%
h	Height the hexagonal pyramid	μm
$H_{(\text{Object number})}$	Homogeneity of object number	%
$H_{(\text{Phase amount})}$	Homogeneity of phase amount	%

h_R	Region homogeneity	%
K_c	Convexity	
K	Wear rate	$\mu\text{m}^2/\text{N}$
L	Sliding distance	mm
$L_{(i)}$	Cumulative share of the values of the attribute	%
M	Integral of mean curvature of grains	mm^{-2}
N_t	Grain amount	
P	Calculated periodicity	μm
$1/r_1(s), 1/r_2(s)$	Minimum and maximum curvature at the surface element ds of the grain	
R_a	Arithmetical mean deviation	μm
R_{max}	Maximum peak-to-valley roughness	μm
r_p	Phase fraction	%
R_z	Average peak-to-valley profile roughness	μm
S	Surface area	μm^2
S_1	Bottom surface area of the hexagonal pyramid	μm^2
S_2	Top surface area of the hexagonal pyramid	μm^2
S_g	Grain section	μm^2
\overline{S}_g	Mean grain surface	μm^2
S_s	Total surface area	μm^2
S_t	Total grain sections	μm^2
U	Particle perimeter	μm
V	Grain volume	μm^3
V_b	Total binder volume	μm^3
V_c	Convex particle perimeter	μm
V_g	Total grain volume	μm^3
\overline{V}_g	Mean grain volume	μm^3

V_s	Specimen volume	μm^3
v_x	Laser beam speed along X-axis	mm/s
v_y	Laser beam speed along Y-axis	mm/s
α	Slope at the measuring position A-A	°
β	Slope at the measuring position B-B	°
θ	Angle between two sub laser beams	°
λ	Laser wavelength	nm
ν	Kinematic viscosity	mm^2/s
π	Pi: ratio of a circle's circumference to its diameter	

List of Tables

Table 1-1: Equipment list.....	3
Table 2-1. Microstructural properties of the honing stones B151/L2/10/50 and B91/128/x44/35	6
Table 2-2. Properties of the WC-CoNi hardmetal VN77	6
Table 2-3. Metallographic processing program for VN77 specimens	8
Table 2-4. Metallographic processing program for CBN composites.....	9
Table 2-5: Variables and invariables of input parameters and their effects	18
Table 2-6. Chemical composition of 20MnCr5	19
Table 2-7: Variables and invariables of input parameters for Calowear test	22
Table 3-1. Features of the LSM Olympus Lext OLS3100	23
Table 3-2. Quantitative parameters.....	24
Table 3-3. Dimensional parameters	24
Table 3-4. Form parameters.....	25
Table 3-5. Shape factor as a function of the corresponding geometries	26
Table 3-6. Positional parameters	26
Table 3-7. Quantitative results of the honing stones.....	30
Table 3-8. Mean values of the dimensional parameters	31
Table 3-9. Grain region homogeneities of B151 and B91	36
Table 3-10. Microstructural information of the B151 specimen.....	39
Table 3-11. Geometrical properties of the B151 grains	39
Table 3-12. Grain shape classification of the B151 specimen	41
Table 4-1. Summary of the produced patterns and corresponding laser configurations	44
Table 4-2. Parameters of the ns-laser setup for the production of the line-like patterns	45
Table 4-3. Experimental parameters of the ns-laser setup for the pattern geometry.....	46
Table 4-4. Laser parameters used for the production of dimples.....	46
Table 4-5. Motion control parameters for the production of dimples.....	46
Table 4-6. Motion control parameters for the production of grooves	47
Table 4-7. Quantification of the honing stone B151 and surface topography design of the WC-CoNi hardmetal sample	48
Table 4-8 Geometrical design of the hexagon pyramids.....	49

Table 4-9. Geometrical properties of single square pyramid	50
Table 4-10. Surface topography design of the sample with the square pyramids	50
Table 4-11. Geometrical property measurements of the dimples produced by ps-laser	53
Table 4-12. Geometrical property measurements of the grooves produced by ps-laser	58
Table 4-13. Summary of geometrical property measurements of the produced hexagonal pyramids .	64
Table 4-14. Summary of geometrical property measurements of the produced square pyramids	70
Table 4-15. Geometrical property comparison of the produced pyramids	70
Table 5-1. Tool testing of different surface patterns for determined applications	72
Table 5-2. Machining parameters set for the workbench	73
Table 5-3. Lubricants used in the experiments	73
Table 5-4. Roughness requirement of pre-machined workpiece	73
Table 5-5. COFs obtained in each friction test on the workbench	74
Table 5-6. Values of COFs obtained in each friction test on the workbench	76
Table 5-7. Nano-tribometer configuration.....	78
Table 5-8: Average COFs of the friction tests on Nano-tribometer	78
Table 5-9. Calowear test instrument configuration.....	81
Table 5-10. Measurement results on the polished and patterned surfaces	83
Table 5-11. Calowear test instrument configuration.....	84
Table 5-12. Measurement results on the polished and patterned surfaces	84
Table 5-13. Machining parameters and workbench configuration	88
Table 5-14. Quantification of the hardmetal tool	89
Table 5-15. Roughness measurements of workpiece 1 and workpiece 2 before testing	89
Table 5-16. Roughness measurement of workpiece 1 and workpiece 2 after testing	90
Table 5-17. TFCs obtained with different tools.....	92
Table 5-18. Summary of geometrical properties of the hexagonal pyramids after tests.....	94
Table 5-19. Comparison of geometrical properties	95

List of Figures

Figure 1-1. Basic task division of the dissertation	2
Figure 2-1. Composite materials: (a) CBN composite surface (SEM), (b) polished WC-CoNi hardmetal surface (SEM).....	5
Figure 2-2. (a) VN77 specimen production using W-EDM, (b) dimension of the produced VN77 specimen with curved top surface	7
Figure 2-3. VN77 specimen shaped by W-EDM: (a) surface inspection by SEM, (b) FIB cross-section	8
Figure 2-4. B151 specimen surface inspection by LSM (a) before polishing and (b) after polishing	9
Figure 2-5. Microstructural assembly of composite materials used to fabricate super hard abrasive tools: (a) schematic illustration and cross-section, (b) SEM image showing a typical surface aspect of a CBN honing tool; (c) SEM image of polished surface of CBN honing tool B151; and (d) LSM image of a single monocrystalline CBN grain	10
Figure 2-6. Schematic illustration of laser cavity	14
Figure 2-7. Influencing factors of surface patterns produced by LST	15
Figure 2-8. Causes and influencing factors of the tangential force coefficient (TFC)	17
Figure 2-9. (a) Workbench for abrasive machining processes, (b) dynamics in the abrasive machining process	19
Figure 2-10. (a) Testing counterpart, (b) geometrical properties of the testing counterpart	19
Figure 2-11. (a) Nano-tribometer set-up, (b) dynamics of the Nano-tribometer.....	20
Figure 2-12. (a) Calowear test instrument, (b) kinematics of the Calowear test	21
Figure 3-1. Assessment parameters of surface topography quantification	23
Figure 3-2. Schematic illustration of dimensional perimeters.....	25
Figure 3-3. Schematic illustration of grain orientation	26
Figure 3-4. Schematic illustration of homogeneity (e.g., object number).....	26
Figure 3-5. Example (10 parts of the honing stone B91) of surface sectioning and assembly by LSM	28
Figure 3-6. LSM images of B151 surface: (a) before segmentation, (b) after segmentation	28
Figure 3-7. Common errors and correction in the image processing: examples of (a) no default, (b) pore, and (c) adhesion.....	29
Figure 3-8. (a) B151 and (b) B91 grain distribution after image digital processing	30
Figure 3-9. Grain sections of (a) B151 and (b) B91	31
Figure 3-10. Grain convexity of (a) B151 and (b) B91	31
Figure 3-11. Grain convex perimeter of (a) B151and (b) B91	32

Figure 3-12. Feret diameters of B151 and B91: (a) F_{\max} of B151, (b) F_{\max} of B91, (c) F_{\min} of B151, (d) F_{\min} of B91	32
Figure 3-13. Typical grain shapes of CBN honing tools (B151): (a) elongated, (b) triangle, (c) rectangle, (d) square, (e) ellipse, (f) pentagon, (g) circular	34
Figure 3-14. Shape factor histograms of (a) B151 and (b) B91	35
Figure 3-15. Grain orientation distribution of (a) B151 and (b) B91	35
Figure 3-16. Lorenz curves of (a) B151 and (b) B91 region homogeneities	36
Figure 3-17. Procedure of volume reconstruction and 3D characterization	37
Figure 3-18. Cross sectional image of CBN composite obtained by CT scan	38
Figure 3-19. Grain segmentation of the specimen: (a) cross-section image of the reconstructed 3D model, (b) grain distribution in the 3D model.....	38
Figure 3-20. (a) Grain amount distribution and (b) volume fraction: distribution as a function of equivalent spherical diameter.....	39
Figure 3-21. (a) Basic grain shape definitions, (b) grain shape classification using shape factors	41
Figure 4-1. (a) Experimental configuration and (b) schematic illustration of LIMET for production of laser interference structure.....	45
Figure 4-2. (a) High precision 5-axis laser micromachining system (GL.5, GFH GmbH, http://www.photonik-zentrum.de), (b).fs-laser set-up with the auto stage, and laser trajectory configurations for the production of (c) dimples and (d) grooves	47
Figure 4-3. (a) Schematic illustration of pyramid production using ultra-short pulse laser beams, (b) geometrical design of single hexagonal pyramid	48
Figure 4-4. (a) Array arrangement of the square pyramids on the hardmetal surface, (b) geometrical design of single square pyramid.....	50
Figure 4-5. (a) LSM image and (b) cross-sectional plots of the line-like pattern.....	51
Figure 4-6. Microstructural investigation of the line-like surface pattern: (a) overview, (b) cross-section, (c) enlarged view of the cross-section, (d) induced defects, (e) FIB cross-section, (f) enlarged view of the FIB cross-section.....	52
Figure 4-7. LSM images and cross-sectional plots of geometrical properties of surface patterns: (a) arrangement, (b) single dimple, (c) cross section, (d) geometric characterization	53
Figure 4-8. Microstructural investigation of the dimples: (a) overview, (b) transition zone, (c) enlarged view of the processed zone, (d) FIB cross-section, (e) enlarged view in the transition zone, (f) enlarged view in the processed zone	54
Figure 4-9. Patterned dimples by ultra-short pulsed laser processing on the WC-CoNi surface: (a) arrangement, (b) cross-section.....	56
Figure 4-10. Surface integrity investigation of dimples (SEM): (a) overview, (b) non-affected zone, (c) transition zone, (d) processed zone	56
Figure 4-11. Grooves produced on the surface of the WC-CoNi hardmetal sample using ps-laser: (a) horizontal grooves (LSM), (b) and (c) geometric properties (SEM)	57

Figure 4-12. Surface integrity assessment of produced grooves (SEM): (a) overview, (b) processed zone, (c) transition zone (d) non-affected zone	59
Figure 4-13. FIB cross sectional analysis of produced grooves: (a) cross section, (b) processed zone, (c) transition zone and (d) zoomed processed zone	60
Figure 4-14. (a) LSM image and (b) cross-sectional plots of the groove produced by fs-laser	61
Figure 4-15. Microstructural investigation of the grooves produced by fs-laser: (a) overview, (b) enlarged view of the processed zone, (c) FIB cross-section, (d) enlarged view of the FIB cross-section	61
Figure 4-16. Surface inspection of CBN honing stone B151: (a) grain distribution, (b) single CBN grain on the surface; geometrical properties of hexagonal pyramids: (c) arrangement of produced hexagonal pyramids, (d) single hexagonal pyramid (images taken by SEM)	62
Figure 4-17. Surface topography reconstruction using Origin 9.0: (a) and (c) arrangement and projection of produced hexagonal pyramids, (b) and (d) single hexagonal and its projection	63
Figure 4-18. (a) Projection of a single hexagonal pyramid, (b) and (c) cross-section views at positions A-A and B-B, respectively.....	64
Figure 4-19. Comparison of aimed and experimentally attained surface topography features: (a) interval between adjacent pyramids; (b), (c) and (d) geometrical parameters of a single hexagonal pyramid	65
Figure 4-20. Pattern morphology (SEM): (a) pyramid top and slope, (b) pyramid bottom	65
Figure 4-21. Cross sectional investigation of the hexagonal pyramid: (a) cross section position, (b) pyramid top, (c) pyramid bottom, (d) Oxidation layer, (e) EDS analysis of oxidation layer.....	66
Figure 4-22. Morphological characterization of square pyramids by SEM: (a) arrangement of produced square pyramids, (b) single square pyramid	68
Figure 4-23. (a) 3D model reconstruction of square pyramid and (b) its projection.....	68
Figure 4-24. (a) Cross sections of the 3D model of the single square pyramid, (b) and (c), cross-sections at position A-A and B-B.....	69
Figure 4-25. Comparison of the geometrical properties between the design and the measurements: (a) interval between the adjacent grains, (b) side lengths and height, (c) surface area and (d) slope angles	69
Figure 4-26. Phase ratio comparison between the design and measurement: (a) hexagonal pyramids and (b) square pyramids.....	70
Figure.5-1. (a) Analysis of the COF for line-like patterns and dimples as a function of the normal loads, (b) schematic diagram of the line-like pattern interfaces, (c) schematic diagram of the lubrication microcirculation and the interfacial reaction in the dimples	75
Figure 5-2. (a) COFs as a function of normal loads for all tested specimens, interfacial reactions of (a) rough surface, (b) polished surface, (c) surface with dimples.....	77
Figure 5-3. Evolutions of COFs for each type of surface patterns as a function of the slide laps	79
Figure 5-4. COF evolution as a function of slide laps: (a) comparison between polished and patterned surfaces in the non-lubricated case, (b) comparison between polished and patterned surfaces in the lubricated case	80

Figure 5-5. COF evolution as a function of slide laps: (a) comparison on lubricants for polished surfaces, (b) comparison on lubricants for patterned surfaces	80
Figure 5-6. Wear crater evolution as a function of sliding cycles on the surfaces with different patterns: (a) polished surfaces, (b) line-like patterns	82
Figure 5-7. Calowear test results of polished surface and line-like patterns: (a) diameter (D) vs. sliding cycles, (b) wear rate (K) vs. sliding cycles	83
Figure 5-8. Calowear test results of polished and patterned surfaces with/without lubricant: (a) diameter (d) vs. sliding cycles, (b) wear rate (K) vs. sliding cycles	85
Figure 5-9. SEM investigation of wear craters produced on different surfaces and under different conditions: (a) polished and non-lubricated, (b) polished and lubricated, (c) patterned and non-lubricated, (d) patterned and lubricated.....	86
Figure 5-10. Flow chart of the test procedure	87
Figure 5-11. Profile of (a) one single hexagonal pyramid on the WC-CoNi hardmetal tool, (b) one single CBN grain on the honing stone B151 (images taken by LSM)	88
Figure 5-12. Surface characterization (LSM) and profiles of (a) workpiece 1, (b) workpiece 2	89
Figure 5-13. Surface characterizations after testing (LSM): (a) workpiece 1, (b) workpiece 2	90
Figure 5-14. Roughness improvement of the workpieces: (a) Workpiece 1 machined by the honing stone B151, (b) Workpiece 2 machined by the hardmetal tool	90
Figure 5-15. Cutting force signal record of one test: (a) workpiece 1 machined by the honing stone B151, (b) workpiece 2 machined by the hardmetal tool	91
Figure 5-16. Cutting force and TFC evolution: (a) workpiece 1 machined by the honing stone B151, (b) workpiece 2 machined by the hardmetal tool	92
Figure 5-17. Comparison of TFC mean values	92
Figure 5-18. Hexagonal pyramids characterized by (a) LSM and (b) SEM after testing	93
Figure 5-19. Pyramid reconstruction after machining using Origin 9.0: (a) reconstructed 3D model and (b) its projection	93
Figure 5-20. (a) Projection of a single hexagon pyramid, (b) and (c) cross-sections at position A-A and B-B, respectively.....	94
Figure 5-21. Comparison of the geometrical properties of the hexagonal pyramids before and after machining: (a) side lengths and height, (b) surface area, (c) slope angles and (d) height evolution....	95

1 Introduction

1.1 Motivation

Tools for abrasive processes are usually composed of abrasive grains, such as aluminum oxide, carbon silicide, cubic boron nitride (CBN) or diamond, and the binder. Abrasive grains serve to remove material of the counterparts and also have a high wear resistance concerning friction. However, due to the production processes, a contingent statistical allocation of single grains appears at the tool surfaces, which can lead to instabilities and interferences in the tool applications. For instance, the tool used in the long-stroke honing processes consists of a honing stone and a guiding stone, and both of them are usually diamond or CBN composites. The honing stone serves to remove materials and the guiding stone, which is positioned between the tool's rotating axis and workpiece, serves as a support part to maintain the rotating axis. However, the diamond or CBN composites are expensive materials and the statistical distribution of abrasive grains in the matrix can lead to inhomogeneities at the tool surfaces. In considering the application requirements, ideal tools for abrasive machining processes should possess the following features:

- combining adequate hardness and toughness;
- homogenous and stable behavior properties;
- enough surface wear resistance;
- and low cost.

The production of defined surface structures on hard, tough and wear-resistant material can be a new possible concept in designing and producing supporting parts or cutting tools for abrasive processes. One possible material group is cemented carbides, which are wear-resistant, refractory materials made up of small carbide particles embedded in a metallic binder. This structure combines hardness and wear resistance of the ceramic particles with the toughness of the metallic binder, giving the material an exceptional combination of hardness, toughness and wear resistance. Cemented carbide can not only meet the requirements as a cutting tool material, but also reduces the costs compared to diamond or CBN composites. Laser surface texturing (LST) is implemented to produce defined structures on the cemented carbide, which is an effective method to improve the interface functions and enrich the applications of the surfaces.

This dissertation focuses on the surface modification of a WC-base cemented carbide, materials also referred in practice as hardmetals, with CoNi metallic binder (WC-CoNi). The goal is to produce certain patterns on the surfaces of WC-CoNi hardmetal as support part for the tribological application, as well as to use WC-CoNi hardmetal as an alternative material to reproduce similar surface features of existing abrasive tools (e.g., honing stones) for the abrasive application, aiming towards utilization of these materials for honing-like service conditions.

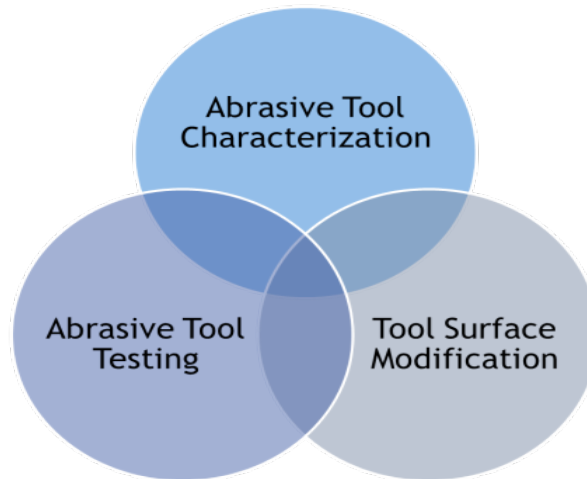


Figure 1-1. Basic task division of the dissertation

Based on the aforementioned considerations, the main work can be divided into three main aspects (Figure 1-1):

Abrasive tool characterization: find out a reproducible approach to describe and quantify surface topography of existing abrasive tools in order to offer necessary information for the reproduction of similar surface features on the WC-CoNi hardmetal surface.

Tool surface modification: produce defined structures on WC-CoNi hardmetal surfaces for the tribological application and also for the abrasive application.

Abrasive tool testing: evaluate the performances of produced surface topography with defined structures, including frictional test, cutting test, and surface integrity assessment according to surface applications.

In this study, two different honing stones B151/L2/10/50 (B151) and B91/128/x44/35 (B91) as well as a WC-CoNi hardmetal grade are selected as studied materials. Surface topography quantification is conducted to characterize the geometrical properties of single grains of CBN honing stones B151 and B91. Advanced volume characterization is also carried out for the honing stone B151, aiming to obtain more precise structural properties. The obtained geometrical properties of the grains are useful and applicable for the reproduction of the honing stone surface topography on the WC-CoNi hardmetal surface. Hence, convex structures, i.e. regular arrays of hexagonal and square pyramids, are sculpted from hardmetal surfaces using laser machining, particularly considering the pyramids are similar to CBN grains regarding the geometrical properties. Some concave structures, i.e. line-like patterns, dimples and grooves, are also produced using laser, aiming towards the application of these hardmetals for support parts in the tribological system. Once aimed surface topography is shaped, geometrical features of the surface patterns are measured and resulting surface integrity is assessed. The performance of the hardmetal tools with the patterned surfaces is tested and validated by means of an in-house built bench test-

ing unit, which is designed to simulate an abrasive machining process similar to the honing process.

1.2 Methodology

Different methods and equipment are applied for the material characterization, surface modification and tool testing. The equipment (Table 1-1) includes:

- 1) devices for material characterization such as metallographic microscope, laser scanning microscope (LSM), scanning electron microscope (SEM), focused ion beam (FIB), white light interferometer (WLI), computed tomography (CT) and perthometer;
- 2) equipment for surface modification such as Nd:YAG nanosecond laser, Nd:YVO₄ picosecond laser and Ti:Sapphire femtosecond laser;
- 3) devices for tool testing such as Calowear set-up, Nano-tribometer and In-house build test bench.

Other devices such as wire-electrical discharge machining (W-EDM) center, 3D printer and Vickers hardness testing machine are also involved for certain applications.

Table 1-1: Equipment list

Tasks	Experimental equipment	Specification
Specimen production	W-EDM center Metallographic lab	
Abrasive tool material characterization	Laser scanning microscope Computed tomography Vickers hardness tester Metallographic lab	Olympus Lext OLS3100
Tool surface modification	Nd:YAG nanosecond laser Nd:YVO ₄ Picosecond laser Ti:Sapphire femtosecond laser Laser scanning microscope	Spectra Physics Quanta Ray Pro 290 HYPER25 Coherent Kaiserslautern GmbH GL.5, GFH GmbH Spitfire, Newport Spectra Physics Olympus Lext OLS3100
Tool testing	Calowear machine Nano-tribometer In-house build test bench 3D printer SEM/FIB Metallographic microscope white light interferometer Perthometer	CSM instrument Calowear CSM Instruments Dual-Beam-Workstation (Strata DB 235, FEI) and Dual-Beam-Workstation (Helios 600, FEI) with FIB, SEM, EDS, EBSD and STEM

Surface features of abrasive tools can be measured by LSM, and the following image digital processing can quantify geometric features of the abrasives. CT is used to obtain precise microstructural information of the studied materials.

Surface modification is essential in this project. Short and ultra-short pulse lasers are used to produce surface topography with defined structures in order to improve surface functional properties, since this non-conventional technique for high precision machining is fast, clean, efficient, and especially capable to reduce common thermal defects. Surface modification with defined structures is supposed to be an extension to the use of cemented carbides.

The geometrical precision of the produced surface patterns and structures is investigated and their surface integrity is assessed by SEM and FIB. The tribological tests as well as abrasive testing are consequently performed using the in-house build test bench. For certain patterns, frictional tests and wear tests are also conducted on the nano-tribometer and Calowear set-up.

2 State of the art

2.1 Outline of studied materials

2.1.1 Introduction of CBN composite and WC-CoNi hardmetal

Composite materials are nowadays widely used in the tool fabrication industry. The materials, containing two basic components (abrasive grains and binder), are used to manufacture different sorts of cutting tools. The tools can be used as abrasive tools or chip-removal tools. For the abrasive tools, abrasives are mostly Corundum (Al_2O_3), Silicon carbide (SiC), Diamond (C) or Cubic boron nitride (CBN) (Figure 2-1(a)) [1]. CBN is the second hardest substance after diamond. In the manufacturing processes, the structure of boron nitride is transformed from hexagonal to cubic under high temperature and pressure. The formed cubic crystalline lattice is similar to that of diamond and offers high hardness [2-4]. However, CBN has better wear resistance and thermal conductivity compared with diamond, especially its high melting temperature allows CBN to have wider applications than diamond [2]. In practice, CBN composite is often used as cutting tool materials for abrasive machining processes in industry such as grinding and honing. The composite can also be used in some harsh conditions such as high temperature or high speed cutting [5,6]. Dimensions of CBN abrasives can vary from some micrometers to some hundred micrometers. The binder of the composite can be metallic, resin or ceramic. In this dissertation, the CBN composite B151/L2/10/50 (B151) has been studied, and the CBN composite B91/128/x44/35 (B91) is also studied for some cases as a comparison. Both of the composites B151 and B91 are used as honing stones.

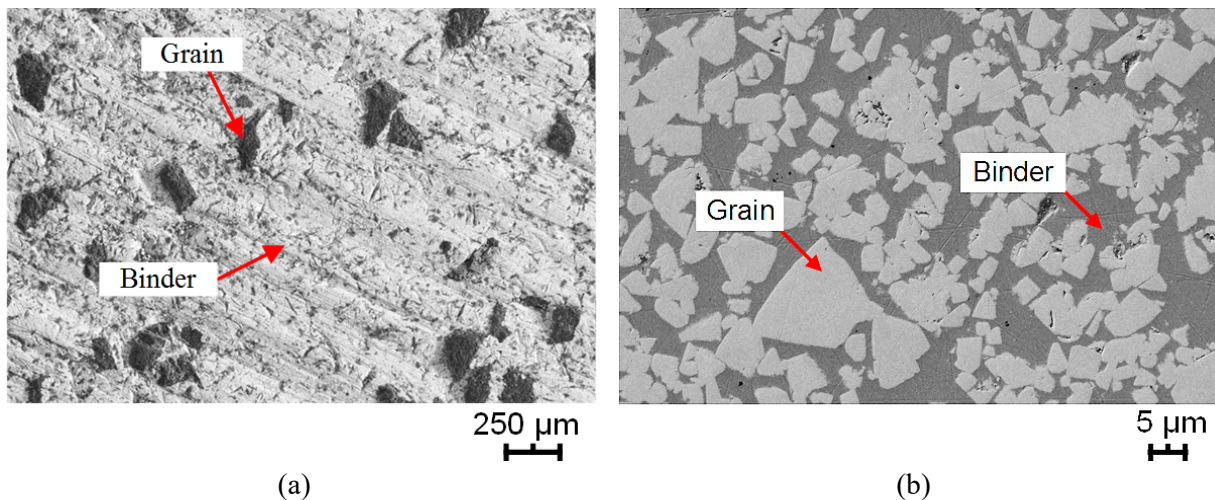


Figure 2-1. Composite materials: (a) CBN composite surface (SEM), (b) polished WC-CoNi hardmetal surface (SEM)

The specifications of honing stones offer the information about the materials from what it is made, such as abrasive nature, grain size, crystal type, binder and grain concentration [7]. According to the Federation of the European Producers of Abrasives (FEPA) standard, which is used to identify the Diamond and CBN honing stones, grains are classified in terms of the mesh width in micrometers (μm) [8].

Grain concentration is defined as the grain amount per one cm^3 in the cutting layer [9]. The specification of the honing stone B151/L2/10/50 (Table 2-1) indicates that abrasive nature is cubic boron nitride (B), grain size is between 126 μm and 150 μm (151), crystal type and binder materials (L2 and 10 respectively), and grain concentration of 12.5 vol-% i.e. about 0.44 g/cm^3 (50) [10]. The CBN grains have a monocrystalline structure, which can form sharp cutting edges in the cutting processes due to its self-generating nature. The Cu/Sn/Co/Ag alloy is used as the binder. The properties of B91/128/x44/35 are also shown in Table 2-1.

Table 2-1. Microstructural properties of the honing stones B151/L2/10/50 and B91/128/x44/35

Honing Stone	Mean grain size (μm)	Max. grain size (μm)	Min. grain size (μm)	Grain concentration (vol-%)	Density (g/cm^3)
B151	138	150	126	12.5	0.44
B91	83	90	76	8.75	0.31

WC-CoNi hardmetal is composite of tungsten carbide (hard phase) and cobalt/nickel (binder) (Figure 2-1(b)), which is usually sintered and formed under high pressure and temperature in a vacuum chamber. The size of WC grains can vary from 0.5 μm to 30 μm and imbedded in the metallic binder. The shape of WC grains is mainly triangle or rectangle. The structure of WC-CoNi hardmetal can be dense or coarse [11]. This structure combines the hardness and wear resistance of the carbide grains with the toughness of the metallic binder. From the structural point of view, WC-CoNi hardmetal has similar microstructure as the aforementioned CBN composite. Therefore, both of them are used as cutting tool materials. Although the hardness of WC is less than CBN, hardmetal is still able to machine most steels due to its adequate hardness and toughness. Hardmetal is often shaped by electron discharge machining (EDM) [12], and is applied as forefront materials in engineering, especially in tooling applications, such as chip removal cutting tool materials for metal cutting, mining, rock drilling, metal forming, structural components and wear parts [13-15].

The WC-CoNi hardmetal VN77 has been selected as the studied material. This hardmetal has a grain size of 20 μm and contains 14 wt% Cobalt and 14 wt% Nickel as binder (Table 2-2). The material is characterized by large grain size and low hardness in the hardmetal family.

Table 2-2. Properties of the WC-CoNi hardmetal VN77

Material	WC-Grain Size (μm)	Co (wt.%)	Ni (wt.%)	Density (g/cm^3)	Hardness (HV30)
VN77	20	14	14	12.82	610

2.1.2 Metallographic preparation of WC-CoNi hardmetal

Hardmetal is difficult to be machined by traditional chip-removal shaping methods due to its high hardness. Electrical discharge machining (EDM) can be employed as surface treatment method to machine the material surfaces on the micro scale. During the EDM process, a great number of tiny materials are individually removed due

to the electrical discharges between the two electrodes, which finally result in homogenous large material removal. The accuracy of this method is fairly high compared with the traditional chip-removal method [12].

In this work, specimens of VN77 have been produced using wire electrical discharge machining (W-EDM). Figure 2-2(a) illustrates that the specimen is shaped by W-EDM from a piece of raw material. Two different types of specimens have been produced. Both of them are basically rectangular cuboid with the dimension of $20 \times 3 \times 4.95 \text{ mm}^3$. The first type has a flat top surface, whereas the second type has a top surface with radius of 12.5 mm in order to adapt to the workpiece profile in the tool testing (Figure 2-2(b)).

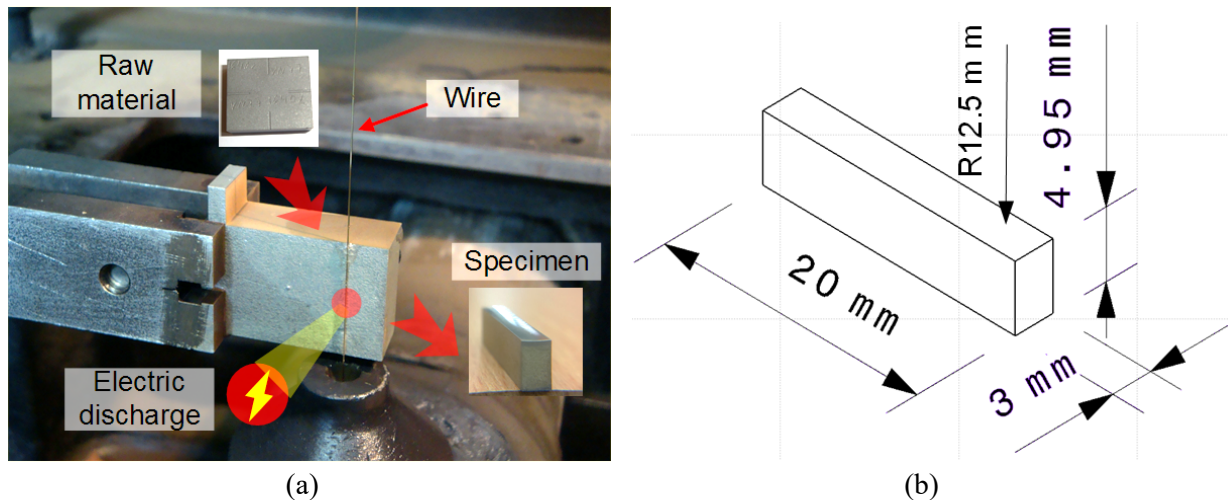


Figure 2-2. (a) VN77 specimen production using W-EDM, (b) dimension of the produced VN77 specimen with curved top surface

However, the mechanical strength of the cemented carbides might be strongly affected by EDM. The degree of which it is affected depends on the correlation between sizes of induced defects, flaws and the level of the tensile residual stresses developed at the shaped surface [16]. The affected zone can penetrate several micrometers into the sublayer of the workpiece. Furthermore, these methods can lead to non-uniform residual stresses in the surfaces, [17,18]. Characteristics of the eroded surface after the W-EDM processing can be observed in Figure 2-3. This figure reveals common induced thermal damages such as material melting, cracks and pores etc. A crack of about $4 \mu\text{m}$ can be found penetrating into the sublayer after the W-EDM processing.

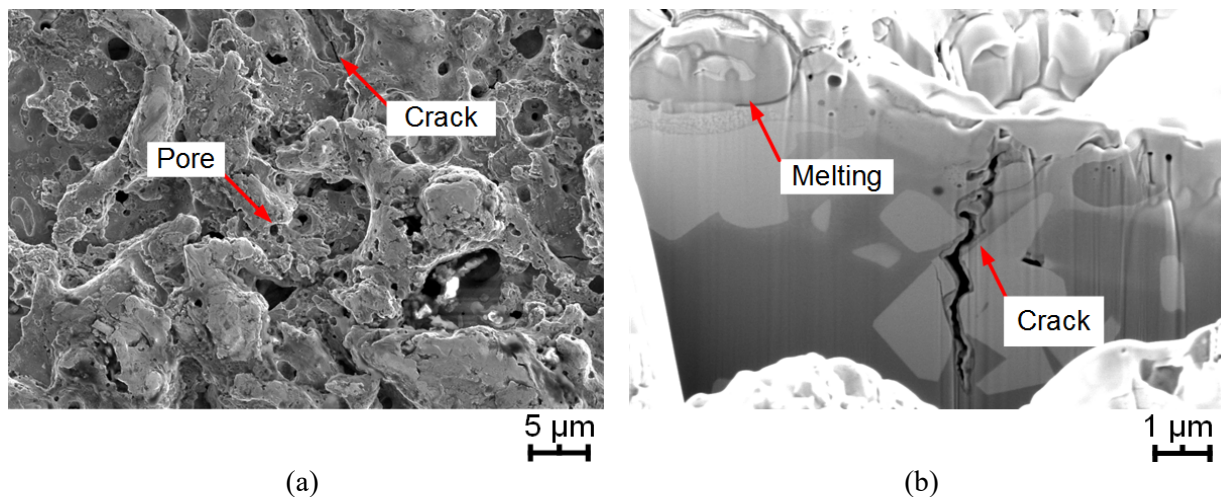


Figure 2-3. VN77 specimen shaped by W-EDM: (a) surface inspection by SEM, (b) FIB cross-section

Therefore, the polishing of the eroded surfaces is imperative, since the induced ‘impurities’ by W-EDM in the surfaces can strongly influence the energy absorption in the laser processing, which can cause inhomogeneities of the new structures or even some critical failures in the surface modification. The specimen surfaces are polished in accordance with the program described in Table 2-3. After polishing, the eroded sublayer is removed and the inner structure of VN77 specimen is exposed (Figure 2-1(b)). For the specimens with a radius (i.e. a curved surface), the aforementioned processing method is not valid any more due to the specific form. The manual method of using a felt polisher has proven to be effective and optimal results can be achieved using the program mentioned in [19].

Table 2-3. Metallographic processing program for VN77 specimens

Steps	Pre-grinding	Grinding	Pre-polishing	Polishing
Polishing paper	SiC paper 320	MD-Allegro*	MD-Dac*	MD-Nap*
F_n (N) per specimen (N)	35	30	30	25
Time (min)	7	5	15	3
Lubricant	Water	6 μ m Diamond Suspension	3 μ m Diamond Suspension	1 μ m Diamond Suspension
Platen Rotation (r/min)	300	150	150	150

* produced by company Struers

2.1.3 Metallographic preparation of CBN composite

The delivered CBN specimens have the same dimension of 20×3×4.95 mm³ as the produced VN77 specimens. In the metallographic preparation, CBN grains can often break out or split out when the binder can no longer hold and support the grains due to their high hardness and fragility. The breaking-out of these hard grains is harmful to the polished surface, which leaves some scratches on the surface. Therefore, slight normal forces and low rotation speed are necessary in the polishing (Table 2-4). The use of diamond suspension in the final step can remove the staked binder around the grains.

Table 2-4. Metallographic processing program for CBN composites

Steps	Pre-grinding	Grinding	Pre-polishing	Polishing	Fine polishing
Polishing paper	CAMEO disk (blue)*	SiC paper 320	SiC paper 500	SiC paper 1200	SiC paper 1200
F_n per specimen (N)	25	10	10	10	Manual
Time (min)	3	2	2	2	2
Lubricant	Water	Water	Water	Water	6 μ m Diamond Suspension
Platen Rotation (r/min)	150	100	100	100	100

* Cameo disk (blue): corresponds to grain size 120-180, produced by Heraeus Kulzer GmbH

Figure 2-4 shows the honing stone B151 surfaces before and after polishing, and the grain contours are clearly exposed after polishing. However, some tiny defects such as pores can be still found.

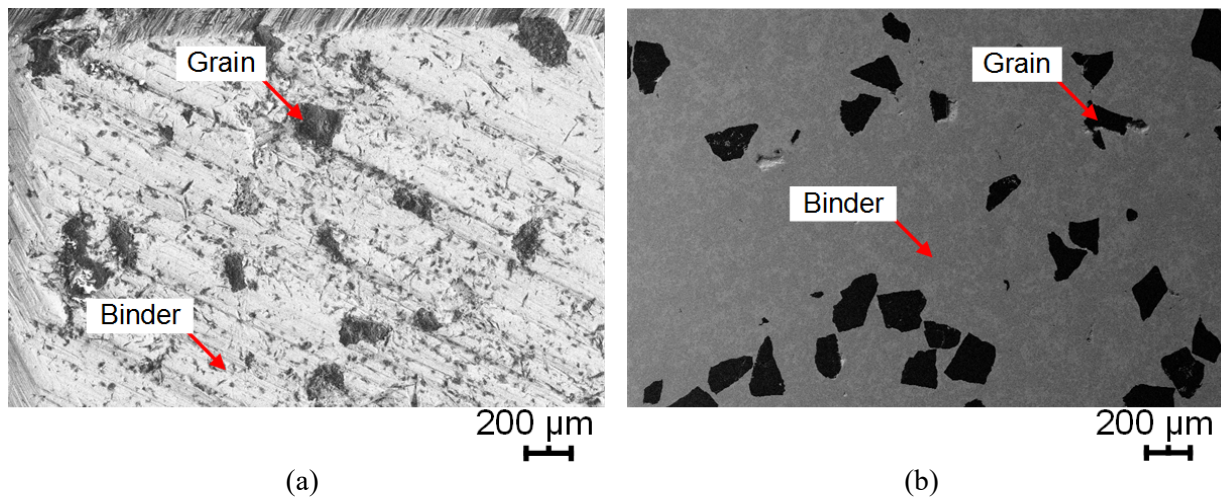


Figure 2-4. B151 specimen surface inspection by LSM (a) before polishing and (b) after polishing

2.2 Significance and approaches of CBN composite characterization

Cubic form of the boron nitride, which is synthesized under high pressure and temperature, is commonly used as super hard abrasives [3,20]. CBN composite is non-conventional, super hard material, widely used in the tool fabrication industry, particularly for precision machining applications (Figure 2-5). In the material removal processes, the microstructure assemblage of the composite plays a significant role in the tool wear mechanism. It has been shown that lower CBN content yields superior wear resistance in finish hard milling of tool steels [5,6]. On the other hand, direct correlation of hardness and fracture toughness to grain size and binder content has been studied and discussed by McKie and coworkers [21]. Surface topography can also have a relevant influence on the tool life. It is reported that smoothing of the tool surface topography can extend CBN tool life during high speed machining of Inconel 718 [22]. It is often observed that grains may degrade by cracking and break out during abrasive processes. Abrasive crystal types and shapes have strong influences on grain wear mechanism. For instance, micro-crystals split and produce sharp cut-

ting edges, whereas mono-crystals lose their layers to generate sharp cutting edges. Grains are erupted when the micro-bonding force between grains and binder exceed certain value. The bonding force can be influenced by the grain size, shape and orientation, etc. It has been noticed that the maximum bonding force can be achieved under optimal grain orientation [23]. Therefore, quantification of all the features associated with the ceramic grains becomes useful to understand the correlation between the microstructural assemblage and mechanical characteristics of the composite and the wear mechanisms of the tool material.

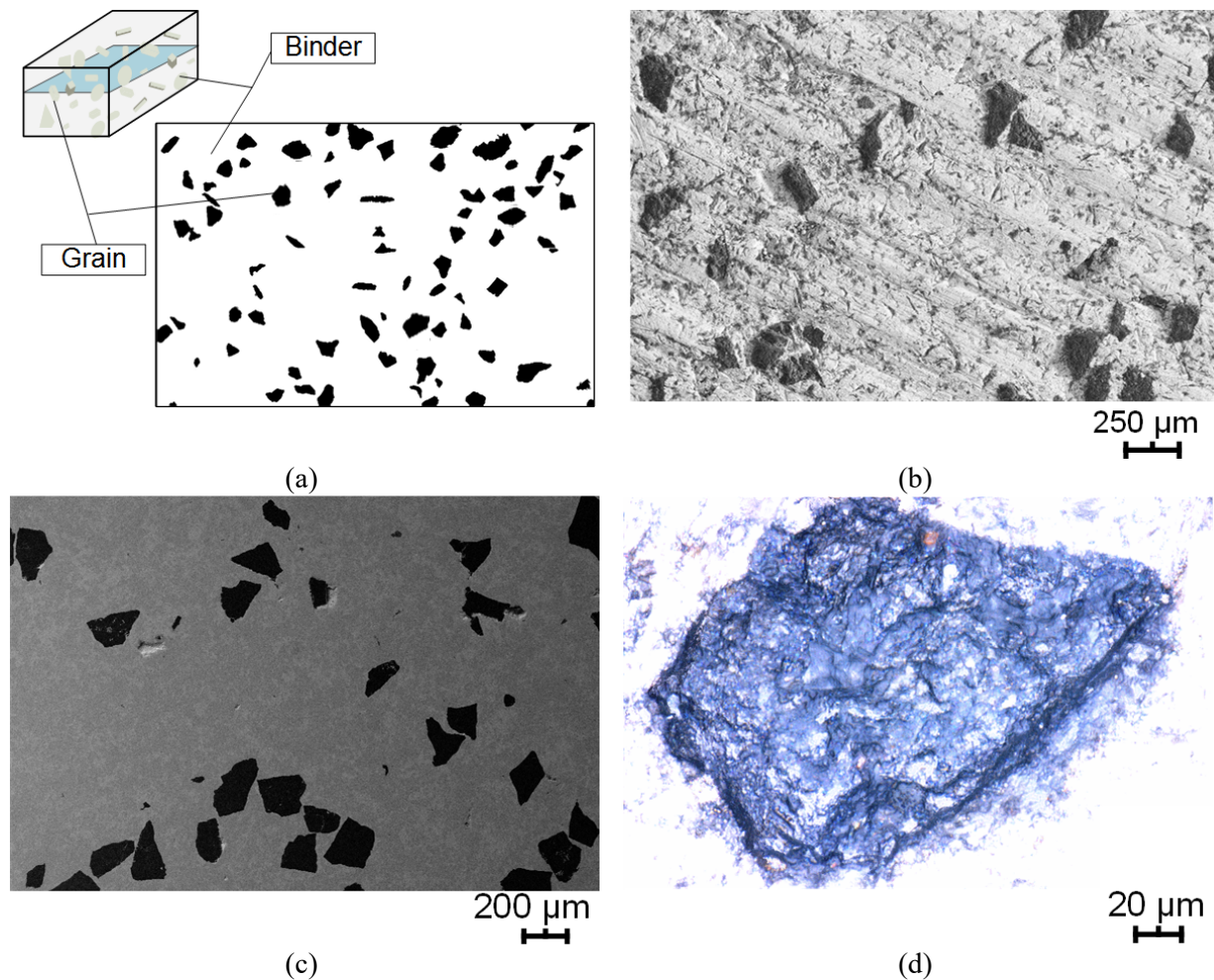


Figure 2-5. Microstructural assembly of composite materials used to fabricate super hard abrasive tools: (a) schematic illustration and cross-section; (b) SEM image showing a typical surface aspect of a CBN honing tool; (c) SEM image of polished surface of CBN honing tool B151; and (d) LSM image of a single monocrystalline CBN grain

Nowadays, surface topography design of abrasive tools is becoming a frontier concept to improve the tool performance [24]. For instance, innovative manufacturing of honing stones has been approached by using glue and piezoelectric nozzle, as well as regular deposition with defined patterns of the ceramic grains on the tool surface [25]. Within this context, Kirsch and Aurich has recently proven that cooling efficiencies can be optimized using slotted grinding wheels [26]. Moreover, it has been reported that grinding wheels with defined grain patterns can ameliorate the grinding ability of materials, and reduce the forces and power in the grinding processes

[27,28]. In this dissertation, one important task is to produce defined structure on WC-CoNi hardmetal surfaces to create cutting edges for the abrasive machining application. Hence, on the basis of surface topography design or modification, it seems clear that quantification of ceramic grain features can offer an effective and applicable path towards description and evaluation of new grain patterns to be generated on the tool surface.

Scanning electron microscopy (SEM) is a common characterization technique invoked for investigating the surface of cutting tools. Furthermore, the combined implementation of SEM with other techniques, such as focused ion beam (FIB), extends the application of the former into three-dimensional sectional analysis. For instance, different fracture mechanisms of mono- and micro-crystalline CBN grains have been discerned and compared using SEM [28]. Similarly, based on SEM inspection together with newly developed image processing techniques, quantitative characterization of microstructural changes and varying cooling rates during solidification of hypoeutectic Al-Si and Al-Si-Mg alloys have been achieved [29,30]. Although SEM is suitable for surface characterization, its application in practice is strongly limited by the implicit requirements regarding sample preparation and environment. Laser scanning microscopy is also a technique commonly used not only for 2D metrological measurements, but also for 3D surface topography characterization. Compared with SEM, Laser scanning microscope (LSM) implies lower costs, besides being simpler and easier to operate. LSM can meet most of the needs involved for surface topography investigation of the abrasive tools, especially for characterization of grain features. For example, a three-dimensional model of one single diamond grain has been reconstructed using LSM [31]. Moreover, topography characterization using laser methods has also been implemented as in-process inspection method in several abrasive machining processes [32]. The topography of grain protrusion of the truncated diamond grinding wheel has been visualized using laser methods, and some important parameters such as protrusion number, height etc. have been characterized [33]. However, implementation of laser methods to investigate ceramic grain parameters is rather limited to the assessment of roughness of the tool surface and dimensional properties of single grains. Meanwhile, there is a lack of systematic and statistical investigation of other important parameters of the grains in abrasive tools, such as form, quantity and location.

Following the above ideas, a main objective of this study is to propose an experimental protocol aimed for systematically quantification of the ceramic grains on the tool surface, as well as for statistical assessment of the geometrical properties of grains on the cutting surface of abrasive tools. Furthermore, the volume characterization is also preliminarily attempted to describe the microstructural properties of the abrasive tools. The obtained geometrical and microstructural information of grains from surface topography quantification will support and contribute to the abrasive surface design and its reproduction on hardmetal surface. Hence, it is mainly focused on the two-dimensional surface topography quantification of the abrasive tools in this

study, and the three-dimensional volume quantification is also carried out and shortly explained.

2.3 Approaches of hardmetal surface modification

Surface treatment of structural materials has received increasing attention, since it usually yields improved functional performance, significant life extension and even wider application fields [34-36]. Surface modification on micro- and/or nano-scale with high geometrical precision is considered as an effective method to improve surface functions of cutting tools, such as reduce friction, improve wear resistance, and improve corrosion and thermal resistance. These benefits result from the fact that the contact condition between the tool surface and workpiece can be effectively improved by surface modification, e.g., improve the distribution of the lubrication, avoid excessive friction and reduce wear of both tools and workpieces. Regular surface patterns lead to the stabilization of the lubrication film covering the whole contact surface. For example, the inner surface of the cylinder, after the honing processing, possess reticular motifs, which facilitates the lubrication supply and stabilize the lubrication film [9,10]. Some surface modification approaches can reduce the surface roughness, such as polishing and buffing. The decrease of friction is not only helpful to reduce the damages, which can be induced from the adhesion and thermal reactions, but also to reduce the use of lubrication and reduce the cost. It is also effective to deposit a thin film on the surface to improve its thermal or corrosive resistance and to reduce the contact damage [37,38]. All the three main factors (adequate lubrication, decreasing friction and higher wear resistance) lead the whole tribological system to become more stable and consume less energy. Meanwhile, some defined convex structures attract attention to produce new abrasive tool surfaces for high precision machining. It is an innovative approach to fabricate cutting tools with the concept of surface topography design, e.g., abrasive grains have been regularly deposited on the honing stone to improve the cutting ability [24,25]. Other common methods of surface treatments are physical/chemical vapor deposition (PVD/CVD), thin film coating, electrical discharge machining (EDM), directed energy deposition, etc. The resulting surface structures on cutting tools should exhibit adequate combination of hardness, toughness and wear resistance.

2.3.1 Comparison of hardmetal surface modification methods: EDM and LST

WC-base cemented carbides, ceramic-metal composites usually referred to as hardmetals, are first-choice materials for tool applications due to their outstanding tribomechanical performance. However, as expected from their elevated hardness and brittleness, shaping and machining of hardmetals are difficult. It prevents wider usage of them for specific applications where machining may represent a limiting production step, for instance, in the fabrication of tools with intricate outline shapes and/or close tolerances prescribed by design. To diminish these shortcomings, different design and machining routes are attempted. One of them, within the latter approach, is the use of electrical discharge machining (EDM) as the final shaping procedure for manufacturing complex geometry pieces instead of following conven-

tional techniques involving diamond as abrasive, e.g. saw cutting or wheel grinding. During EDM, material is removed by numerous tiny electrical spiking between electrode and workpiece. It does not involve any physical contact; hence, mechanical parameters such as hardness play simple secondary roles as EDM's restricting factors, pointing it out as a suitable alternative for machining hard and brittle materials with appropriate electrical conductivity [39]. In this regard, the capability of EDM as a machining route for shaping cemented carbides has been proven in terms of machining performance indexes at different length scales (e.g., Refs. [40,41]). However, even for the cases where optimum surface conditions are achieved, EDM of cemented carbides usually induces cracks, material re-deposition and relevant residual stresses within a thermally affected zone beneath the shaped surface [12,16,42-44].

Laser surface texturing (LST) has the advantages of being fast, clean and efficient (compared with the traditional chip-removal cutting methods). LST using ultra-short pulse laser has become a popular micromachining method and has been successfully implemented as surface treatment option for hardmetals [45-47]. It is particularly suitable for tiny parts with high precision and short time machining requirements. Therefore, it is implemented to modify tool surfaces and improve the functional properties of contact surfaces. During LST processing, the ultra-short pulse laser has extreme short reaction time with the target material. Thus, material is removed by cold ablation rather than by thermal reaction, i.e. melting and vaporization. As a result, and different from EDM, thermal damage effects may be effectively avoided. Following the above ideas, it is clear that LST of hardmetals is an interesting topic for this study, where different surface patterns have been produced on WC-CoNi hardmetal surfaces using variant laser set-ups and configurations, aiming to fulfil the two different goals for cutting tools made of WC-CoNi hardmetal: friction-reduction and material-removal. Nano-second/pico-second/femto-second laser beams have been applied to find out suitable laser conditions for the production of different surface patterns. The study has proven the capability of high precision 5-axis laser micromachining system, combined with a picosecond laser, to move the beams along the X-, Y- and Z- axis with micrometric precision [48]. Such accurate movement of laser beams, especially their oscillation in the perpendicular direction to the workpiece, facilitates the production of complex surface structures. Such technical development can not only widen the application range of LST but also open windows for creative surface topography design.

2.3.2 Basics of laser surface texturing (LST) and its feasibility on hardmetal

Laser has been firstly proposed by the American physicist Theodore Maiman in the 1960s, and it is the abbreviation of Light Amplification by Stimulated Emission of Radiation. Different from white light, laser can emit monochrome light with identical frequency. Laser beams have high coherency with little divergence, which allows the laser beams to focus on a spot with high intensity and rectilinearly propagate for long distance. A typical laser set-up includes three basic components: pump source, laser medium and resonator (Figure 2-6) [112]. Pump source supplies energy for the laser set-up. Common pump sources are electrical discharges, light from another laser and

chemical reactions. Pump source is dependent on the laser medium, which determines how much energy can be absorbed from the pump source. Laser medium is the essential part of the laser construction, for it determines the wavelength of the produced laser beams. The laser medium mainly concludes liquids, gases, solids and semiconductor. In the laser medium, the spontaneous and stimulated emissions of photons take places as a consequence of the excitation from the pump source. The photons produced by spontaneous emissions are reflected by the resonator back to the laser medium and amplified by the simulated emissions. The basic resonator is composed of two parallel mirrors and allows the laser set-up to produce the beams with identical wavelength. Resonator in combination with other important techniques, such as Q-switch, and mode-locking, enables to emit pulsed laser beams, which strongly expands the applications of laser. Nowadays, laser is not only applied in the manufacturing but also in biology and medicine as a frontier technique. Regarding the surface treatment using laser in the domain of materials sciences and production engineering, the laser processing can be basically classified into four categories: heating, melting, vaporization and shocking [113].

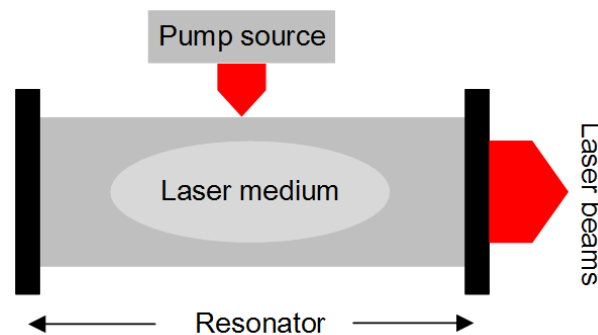


Figure 2-6. Schematic illustration of laser cavity

Since the early 1990s, ultra-short pulse (10^{-12}s - 10^{-15}s) laser processing has been used as a surface treatment method to improve the tribological performance of functional surfaces because it has some excellent advantages, such as high accuracy and excellent quality of the produced surfaces [49,50]. The surface treatment using ultra-short pulse laser processing can be named as laser surface texturing (LST). Current research validates the view that LST is a clean, fast and precise surface treatment technique. It is well accepted that LST is suitable to machine steels with diverse patterns. Most of produced patterns on hardmetals have been used in tribological systems and achieved success in reducing friction of the contacting surfaces [34,51]. In previous research on hardmetal, there is confirmation but only with a little evidence that proves hardmetals are also machinable by ultra-short pulse laser processing. Assessment of the geometrical precision and the quality of the produced patterns are also rarely mentioned in the literature.

The quality of surface patterns produced by laser processing can be influenced by many factors, which can generally be classified into three categories, namely, laser parameters, absorption characteristics and machining parameters (Figure 2-7). Regarding the laser parameters, energy density, wavelength and pulse duration are the

most important intrinsic impact factors. The absorption of the laser beams on the target materials are affected by the material intrinsic physic properties, its surface condition as well as laser-matter interaction. Laser pulse repetition frequency (PRF) and spot number are the two important machining parameters. If the laser beam is integrated in the micromachining system, the precision of stage motion can also influence the produced patterns.

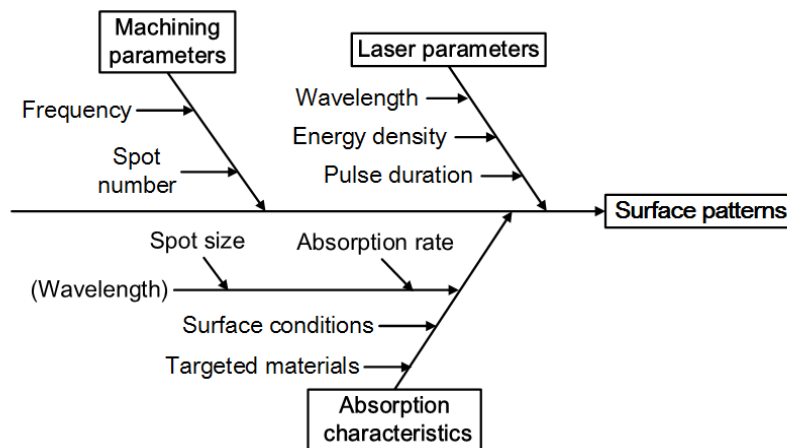


Figure 2-7. Influencing factors of surface patterns produced by LST

The influences of the three laser intrinsic parameters (wavelength, energy density and pulse duration) are introduced and discussed in the following section. In principle, the resolution of produced structures depends on the wavelength of the laser source, whereas the ablation rate is based on energy density, and the ablation depth can be controlled by the spot number [52]. Energy absorption rate as well as spot size is strongly correlated to laser wavelength in the laser-matter interaction. In general, the absorption for metals and ceramics is higher with shorter waves. The absorption rate for hardmetals can reach more than 80% when the wavelength is 1064 nm, and the absorption increase is limited when the wavelength decreases [46,53]. Given that WC, Co and Ni have the respective melting and vaporization temperatures (WC: 3143K, 6273K; Co: 1768K, 3170K; Ni: 1728K, 3003K) [54], it is obvious that The binder (Co and Ni) will be firstly melted and ablated due to the large melting temperature gap between the binder and the grains. Within this context, the energy density (fluence) leads to different material removal sequences: binder can be selectively ablated at the fluence between 0.6 and 2.5 J/cm² in the nanosecond regime. However, when the fluence is less than 0.6 J/cm², no evident vaporization can be observed [55,56].

Pulse duration is the decisive parameter with regard to laser-matter interaction mechanism. The incident laser beam excites the electrons by generating an electric field. The excited electrons are endowed energy by the acceleration. The energy is transferred to the lattice atom by the collision between the electrons and lattice. The vibration of lattice causes the material heating and phase transformation [57]. Therefore, it can be observed that two different material removal mechanisms occur when the pulse duration overpasses ~1 ps [58]. In the femtosecond regime, the material is

mainly removed by cold ablation through non-thermal mechanisms (e.g., induced local stresses, coulomb explosion, and material breakdown) [57]. This can be explained by the fact that there is not enough time to establish electron-photon coupling and to transfer the energy to the lattice. In the nanosecond regime, the material is mainly removed by phase transformations (melting and vaporization) resulting from the local temperature rising induced by the laser [59,60]. In the picosecond regime, a mixture of the aforementioned two processes typically occurs.

In this study, the production of different surface patterns were mainly carried out through the changes of the three important laser intrinsic parameters (wavelength, energy density and pulse duration) and the motion control. These laser produced patterns can be generally classified into two groups according to their profiles (concave and convex), aiming to fulfil the goals of reducing friction and removing materials.

2.4 Evaluation and testing of patterned tool surfaces

Cutting force is one of the most essential considerations to evaluate the tool performances in the machining processes. The ratio between the two components of cutting force (normal force F_n and tangential force F_t) is defined as the tangential force coefficient (TFC). TFC is an indicator of grain sharpness in the abrasive machining processes [61,62]. Typical values of the force ratio and its respective meaning for the process are described by Marinescu et al. [63]. High value corresponds with sharp grain and deep penetration. On the contrary, low value means blunt surface contact and little grain penetration. In the non-abrasive machining processes, TFC can be considered equally as the coefficient of friction (COF). There are some methods to examine and evaluate the machining processes using force measurements, e.g., a test bench was used for tool examinations with variant lubricant types [64,65]. The studies of Schmitt et al. demonstrate the proportional relation between the normal force and the tangential force in the short stroke honing processes [66]. Wear is another important indicator of the machining processes, and it describes the degradation phenomena of the solid surface layer under the external actions. Wear is related to the mechanical abrasive processes, physical-chemical adhesion, chemical erosion and superficial fatigue phenomena. Wear is often characterized by weight loss, dimension change and structure modification [67]. Surface contact conditions have a strong impact to the tool wear mechanism. A simulating model of abrasive wear has been built up and proves the possibility to link the abrasive wear behavior and contact condition [68,69]. Cozza has carried out an investigation of the normal force and abrasive modes, and it is found that COF can present a constant or variable behavior depending on the equipment configuration and contact conditions [70]. It becomes popular to improve contact conditions by texturing functional surfaces in micrometer scale with regard to obtain less wear in the tribological system. Some studies have been carried out and proved that special surface patterns on steels can effectively reduce friction and wear in a tribological system [71-75]. From the above considerations, TFC (COF) and wear are selected as major indicators to evaluate the

patterned tool surfaces in this study, aiming towards the understanding of the material-removal mechanism and the material damage mechanism.

Figure 2-8 summarizes the influencing factors of the TFC. The causes and factors can be grouped into five major categories, including tool, workpiece, lubrication, environmental disturbance and machining parameters. For instance, surface condition of the tool should be considered together with workpiece materials in order to obtain a stable machining surface quality and a reliable TFC. The machining processes could also be affected by the tool wear change at the late stage of tool life. The temperature, pressure and flow rate of the lubrication during the abrasive machining processes should be investigated. The machining parameters, such as rotation speed, oscillation speed/number and feed speed, have direct impact on the tangential force coefficient. The environmental disturbances, such as the machine vibration, the impurities of the material etc., could also influence the machining process.

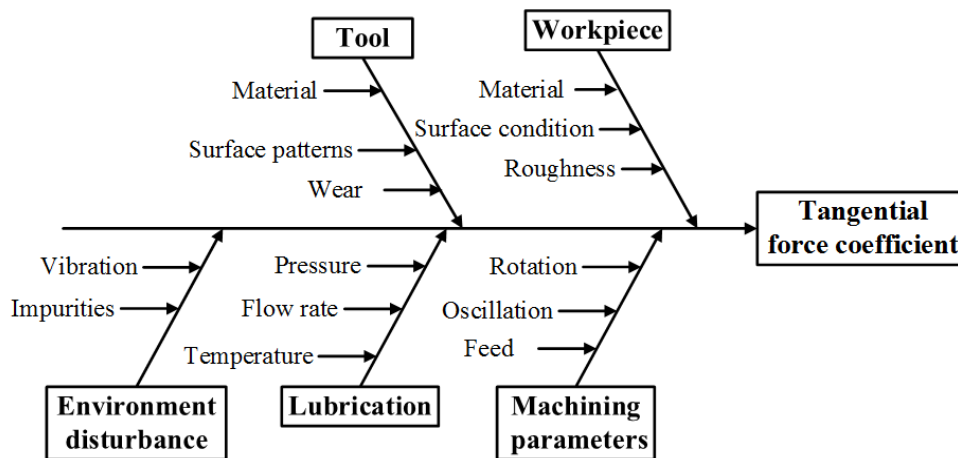


Figure 2-8. Causes and influencing factors of the tangential force coefficient (TFC)

In this study, the experimental design aims to evaluate the behavior of different surface patterns under different normal forces by comparing the obtained TFCs (or COFs). The wear of the surface patterns after testing is studied by assessing their surface integrity. Therefore, the machining parameters, such as rotation speed, oscillation speed/number, and feed speed are set to be invariables. Surface patterns of the tool and normal forces applied on the tool are set to be variables. The workpiece geometry and its surface condition should be determined in advance to meet machine installation requirement. The type of lubrication and its volume should coincident with the machining process and with the test bench design. The lubrication parameters, such as temperature, pressure and flow rate, are set as the invariables in the experiments. The obtained force coefficient and the following wear investigation are the indicators of the behavior of different surface patterns. The variables and invariables are summarized in Table 2-5. Three experimental set-ups are implemented to study and evaluate the tool surface patterns, including the in-house build test bench, Nano-tribometer and Calowear set-up.

Table 2-5: Variables and invariables of input parameters and their effects

	Input parameters		Process effects
	Variables	Invariables	Measurement
Machining parameters	Normal force	Rotation Oscillation Feed	
Tool	Surface pattern	Materials Dimension	Cutting forces Surface integrity
Workpiece		Materials Geometry Roughness	Roughness Surface integrity
Lubrication		Temperature Pressure Flow rate	Temperature Pressure Flow rate

2.4.1 Testing workbench for friction and abrasive testing

In order to systematically analyze the different parameters and their impact under the conditions within the abrasive processes, an in-house test bench has been constructed [48]. The measured variables serve as a basis for a quantitative and valid evaluation of the impacts; as needed complemented by analysis at the tools and workpieces. Subsequently, the concept, design and application of a test bench are based on the conditions during the process of external honing. This test bench is generally employed for the analysis of the influencing parameters during the abrasive machining processes by force measurements, and it can also be implemented to evaluate the frictional performance of functional surfaces as a tribometer. Exemplary machining parameters such as cutting speed, cutting forces and cooling lubricants have been chosen as they are essential elements of cutting processes.

The test bench is adapted to determine the abrasive machining process with certain tool and materials by measuring the cutting forces. The test bench, set on a milling machine, consists of five components: Supporting structure, Movement supplier, Lubrication system, Detection devices and Analysis devices (Figure 2-9(a)). The milling machine platform supports the test bench and supplies the longitudinal feed. The tool (test sample) is set on a force measurement platform and the workpiece is clamped on the milling machine spindle which supplies the oscillation movement and the rotation of the workpiece.

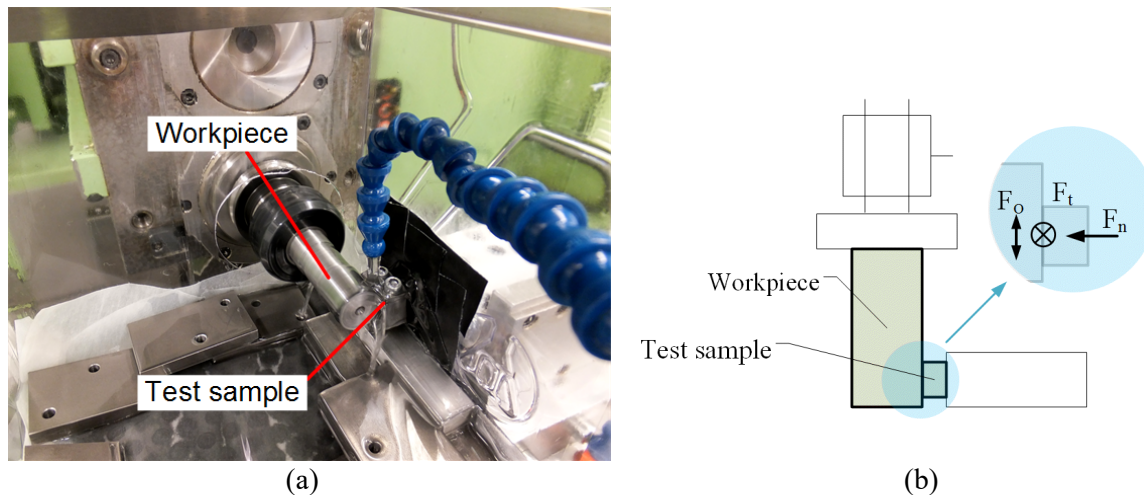


Figure 2-9. (a) Workbench for abrasive machining processes, (b) dynamics in the abrasive machining process

The test samples should have the identical dimension of 20 mm x 3 mm in the XY-plane. Working surfaces of test samples should have a radius of 12.5 mm in order to adapt the test counterpart profile (Figure 2-9(b)). The workpieces used as counterpart in the tests are made of steel 20MnCr5 (Table 2-6), which has the hardness of 260 HB. The workpieces have been pre-machined to obtain the dimension shown in Figure 2-10. The working surfaces should be polished to meet the experimental requirements.

Table 2-6. Chemical composition of 20MnCr5

Element	C	Si	Mn	Cr	S	Other
in wt.-%	0.20	0.25	1.25	1.15	< 0.035	(Pb)

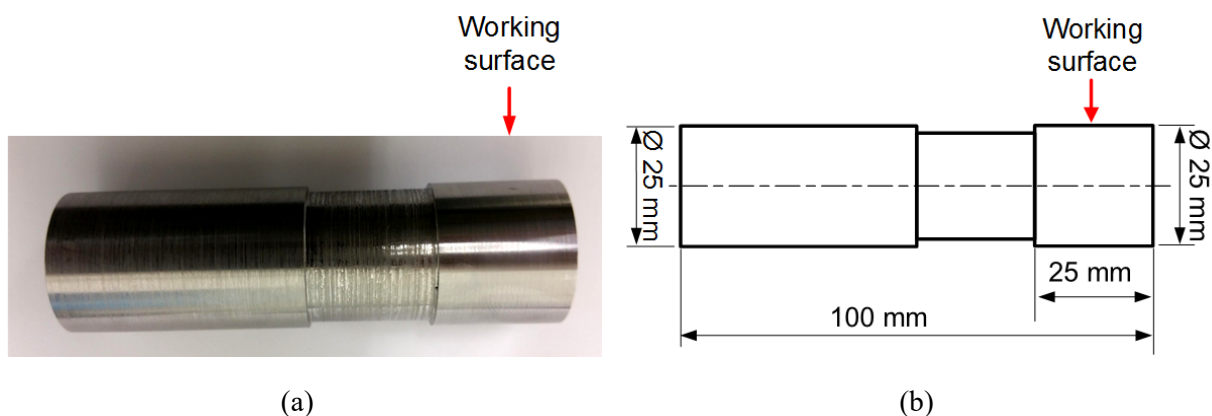


Figure 2-10. (a) Testing counterpart, (b) geometrical properties of the testing counterpart

The testing processes consist of three independent movements: rotation and oscillation of the workpiece, and longitudinal feed of the tool. The three independent movements generate the cutting force between the test tool and the workpiece. Thus, the cutting force can be decomposed to three orthogonal forces corresponding with the movements (Figure 2-9(b)):

F_n : Normal force along the X-axis produced by tool feed

F_t : Tangential force along the Y-axis produced by workpiece rotation

F_o : Oscillation force along the Z-axis produced by workpiece oscillation

Knowing the normal force F_n and the tangential force F_t , TFC can be calculated with Equation (2-1) [61-63,66]:

$$TFC = \frac{F_t}{F_n} \quad (2-1)$$

Before the test, the machining parameters are set as constant. During the tests, the lubrication status can be controlled and adjusted by its temperature, pressure and flow rate. The cutting forces are detected and visualized in real-time and the force signals are recorded using the software Genesis 2i. Surface integrity of the tool can be assessed after the machining process using LSM or SEM. Hence, TFC (or COF) and the wear of tool and workpiece can be analyzed and compared.

2.4.2 Nano-tribometer

The Nano-tribometer (NTR-CSM instruments) is employed to investigate the mechanical contact response by means of friction measurement, especially suitable for low forces and displacements with high accuracy and precision in micrometer scale (Figure 2-11(a)). The stiff cantilevers fixed in the horizontal and vertical directions can transduce the forces into signals produced by the movements of test samples. The test counterpart (ball) is applied on the test sample with a precise normal force F_n . The force is measured and adjusted by the piezo-actuation, which maintains the normal force during the movement loop.

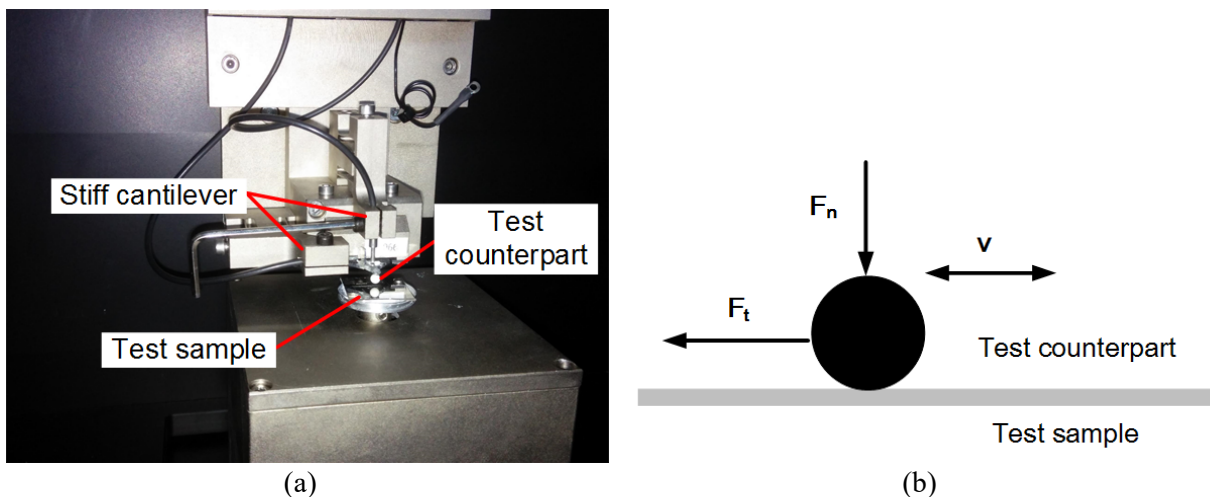


Figure 2-11. (a) Nano-tribometer set-up, (b) dynamics of the Nano-tribometer

The Nano-tribometer can measure the coefficient of friction (COF) by sliding movement between the samples and balls with or without lubricants. The lubricant can be manually supplied at the beginning of the tests. The normal force F_n applied on the ball and the tangential force F_t produced by the reciprocal movement are recorded during the test (Figure 2-11(b)). COF is then calculated in account of the two forces using Equation (2-2):

$$COF = \frac{F_t}{F_n} \quad (2-2)$$

2.4.3 Calowear test

Calowear test is applied to measure the wear rate by means of the mechanical sliding between the tool surfaces and the testing counterparts. Calowear test can quantify the wear rate resulting from the sliding movement between the sample and the testing counterpart. Figure 2-12(a) shows the Calowear test instrument (CSM Instruments). The instrument is suitable to measure the wear coefficient of bulk materials or to measure a combined wear rate of coated material for both substrates and coatings in small scale.

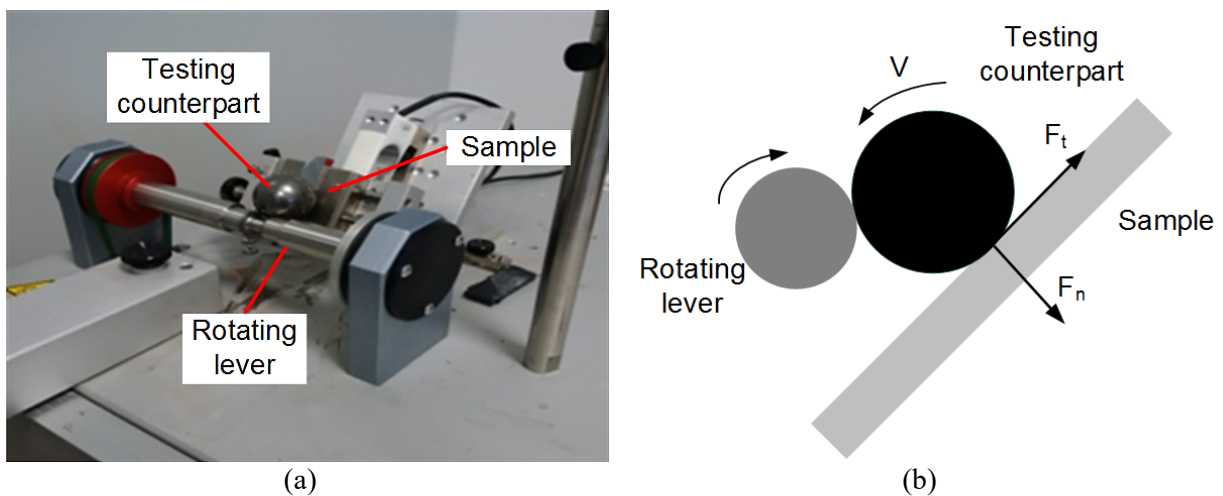


Figure 2-12. (a) Calowear test instrument, (b) kinematics of the Calowear test

The instrument is usually composed of several functional elements: adjustable sample support table, sensitive load cell, rectangular-cut shaft, and motion control unit. The testing counterpart (a steel ball of standard dimension $\text{Ø}25$ mm with standard weight) is positioned between the support table and the rectangular-cut shaft. The test sample is fixed on the table and supports the rotating ball. The table can be adjusted with a specific angle to obtain a desired force components F_n and F_t . The ball is driven to rotate with certain speed by the rectangular-cut shaft (rotating lever) (Figure 2-12(b)). The rotation speed is adjusted by the motion control unit and can vary from 10 r/min to 1000 r/min. The tests can be lubricated with an integrated lubrication supply system. During the ball rotation, materials of the test sample are removed and a crater is then produced on the sample surface.

A force measurement platform is integrated in the sample support table, and it displays the force applied on the sample in real-time. The normal force F_n applied on the sample as well as the diameters of the testing counterparts are considered as given parameters. The sliding distance is recorded during the test. Wear rate is calculated by taking into account all the parameters in Table 2-7 with Equation (2-3):

$$K = \frac{\pi \times b^4}{32L \times F_n \times d} \quad (2-3)$$

Table 2-7: Variables and invariables of input parameters for Calowear test

Symbol	Parameter	Variable	Invariable	Measurement	Calculation
K	Wear rate	-	-	-	√
b	Wear crater diameter	-	-	√	-
L	Sliding distance	√	-	-	-
F_n	Normal force	-	√	-	-
d	Ball diameter	-	√	-	-

3 Tool material characterization

3.1 Surface topography quantification of super hard abrasive tools (CBN composite) in 2D

3.1.1 Materials and assessment parameters

The honing stone B151 has been selected as the studied material, and the honing stone B91 was also studied as a reference case. Table 2-1 on Page 6 shows the microstructural properties of the both honing stones. The LSM Olympus Lext OLS3100 is used to acquire the images of the honing stone surfaces (Table 3-1). The laser with the wavelength of 408 nm is employed as illumination resource. It includes a 150 mm x 100 mm auto-stage, equipped with the maximum vertical movement of 70 mm which is able to support the specimen with maximum height of 100 mm. The objective lenses vary from 5x to 100x, with the optical zoom from 1x to 6x. The LSM has a resolution of 0.01 μm .

Table 3-1. Features of the LSM Olympus Lext OLS3100

Designation	Laser wavelength (nm)	Stage size (mm ²)	Vertical movement (mm)	Max. specimen height (mm)	Objective lens
Olympus Lext OLS3100	408	150 x 100	126	100	5x, 10x, 20x, 50x, 100x

Surface topography quantification includes evaluation of important geometrical properties (Figure 3-1) of single CBN grains, as well as corresponding statistical analysis. The measured and analyzed parameters are quantity, dimension, form and position.

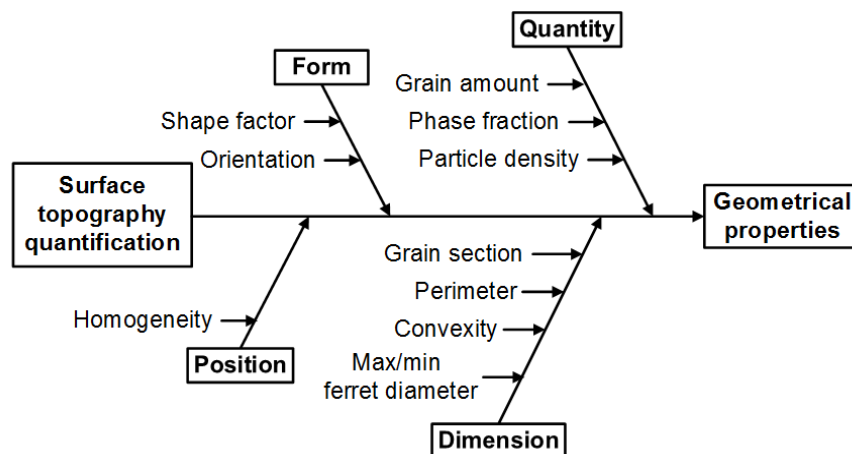


Figure 3-1. Assessment parameters of surface topography quantification

Quantitative parameters

Three parameters (Table 3-2) are used to describe the quantitative properties of the grains: grain amount N_t , phase fraction r_p and particle density D .

Phase fraction r_p is calculated by Equation (3-1):

$$r_p = \frac{S_t}{S_s} \quad (3-1)$$

S_t : total grain sections

S_s : surface area

Particle density D is calculated by Equation (3-2):

$$D = \frac{N_t}{S_s} \quad (3-2)$$

N_t : Grain amount

Table 3-2. Quantitative parameters

Symbol	Parameter	Definition
N_t	Grain amount	Number of all the observed grains on the analyzed surface
r_p	Phase fraction	Ratio of the total grain section (S_t) to the surface area (S_s)
D	Particle density	Grain amount per mm ²

Dimensional parameters

Seven parameters (Table 3-3 and Figure 3-2) are invoked to describe the dimensional properties of the grains: Grain section S_g , Perimeter U , Convex perimeter V_c , Convexity K_c , Max/min Feret diameter F_{max}/F_{min} and Mean Feret diameter \bar{F} .

Convexity K_c [77,78] is given by Equation (3-3):

$$K_c = \left[\frac{V_c}{U} \right]^2 \quad (3-3)$$

K_c : Convexity

V_c : Convex particle perimeter

U : Particle perimeter

Table 3-3. Dimensional parameters

Symbol	Parameter	Definition
S_g	Grain section	Grain cross-section area
U	Perimeter	Grain contour length
V_c	Convex perimeter	Contour length of the convex grain
K_c	Convexity	Quadratic value of the ratio of the perimeter to the convex perimeter of the particle
F_{max}/F_{min}	Max/min Feret diameter	Maximal/minimal distance between two parallel tangents of the particle at an arbitrary angle (36 angles are selected from 0° to 180° with an interval of 5° to simplify the calculation)
\bar{F}	Mean Feret diameter	Mean value of the Feret diameters at the selected 36 angles

Convex particle perimeter V_c is always inferior or equal to the real perimeter of the particle U ; therefore, the convexity K_c should lie between 0 and 1. Convexity describes the deviation grade of the particle perimeter from its convex perimeter. Convex perimeter of a particle is less sensitive when the shape profile becomes less smooth, which can result from the change of the size and number of the irregularities on the border [79]. Feret diameter F measures the perpendicular distance between parallel tangents touching opposite sides of the profile. This parameter is commonly used to measure and describe a randomly oriented particle [80,81].

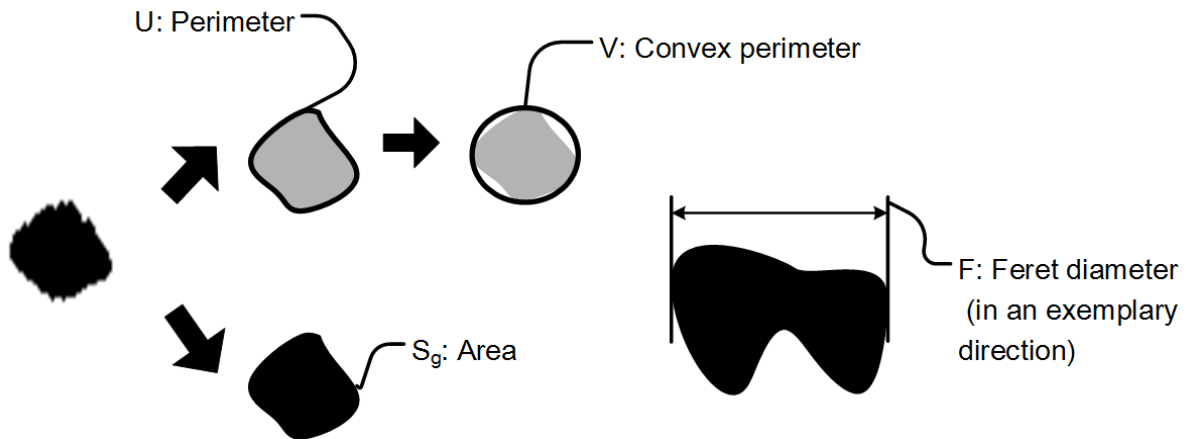


Figure 3-2. Schematic illustration of dimensional perimeters

Form parameters

Form parameters (Table 3-4) have been used to describe form-related features of the grains: shape factor f and grain orientation. Grain shape is assessed and quantified by Equation (3-4) [82]:

$$f = 4\pi \frac{S_g}{V_c^2} \quad (3-4)$$

f : Shape factor

S_g : Grain section

V_c : Convex particle perimeter









Table 3-4. Form parameters

Symbol	Parameter	Definition
f	Shape factor	Circularity grade
-	Orientation	Angle θ between the X-axis and the long axis of the adjusted ellipse of the particle

Shape factor f is a dimensionless quantity used in image analysis and microscopy that numerically describes the particle shape, independent of its size [83,84]. According to the definition, the value of the shape factor f lies between 0 and 1. The indicator enables the quantification of the shape in terms of the area and corresponding perimeters. Table 3-5 lists the evolution of the shape factor as a function of the shape side numbers. For an ideal circle, the factor value is 1. The factor value gets lower

when the number of the shape side decreases as well as the shape stretches. The factor tends to 0 when the particle is stretched or elongated.

Table 3-5. Shape factor as a function of the corresponding geometries

	Circular	Hexagon	Pentagon	Ellipse	Squar	Rectangle	Triangle	Elongated
Shape								
Shape factor	1	0.907	0.865	0.8*	0.785	0.698*	0.604	<0.5

*: a:b=2:1, a:long side, b: short side

Grain orientation is illustrated in Figure 3-3.

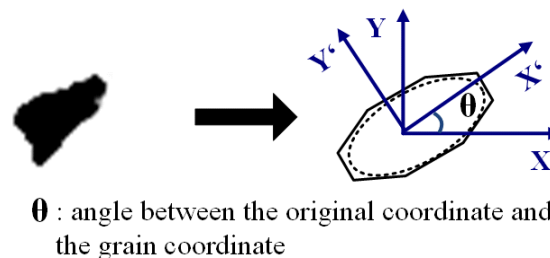


Figure 3-3. Schematic illustration of grain orientation

Positional parameter

Abrasive grains have random distributions on the surface, relative to its quantity and position. This study aims to describe the grain distribution from a quantified point of view, instead of from a statistical analysis one [85]. Thus, homogeneity H (Table 3-6) is selected to describe the grain distribution on the surface. Figure 3-4 gives an example of homogeneity in terms of object amount: there is equal number of grains on the surfaces (1), (2), (3), but grain distribution on each of them is different; therefore, they exhibit distinct homogeneities.

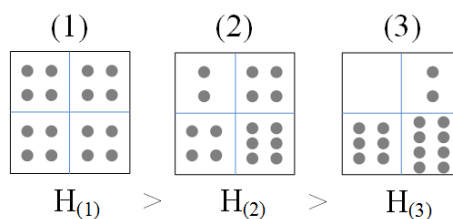


Figure 3-4. Schematic illustration of homogeneity (e.g., object number)

Table 3-6. Positional parameters

Symbol	Parameter	Definition
H	Homogeneity	Similarity of its components considering a given attribute

Homogeneity $H_{(y)}$ can be interpreted by the Gini index: $H_{(y)} = 1 - G_{(y)}$. $G_{(y)}$ is the Gini index, proposed to describe the mean difference from all observed quantities [86]. Therefore, homogeneity of a system is defined as the similarity of its components considering a given attribute [87]. Equation (3-5) gives the mathematic definition of homogeneity. Quantification assessment of microstructural homogeneity can be achieved by means of the Lorenz curve. Homogeneity H is given by the ratio between the area (AL) below the Lorenz curve and the area (AE) below the line of equality [88]. Therefore, the value of the homogeneity H is between 0 and 1. The higher is the value H , the more homogenous is the system.

$$H_{(y)} = \frac{\sum_{i=1}^n (F_{(i)} - F_{(i-1)}) (L_{(i)} - L_{(i-1)})}{\sum_{i=1}^n (L_{(i)} - L_{(i-1)})} \quad (3-5)$$

$F_{(i)}$: cumulative share of components of the system

$L_{(i)}$: cumulative share of the values of the attribute

In order to describe the microstructural homogeneity, region homogeneity h_R is chosen as an indicator. h_R is defined as the product of the two one-attribute-based homogeneities: homogeneity of object number $H_{(Object\ number)}$ and homogeneity of phase amount $H_{(Phase\ amount)}$. h_R can be calculated by Equation (3-6). The entire analyzed surface is equally divided into 10 sections with the same dimension. In each section, the object number and the phase amount are counted, and then the two one-attribute-based homogeneities, $H_{(Object\ number)}$ and $H_{(Phase\ amount)}$, can be obtained by Equation (3-5), respectively.

$$h_R = H_{(Object\ number)} H_{(Phase\ amount)} \quad (3-6)$$

3.1.2 Experimental procedure

The experimental procedure consists of the following steps: specimen preparation, surface scanning, image assembly, image digital processing and surface quantification. Compared with the conventional microscopy, laser scanning microscopy has strong advantages in the 3D investigation of the surface. Reduction of the background influence of the confocal plane as well as the image processing capacity of the LSM allow for obtaining high quality images [89]. It is also suitable to segment the grains from the binder [31]. By using the software Image Access (product of Imagic Bildverarbeitung AG), the image series are assembled. With the software a4i (product of Aquinto AG, Berlin), the assembled image can be binarized and then quantified.

Specimen preparation

The specimens of the honing stones B151 and B91 have the dimensions of $20 \times 3 \times 4.95 \text{ mm}^3$ and the investigated surfaces are fine polished. A gold film has been deposited on the surface to improve the image contrast. The polishing procedure is detailed in Table 2-4 (on Page 9). Polished B151 surface is shown in Figure 2-5(c) (on Page 10).

Surface scanning and image assembly

The size of the image recorded by the LSM is limited by the objective lens. Therefore, the surface should be sectioned, scanned and assembled to obtain the image of the entire surface with high resolution. Each section is measured and numerated under identical conditions. Figure 3-5 shows the example of surface sectioning and assembly processing. The LSM unit is set to measure the surface with the objective 5x, which has a measuring area $2560 \times 1920 \mu\text{m}^2$ with the resolution of $1024 \text{ pixels} \times 768 \text{ pixels}$. The measured surface ($20 \times 3 \text{ mm}^2$) is sectioned into 18 parts and assembled in the next step to obtain the image of the entire surface.

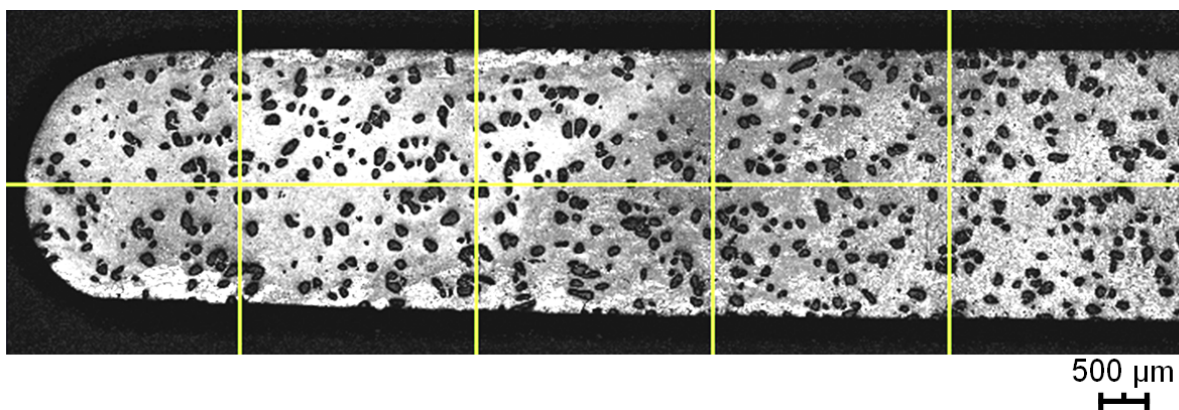


Figure 3-5. Example (10 parts of the honing stone B91) of surface sectioning and assembly by LSM

Image digital processing and grain quantification

Grain quantification is based on the segmentation of acquired images and the subsequent image processing. Grains are extracted from the binder after the segmentation. Meanwhile, it eliminates the influence of the binder and some defects induced during the metallographic preparation, such as scratches, grain split, etc.

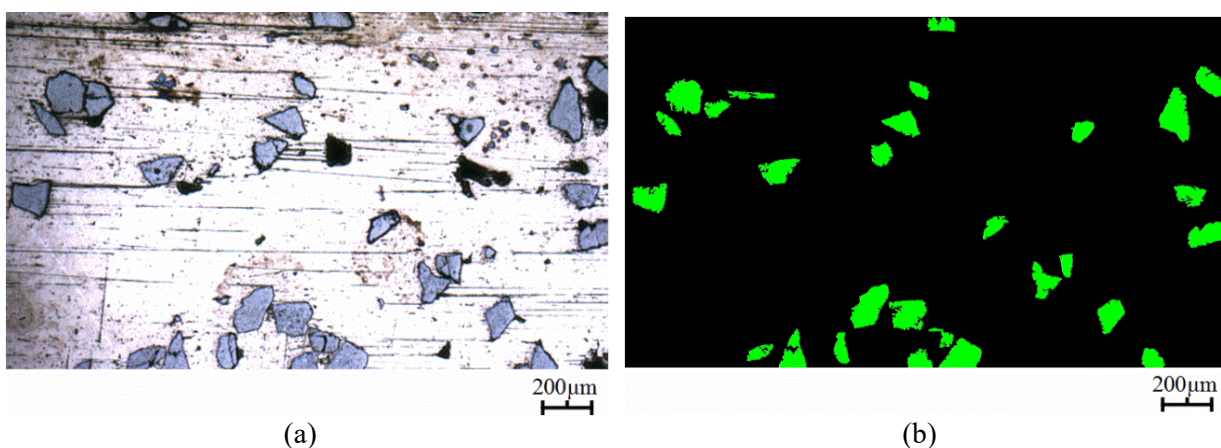


Figure 3-6. LSM images of B151 surface: (a) before segmentation, (b) after segmentation

Figure 3-6(a) shows an acquired image of the specimen B151, where two major phases can be clearly identified: CBN grains and binder, according to the different contrast. Figure 3-6(b) shows the image after the segmentation, where highlighted green blocks represent the grains corresponding with the grey blocks in Figure 3-

6(a). The segmentation accuracy is strongly influenced by the quality of the acquired images. Segmentation defaults can be induced from the equipment accuracy or from the specimen preparation. For example, Figure 3-7(a) shows an image processing case of a micrograph without defaults. Figure 3-7(b) is an example of a grain with a pore in the center, which can be produced in the metallographic processing due to the grain rough edges and its fragility. Figure 3-7(c) shows the common accuracy defaults which emerge when two grains are situated too close to each other. The two grains are treated by the software as one large grain. However, these artefacts may be reduced by morphological treatments in the image digital processing, such as erosion and dilation. Small pores inside particles can be filled in the dilation process where one row of pixels is added to every boundary of the grains. Small bridges between particles can be removed in the erosion process, where one row of pixels is removed from each grain. When the grain is found on the specimen border, the software counts the grain number as 0.5 for the statistics. Grain quantification is executed following the correction of the segmented image.

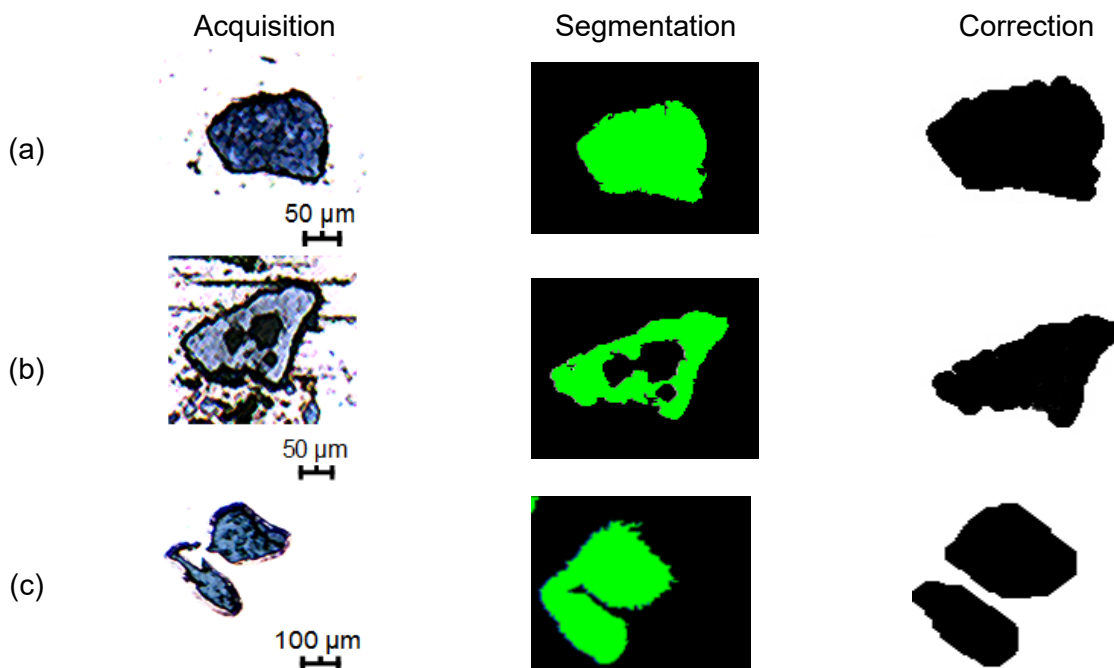


Figure 3-7. Common errors and correction in the image processing: examples of (a) no default, (b) pore, and (c) adhesion

3.1.3 Results and discussion

Figure 3-8 shows the surfaces of the honing stones B151 and B91 after the image digital processing. The results of grain quantification regarding quantity, dimension, form and position are presented in the following sections.

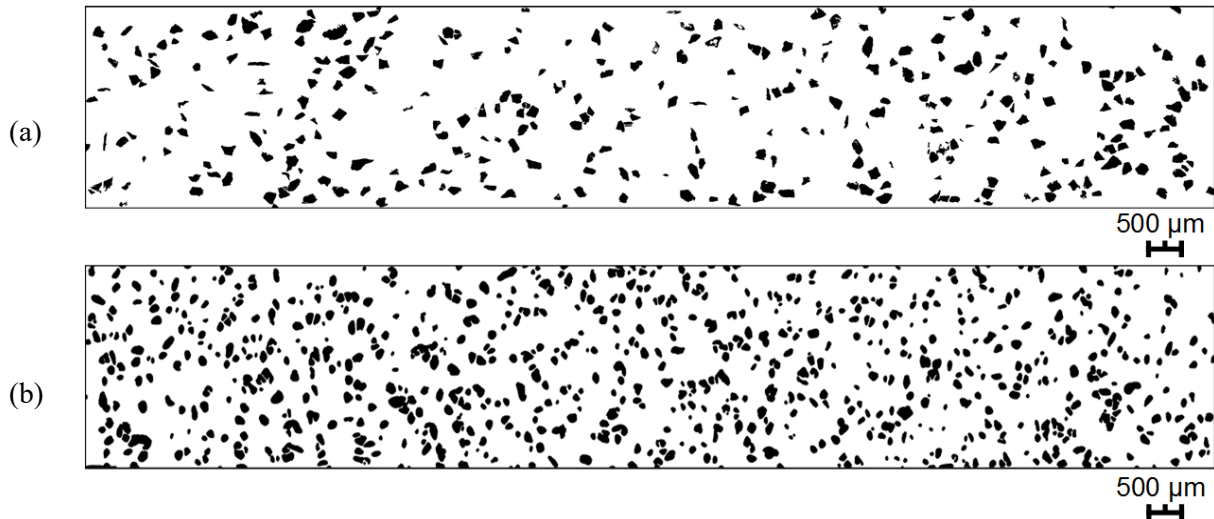


Figure 3-8. (a) B151 and (b) B91 grain distribution after image digital processing

Quantitative parameters

Results of grain quantity are displayed in Table 3-7. On the working surface of the honing stone B151, 355 grains with the surface area S_t of $3.8 \times 10^6 \mu\text{m}^2$ have been analyzed. The scanned surface S_s is $4.2 \times 10^7 \mu\text{m}^2$, (different from the sample surface area $6 \times 10^7 \mu\text{m}^2$ due to damage in the preparatory procedure). Thus, the phase fraction r_p and particle density D of CBN grains is 8.9% and 8.4 mm^{-2} , respectively. For the honing stone B91, 743 grains with the surface area S_t of $7.4 \times 10^6 \mu\text{m}^2$ have been identified on the scanned surface S_s of $4.4 \times 10^7 \mu\text{m}^2$. Thus, the specimen has a phase fraction r_p of 16.6% and a particle density D of 16.7 mm^{-2} .

Table 3-7. Quantitative results of the honing stones

Honing Stone	Grain Quantity N_t	Surface Area S_s ($\times 10^7 \mu\text{m}^2$)	Total Grain Sections S_t ($\times 10^6 \mu\text{m}^2$)	Phase Fraction r_p	Particle Density D (mm^{-2})
B151	355	4.2	3.8	8.9%	8.4
B91	743	4.4	7.4	16.6%	16.7

Dimensional parameters

Table 3-8 lists the mean values of the dimensional parameters obtained from the grain quantification. The grains on the surface of the honing stone B151 have the mean section S_g of $10.6 \times 10^3 \mu\text{m}^2$ and the mean convex perimeter V_c of $391.0 \mu\text{m}$. The mean Ferret diameter \bar{F} is $125.8 \mu\text{m}$, slightly inferior to its mean grain size $138 \mu\text{m}$ (Table 2-1 on Page 6). The grains on the surface of the honing stone B91 have the mean section S_g of $9.9 \times 10^3 \mu\text{m}^2$ and the mean convex perimeter V_c of $360.5 \mu\text{m}$. The mean Ferret diameter \bar{F} is $117.3 \mu\text{m}$, which is greater than its mean grain size $83 \mu\text{m}$ (Table 2-1 on Page 6).

Table 3-8. Mean values of the dimensional parameters

Honing Stone	Grain section S_g ($\times 10^3 \mu\text{m}^2$)	Convex Perimeter V_c (μm)	Convexity K_c	Max Feret diameter F_{max} (μm)	Min Feret diameter F_{min} (μm)	Mean Feret diameter \bar{F} (μm)
B151	10.6	391.0	0.89	151.2	94.1	125.8
B91	9.9	360.5	0.96	137.7	91.3	117.3

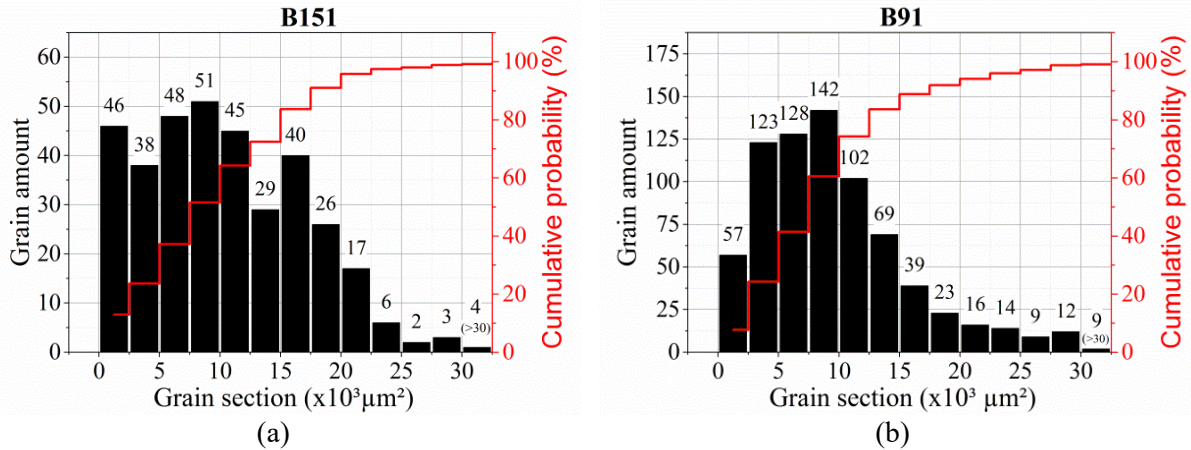


Figure 3-9. Grain sections of (a) B151 and (b) B91

Figure 3-9 shows the histograms of grain amount distribution as a function of grain section. It is observed that the cumulative probabilities of grain amounts are about 50% and 60% for both stones B151 and B91, when the grain sections have their mean values ($10.6 \times 10^3 \mu\text{m}^2$ and $9.9 \times 10^3 \mu\text{m}^2$, respectively).

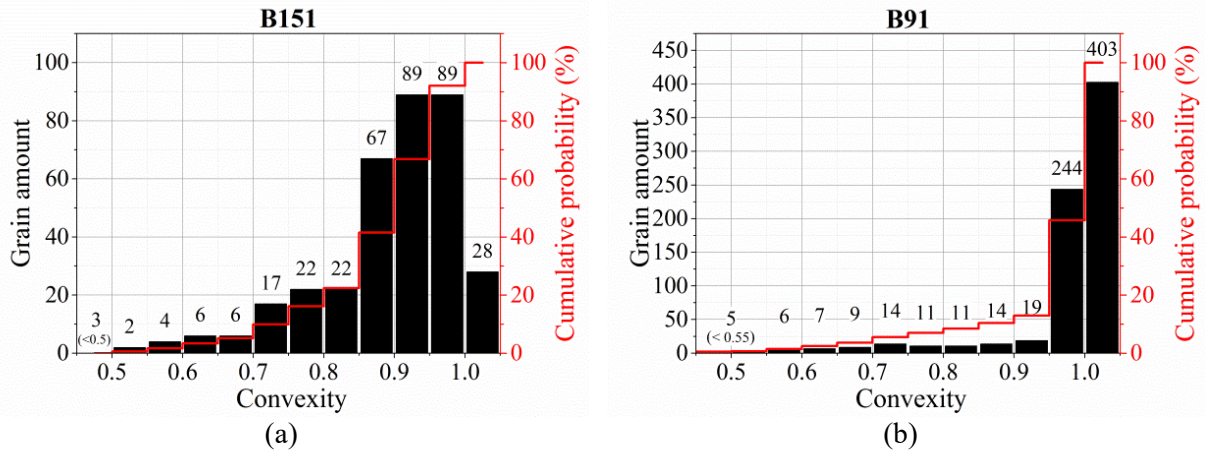


Figure 3-10. Grain convexity of (a) B151 and (b) B91

Figure 3-10 shows the convexity histograms of the honing stones B151 and B91. For the honing stone B151, most of the grains have a convexity between 0.75 and 0.95, whereas for the honing stone B91 it lies between 0.95 and 1. The convex perimeters (Figure 3-11) and the Ferret diameters (Figure 3-12) of the grains exhibit approximate normal distributions.

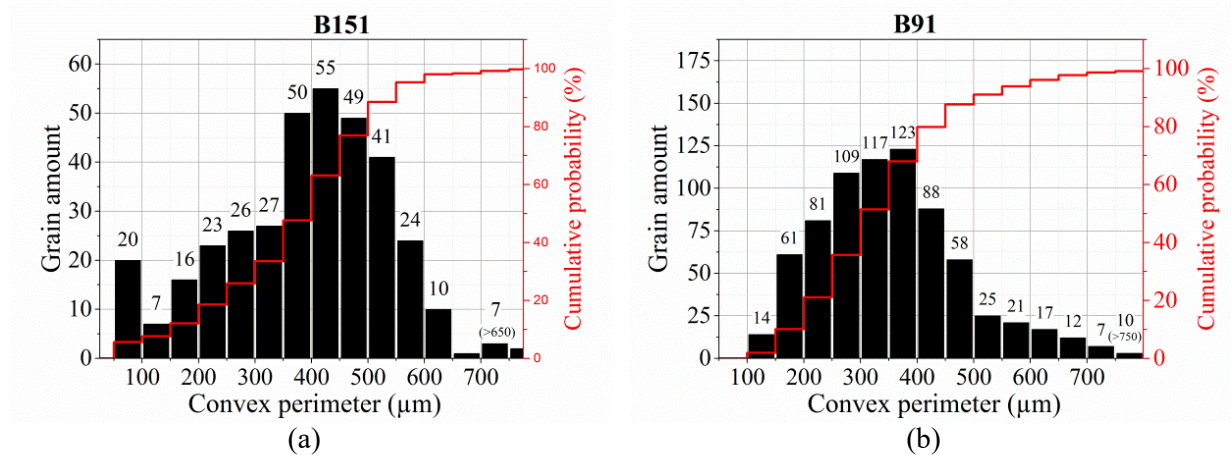


Figure 3-11. Grain convex perimeter of (a) B151 and (b) B91

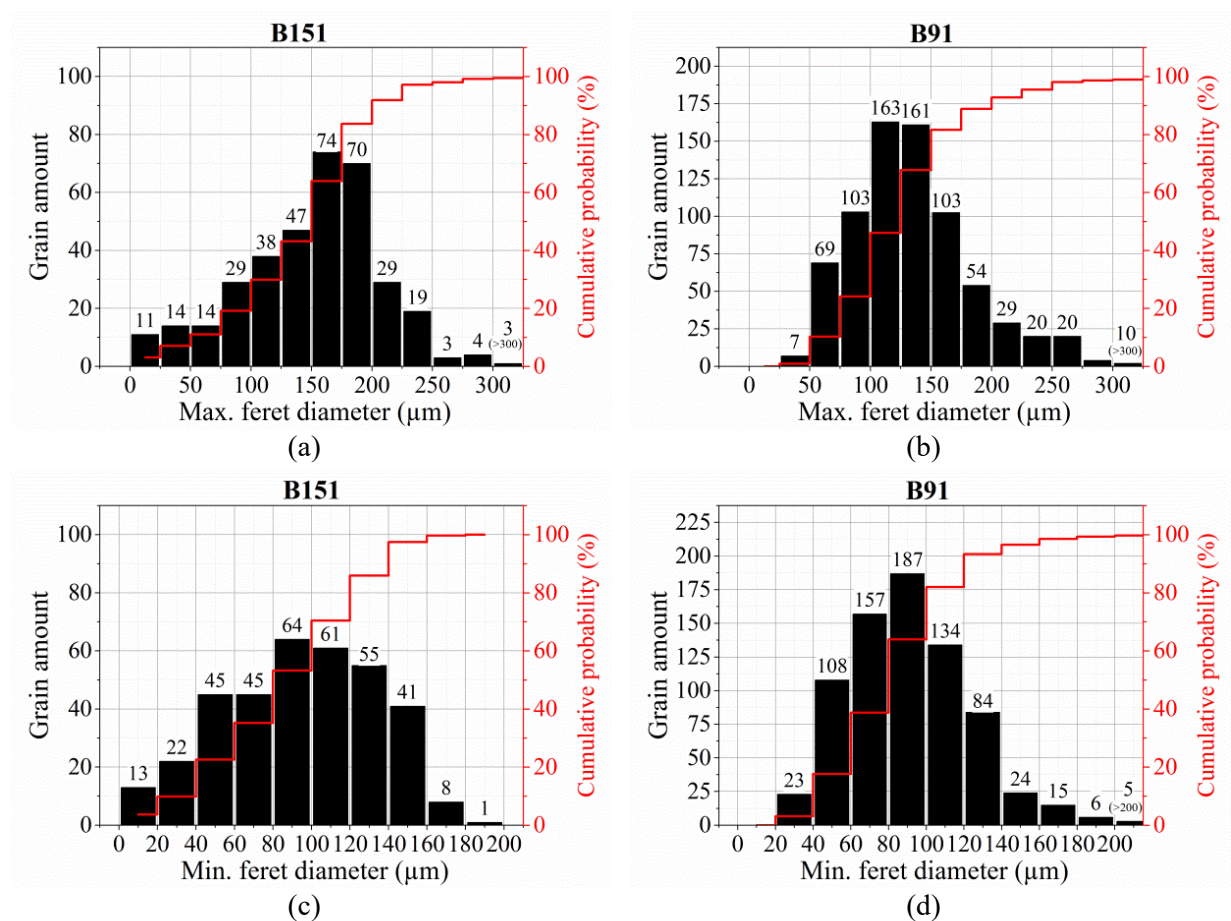


Figure 3-12. Feret diameters of B151 and B91: (a) F_{max} of B151, (b) F_{max} of B91, (c) F_{min} of B151, (d) F_{min} of B91

According to the quantity and dimension analysis, it is found that the total grain quantity and phase fraction of the B91 on the surface is approximately twice as that exhibited by the B151. In consideration of the machining quality of the workpiece, the honing stone B91 can achieve better smoothness than the honing stone B151, by reason of its higher grain density and small contact area of individual grains.

In accordance with the quantification results, grain properties of both honing stones have certain deviations from those given by the manufacturer (Table 2-1 on Page 6). For example, both obtained grain sizes of B151 and B91 (mean Ferret diameters \bar{F} 125.8 μm and 117.3 μm) have certain deviations from the given ones (138 μm and 83 μm). These deviations can be explained by the following reasons.

- The cross sections of the grains on the surface do not go exactly through the grain body center and the grain irregularly spatial distributions can also cause the difference to appear.
- Some defaults introduced in the polishing processes, such as grain eruption, particle cracking, etc., can also result in the observed deviation.
- These deviations can also result from the irregular grain profiles, such as elongated shape, which leads to expanded convex circularity in the segmentation, or from some large grains, which can be mixed in the manufacturing processes.

However, it is found that the obtained grain size of the honing stone B151 (mean Ferret diameter \bar{F} 125.8 μm) approximately conforms to the given one 138 μm , but the obtained grain size of the honing stone B91 is 117.3 μm , and it has a large deviation from the given one 83 μm . This may be rationalized considering that the grains of the honing stone B151 have lower density and larger size than the honing stone B91. Hence, it is more accurate to segment the grains of the former than those of the latter, using the same amount of acquired images with identical resolutions. In the case of the honing stone B91, it is necessary to use more morphological treatments to correct the defaults induced in the segmentation due to inadequate resolution, such as adhesion, impurities, etc. However, the morphological treatments can lead to some unexpected results. For example, the grain edge becomes smooth and the grain shape becomes more round after the operations such as erosion and dilation, which remove the blur asperities and smooth the grain borders. These observations can be proven by the results of convexity in Figure 3-10, which shows that most of the grains of the honing stone B91 are approaching to be more round than those of the honing stone B151. Morphological treatments are more influential to the results of the honing stone B91, since the modification of the pixels has more impact on grain shape when the grains have smaller size. In addition, some common defaults induced in the polishing processes, e.g., grain eruption, particle cracking, etc. are also becoming more significant when the grains have smaller size. Reason for this is the fact that these default features may remain and be considered as grains by the software in the grain segmentation. Thus, it is recommended to use higher resolution during the image acquisition for the honing stone with small grain size, in order to avoid excessive morphological treatments and obtain accurate results.

Form parameters

Typical grain shapes of the CBN composites are shown in Figure 3-13. With the calculation of grain shape factors, the statistics of grain shapes are carried out in Figure 3-14. It is found that the mean value of shape factors is 0.77 for the honing

stone B151, and 0.88 for the honing stone B91, respectively. Most of the grains have a shape factor between 0.7 and 0.9 for the honing stone B151, which correspond with square and hexagon. On the other hand, shape factor is between 0.8 and 1.0 for the honing stone B91, which correspond with ellipse and circular, respectively. Thus, most of the grain sections on the surface have regular forms. The grain sections of the honing stone B91 exhibit more circular than those of the stone B151. The results of B91 can be limited by the used image resolution, which is the same as used for the B151, since the grains of B91 have higher density and smaller size. Figure 3-15 shows the grain orientation on the surface of the honing stones. The grains are in general equally oriented in each direction.

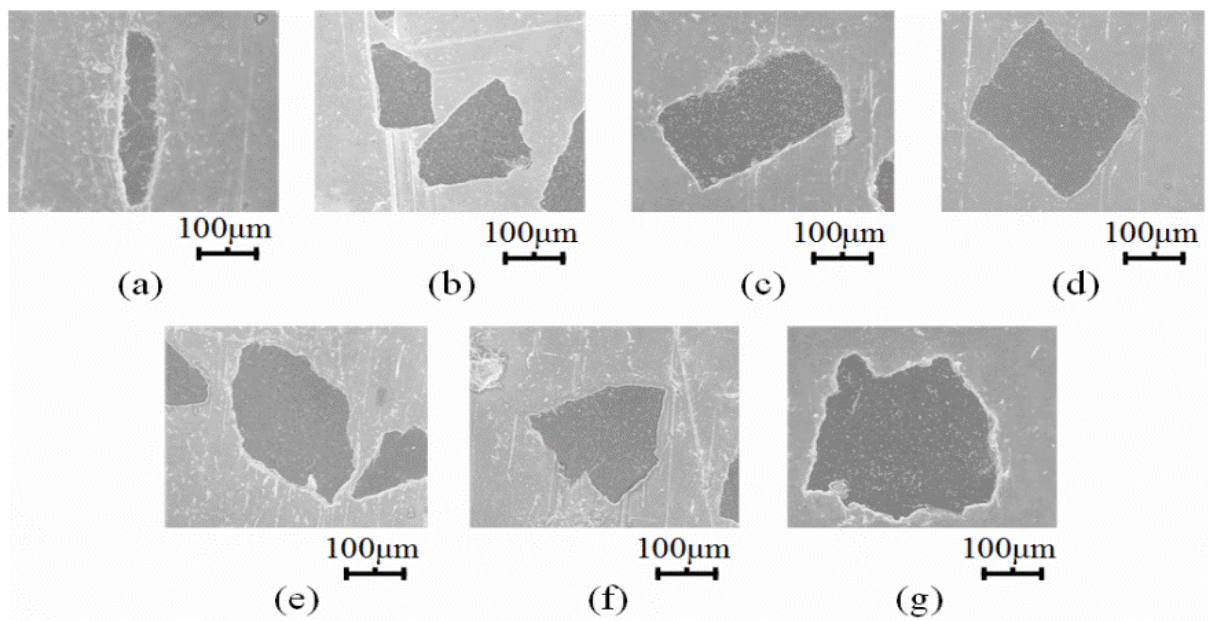


Figure 3-13. Typical grain shapes of CBN honing tools (B151): (a) elongated, (b) triangle, (c) rectangle, (d) square, (e) ellipse, (f) pentagon, (g) circular

Shape factor indicates the grain section shape that is related to the cutting edge in the abrasive process. The results demonstrate that 79.2 % (about 281 out of 355) grains of B151 and 94.9 % (about 705 out of 743) grains of B91 have a shape factor between 0.68 and 1. This attests that most of the grains on the surface are polygons (rectangle-octagon-circle). The orientation analysis indicates that the grains are oriented almost evenly in each direction. In the case of fixed machining directions, the participation of the grain edges in the abrasive process can be considered approximately equal.

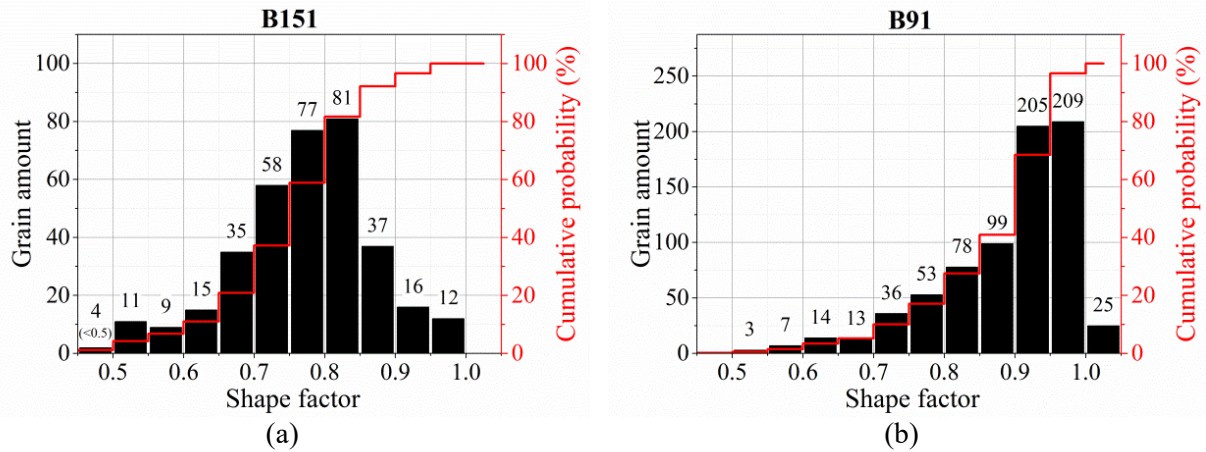


Figure 3-14. Shape factor histograms of (a) B151 and (b) B91

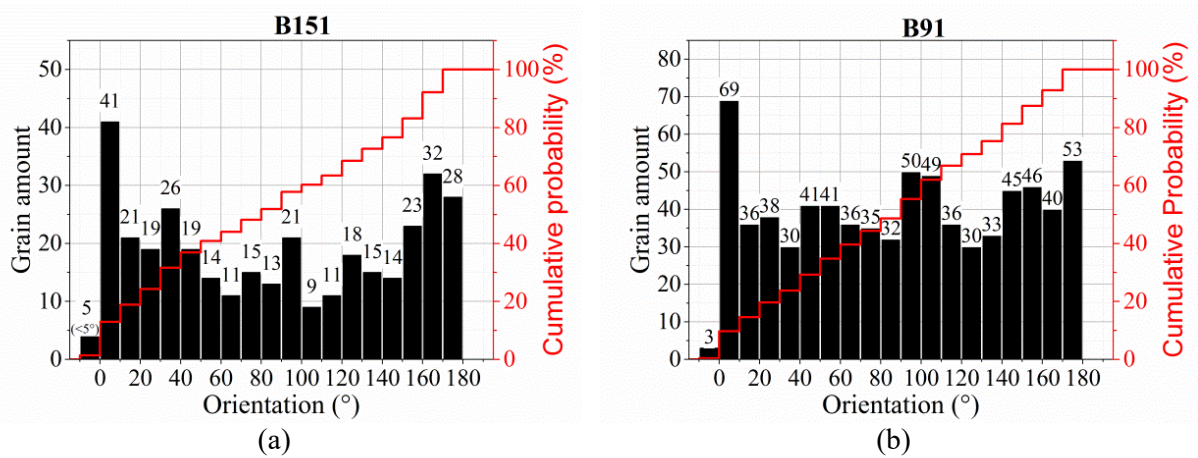


Figure 3-15. Grain orientation distribution of (a) B151 and (b) B91

Positional parameter

It is found that the region homogeneities h_R of the honing stones B151 and B91 are 82.8% and 88.1%, respectively (Table 3-9), which are the products of the homogeneity of object number $H_{(Object\ number)}$ and homogeneity of phase amount $H_{(Phase\ amount)}$. In terms of object number, both studied surfaces have close values 92.1% for B151 and 93.7% for B91, which means that the grains distribute similarly in the ten sections of the studied surfaces. However, the phase amounts have some certain differences, e.g., in the first five sections, the cumulative grain sections account for 43% of the total grain sections for the honing stone B151, and 46% for the honing stone B91, respectively (Figure 3-16). It indicates that the grains of the honing stone B91 distribute more evenly in terms of phase amount. The grain distribution analysis shows that most of the grains of the honing stone B91, which has a higher phase fraction as well as higher grain density, have a more homogenous grain distribution than the honing stone B151. This could also testify that the machined surface by honing stone B91 can achieve better surface quality than the honing stone B151.

Table 3-9. Grain region homogeneities of B151 and B91

Honing stone	$H_{(Object\ number)}$	$H_{(Phase\ amount)}$	h_R
B151	92.1%	89.9%	82.8%
B91	93.7%	94.0%	88.1%

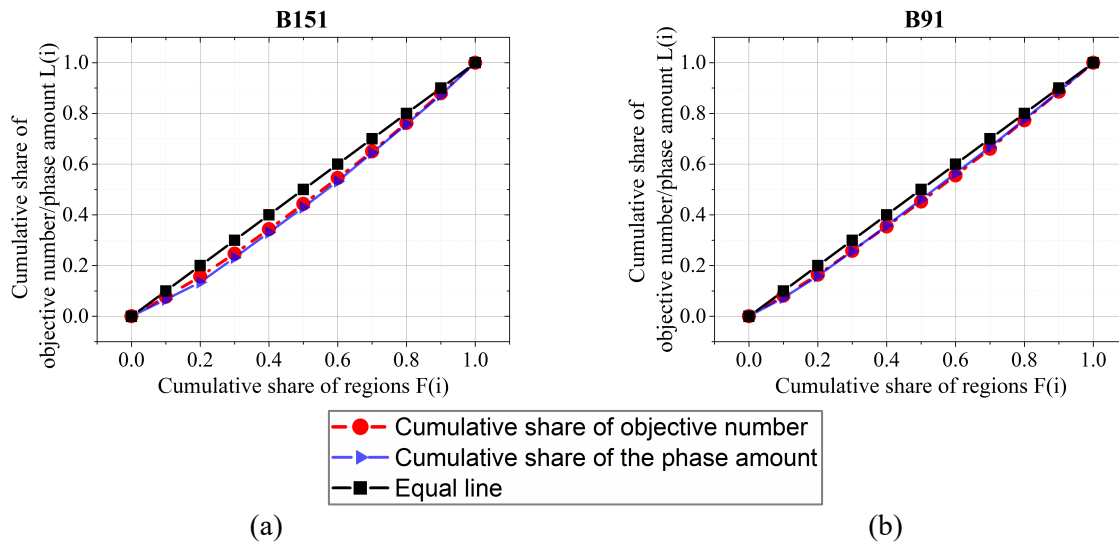


Figure 3-16. Lorenz curves of (a) B151 and (b) B91 region homogeneities

3.1.4 Summary and conclusion

The assessment method of the surface topography quantification by LSM allows for analyzing the geometrical and microstructural properties of the abrasive grains on the tool cutting surface in two dimensions. The geometrical properties of single grains, in terms of quantity, dimension, form and position, have been evaluated. Statistical investigation of all the grains has been conducted. In addition, the grain distributions on the surfaces are described by using the calculation of the region homogeneities. To sum up, it has been proven that the surface topography quantification is an effective method to evaluate and obtain the important geometrical parameters of abrasive grains. The results are acquired based upon the systematic and statistical analysis of a great amount of grains. Therefore, the results are reliable and precise. However, some assignable deviation between the obtained grain size and the one given by the manufacturer regarding the honing stone B91 has been observed, and it is recommended to refine the scanning with higher resolution in order to obtain more precise results. Compared with the sampling inspection method to analyzed single grains, this protocol enables to inspect the tool surface area with large grain quantity in a short amount of time. The method is not only suitable for effective and quick characterization of existing abrasive tools, but also for the assessment of produced grain patterns on tool surfaces. However, the specimen dimension is limited by the LSM capacity; therefore, it is not able to characterize large abrasive tools. In addition, for the characterization of small grains, longer time is required, since images with higher resolution are necessary.

3.2 Volume quantification of super hard abrasive tools (CBN composite) in 3D

In this study, X-ray computed tomography (CT) scan is applied to acquire sectional images of the studied volume. CT scan is a non-destructive method and can be used to analyze and examine objects of materials. A 3D model is generated using the software AMIRA 5 (product of FEI Company) based upon the acquired series of images. Important microstructural parameters such as grain volume, volume ratio, geometrical parameters such as grain density, grain size, and shape parameters are characterized from the grain quantification of the CBN abrasives.

3.2.1 Experimental procedures

The procedure of volume quantification of CBN composite in 3D is shown in Figure 3-17 [90]. In the case of the honing stone, the series of images are obtained by Computed Tomography (CT) and then should be processed by morphological treatments in order to correct the defaults induced from the previous steps and facilitate the segmentation. For example, the filter Alignment is applied to adjust the position of each image, and the filter Global Thresholding is necessary to reduce the range of grey values and to limit the blurred effect. Other common filters such as Resampling Low Pass and Edge-Preserving Smoothing can reduce the noise and smooth curves in an image. In the step segmentation, the grains are separated from the binder and a grey value is assigned to each grain. On the basis of the aforementioned steps, the analyzed volume can be reconstructed by the software AMIRA 5. Important geometrical and microstructural parameters can be obtained after the quantification using the algorithms described in [91-93].

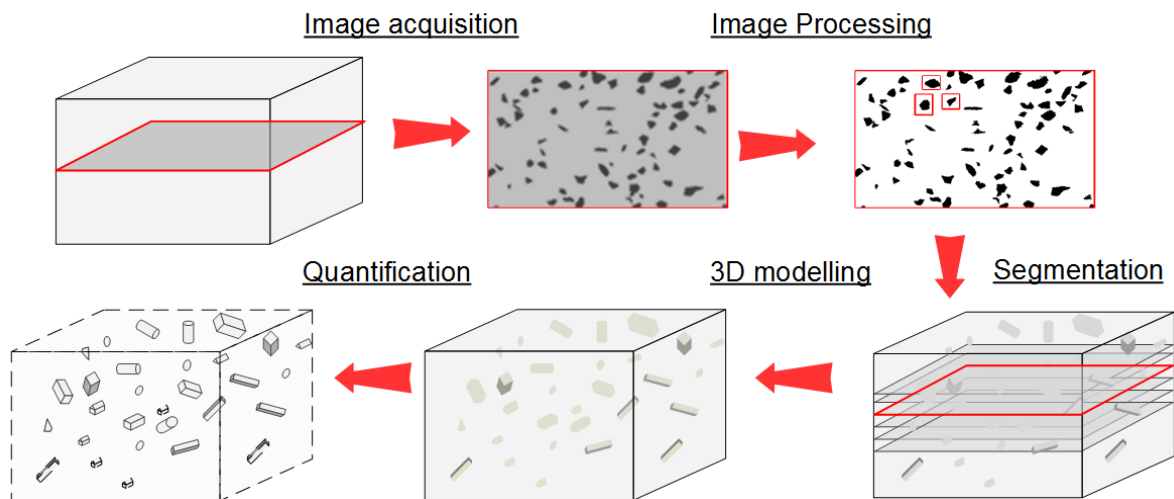


Figure 3-17. Procedure of volume reconstruction and 3D characterization

The honing stone B151/L2/10/50 (B151) is chosen as studied material. In the experiments, the specimen with a volume of $2844 \mu\text{m} \times 16980 \mu\text{m} \times 1765 \mu\text{m}$ has been scanned by CT. In total, 130 images on the XY-plane with the thickness of $13.6 \mu\text{m}$ along the Z-axis have been obtained. The obtained images have the size of 241 pixels along the X-axis, 1439 pixels along the Y-axis. Therefore, the pixel size is 11.8

μm along the X-axis, $11.8 \mu\text{m}$ along the Y-axis and $13.6 \mu\text{m}$ along the Z-axis. The voxel size is then $1.9 \times 10^3 \mu\text{m}^3$. Figure 3-18 shows a cross-sectional image of CBN composite on the XY-plane obtained by CT scan. After the image processing and segmentation, the scanned volume is reconstructed and quantified using the software AMIRA 5.

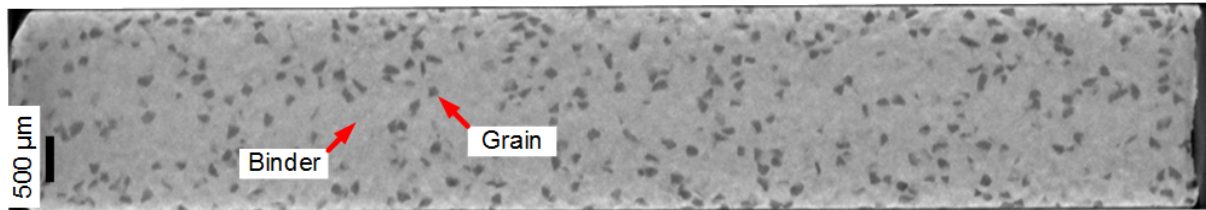


Figure 3-18. Cross sectional image of CBN composite obtained by CT scan

3.2.2 Results and discussion

The grains in the studied volume after the segmentation are visualized in Figure 3-19. It can be observed that the grains are randomly distributed in the volume: grains seem to be more concentrated in some area but less in other area. The shapes of grain cross-sections are not identical, but most of them are polygons according to the cross-sectional image (Figure 3-19(a)). It is also noticeable that the grain shapes vary from each other and have relatively random orientation. Figure 3-19(b) shows that the grains are randomly distributed in the studied volume.

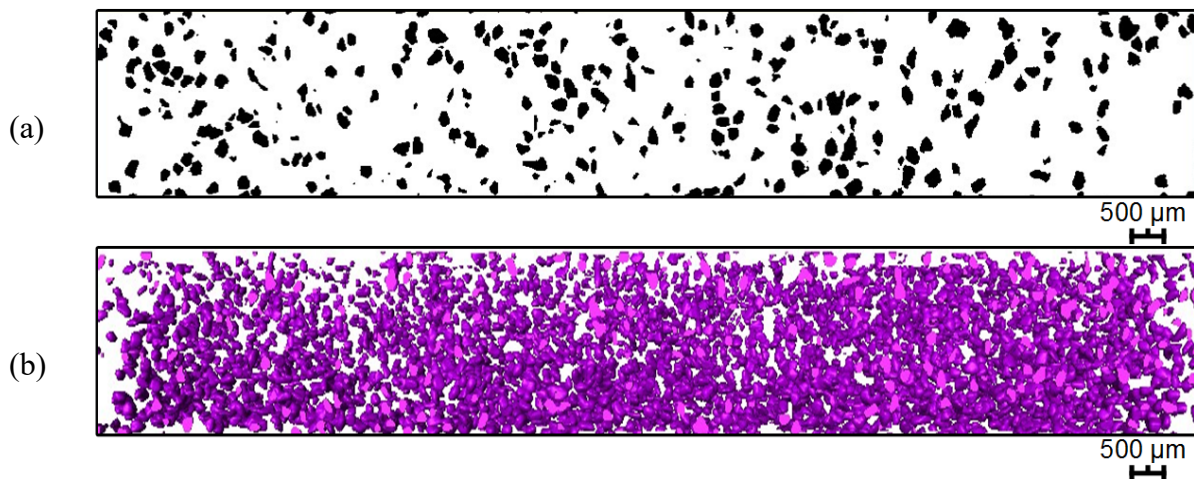


Figure 3-19. Grain segmentation of the specimen: (a) cross-section image of the reconstructed 3D model, (b) grain distribution in the 3D model

Table 3-10 presents the statistical results of the grain quantification of the reconstructed 3D model. The reconstructed specimen volume V_s is $8.5 \times 10^{10} \mu\text{m}^3$, whereby all the grains have the volume V_g of $0.7 \times 10^{10} \mu\text{m}^3$ and the binder has the volume V_b of $7.8 \times 10^{10} \mu\text{m}^3$. Grains and binder then account for 8.2% and 91.8% of the entire volume, respectively. The surface S_g of all grains is $3.2 \times 10^8 \mu\text{m}^2$.

Table 3-10. Microstructural information of the B151 specimen

Specimen volume V_s ($\times 10^{10} \mu\text{m}^3$)	Grain volume V_g ($\times 10^{10} \mu\text{m}^3$)	Binder volume V_b ($\times 10^{10} \mu\text{m}^3$)	Grain volume fraction f_g (%)	Binder volume fraction f_b (%)	Grain surface S_g ($\times 10^8 \mu\text{m}^2$)
8.5	0.7	7.8	8.2	91.8	3.2

Table 3-11 shows the geometrical properties of the B151 grains in the reconstructed volume. It has been found that there are 4093 CBN grains in the studied volume V_s of $8.5 \times 10^{10} \mu\text{m}^3$, namely the grain density is 48 grains/ mm^3 . The mean grain volume \bar{V}_g and the mean grain surface \bar{S}_g are $1.6 \times 10^6 \mu\text{m}^3$ and $7.7 \times 10^4 \mu\text{m}^2$, respectively. Supposing that the grain is a sphere, the equivalent diameter D_{eq} is calculated to be 132 μm , which has a slight deviation from the nominal the grain mean size 138 μm (Table 2-1 on Page 6).

Table 3-11. Geometrical properties of the B151 grains

Grain quantity	Grain density (mm^{-3})	Mean grain volume \bar{V}_g ($\times 10^6 \mu\text{m}^3$)	Mean grain surface \bar{S}_g ($\times 10^4 \mu\text{m}^2$)	Equivalent spherical diameter of grains D_{eq} (μm)
4093	48	1.6	7.7	132

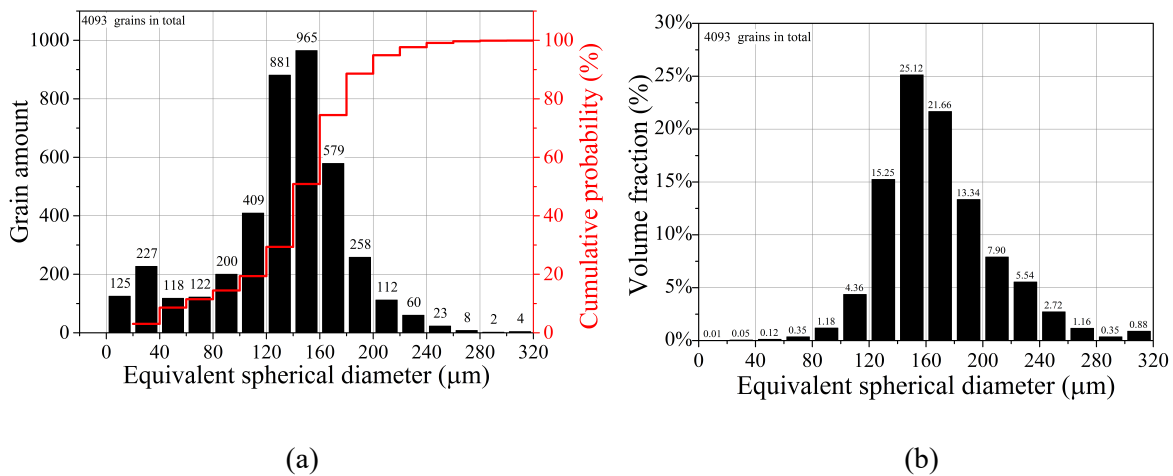


Figure 3-20. (a) Grain amount distribution and (b) volume fraction distribution as a function of equivalent spherical diameter

Figure 3-20(a) shows the grain amount distribution as a function of the equivalent spherical diameter of grains D_{eq} . The distribution of the grain amount is close to a Gaussian approximation, where most of the grains are distributed near the mean equivalent spherical diameter of grains D_{eq} 132 μm . It is found that about 250 grains have the D_{eq} less than 30 μm , which account only for 0.02% volume of all the grains (Figure 3-20(b)). These 250 grains are considered as induced defaults during the imaging processing, where some individual petit particles are produced due to the separation of big particles. Some extreme large grains (larger than 240 μm) have

also been found due to the modelling error, whereby some contacting grains have been considered as one large grain by the software and they were not separated in the image processing. Figure 3-20(b) shows the volume fraction as a function of the equivalent spherical diameter. The distribution has also a Gaussian approximation, and is similar to the grain amount distribution.

Three isoperimetric shape factors are introduced to describe the shape of the intrinsic volumes of convex and compact grains with non-empty interior [94]. For each grain, the three shape factors are calculated by Equation (3-7), using the parameters V , S and M , which represent volume, surface area and integral of mean curvature of grains. The integral of mean curvature M is given by Equation (3-8), where $1/r_1(s)$ and $1/r_2(s)$ are the minimum and maximum curvature at the surface element ds of the grain, and ∂b is the boundary of the grain [91]. The values of the three parameters are obtained from the grain quantification.

$$\begin{aligned} f_1 &= 6\sqrt{\pi} \frac{V}{\sqrt{S^3}} \\ f_2 &= 48\pi^2 \frac{V}{M^3} \\ f_3 &= 4\pi \frac{S}{M^2} \end{aligned} \tag{3-7}$$

$$M = \int_{\partial b} \frac{1}{2} \left(\frac{1}{r_1(s)} + \frac{1}{r_2(s)} \right) ds \tag{3-8}$$

Meanwhile, the grains can be geometrically classified using three corresponding geometrical features, i.e., the length, width and thickness of the grain. Three basic shapes (Figure 3-21(a)) are defined according to the correlations among the three features [95]:

- granule, when the length, width and thickness are approximately equal;
- chip, when the length and width are approximately equal but different from the thickness, or the three parameters are different from each other;
- fiber, when the width and the thickness are approximately equal but different from the length.

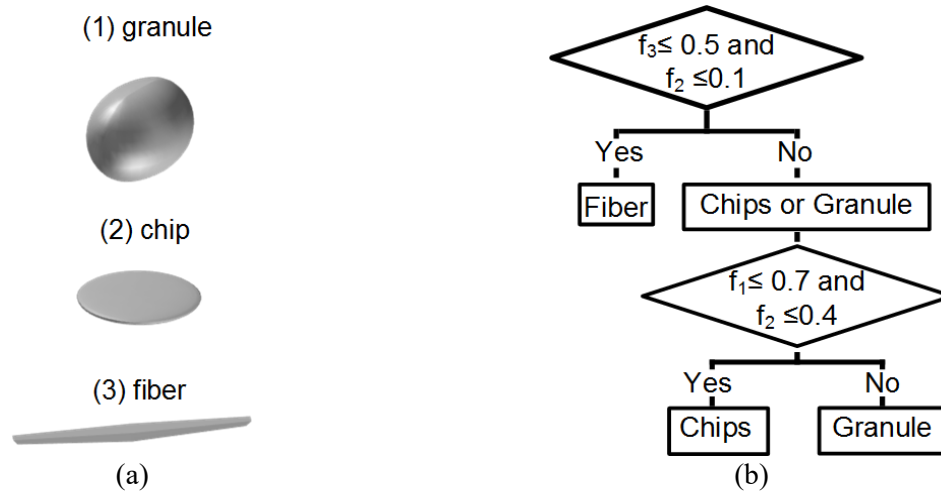


Figure 3-21. (a) Basic grain shape definitions, (b) grain shape classification using shape factors

In accordance with the calculated values of the three isoperimetric shape factors, the grains can be classified into the three basic shape categories (Figure 3-21(b)) [96]:

- when $f_3 \leq 0.5$ and $f_2 \leq 0.1$, it is a fiber;
- if it is not a fiber, when $f_1 \leq 0.7$ and $f_2 \leq 0.4$, then it is a chip;
- if it is not fiber neither a chip, then it is a granule.

When the pixel amount of a particle is too small, the calculation of its shape factors becomes not possible, since the software requires the particle to have at least two pixels along each axis (i.e. 8 voxels) to obtain reliable shape factors. In this case, the grain should have a diameter more than $30 \mu\text{m}$ (approximately corresponding with the volume of 8 voxels $1.5 \times 10^4 \mu\text{m}^3$); otherwise, the shape classification is not reliable any more. Therefore, about 250 grains, which have the diameter less than $30 \mu\text{m}$, should be eliminated in order to analyze the grain shape, then namely 3843 grains have been analyzed. According to their shape classification (Table 3-12), it is found that 31 grains are fibers, 748 grains are chips and 3064 grains are granules. All fibers account for 0.8%, chips for 19.5%, and granules for 79.7% of all the grains.

Table 3-12. Grain shape classification of the B151 specimen

Shape	Quantity	Fraction (%)
Granule	3064	79.7
Chip	748	19.5
Fiber	31	0.8

3.2.3 Summary and conclusion

The volume quantification of the CBN Composite B151 has been conducted using 3D characterization method. A CT scan has been used to acquire a series of images of the volume and the 3D modelling software has been applied to reconstruct the 3D model with the series of images and to quantify the grains. The quantification results indicate that:

- 4093 grains have been inspected in the volume of $8.5 \times 10^{10} \mu\text{m}^3$, whereby the binder account for 91.8% of the entire volume and the grains account for 8.2%.
- The grain amount and the volume fraction as a function of grain size (equivalent spherical diameter) distribution D_{eq} have an approximately gauss distribution. The obtained mean value of D_{eq} is 132 μm , which is close to the nominal mean grain size 138 μm .
- 79.7% grains have a granule shape, and 19.5% grains are chips according to the shape analysis.

3.3 Comparison of the two-dimensional and the three-dimensional quantifications

Three-dimensional volume quantification includes several important steps: volume determination, sectional 2D image acquisition, image processing, segmentation, 3D modelling and quantification. Different from the surface topography quantification, it requires a 3D reconstruction of the studied volume based upon the segmented cross-sectional images. Within this context, the 3D model can be considered as a stack of large quantity of cross-sectional images in certain direction and with certain step space. Hence, it is obvious that the three-dimensional quantification (volume quantification) can avoid the positional influences of the cross sections and the influences of the grain orientations. These two influences can always play negative roles in the two-dimensional quantification (surface topography quantification) and result in the fluctuation of the quantification results. However, it is much more time-consuming to obtain the series of cross-sectional images and process these images for the 3D model reconstruction. For instance, 130 images were needed to reconstruct the B151 sample volume in this case, but only one image is necessary for the surface topography quantification. Moreover, the 130 images should be taken in the identical direction with the same step space in order to ensure the precise alignment in the 3D model reconstruction. In this regard, the three-dimensional quantification has much high implicit requirements of the analytical equipment. It becomes not feasible even for the case where the series of sectional images are taken using traditional manual image acquisition method, such as taking microscopic images by polishing the sample.

Although it is the first attempt to use CT scan to characterize the CBN honing stone, the quantification results is quite satisfactory. The structural and geometrical properties of the grains regarding the quantity, dimension and from were statistically analyzed based upon a large quantity of grains. Within this regard, geometrical properties of the grains obtained from the volume quantification are reliable, such as grain size, grain amount distribution and grain volume fraction distribution. For example, the obtained grain size (equivalent spherical diameter) 132 μm has only a slight deviation from the nominal mean grain size 138 μm , compared to the grain size (mean Feret diameter) 125.8 μm obtained from the two-dimensional quantification. The obtained grain fraction of 8.2% is close to that of 8.9% obtained from the two-dimensional quantification. But both of them have an obvious deviation from 12.5%

described in the specification. Hence, it can be deduced that the deviation was not induced from the analysis procedures, but probably from the material production processes. However, the three-dimensional quantification was not able to precisely analyze all the geometrical properties regarding the form and position. For instance, only three basic shapes have been classified and there was little positional description about the grains. These analyses were limited by the theoretical algorithms and mathematical description. Therefore, more work should be done to find out an appropriate approach to more precisely describe the grain form and position as well as to refine the classification.

4 Tool surface modification

4.1 WC-CoNi Hardmetal surface modification by LST

Table 4-1 lists the produced structures and their corresponding laser set-ups. According to their shape features whether they are concave or convex, the produced structures could be applied to reduce friction or remove materials.

Table 4-1. Summary of the produced patterns and corresponding laser configurations

Pattern	Laser type	Special configuration	Possible application
Line-like	ns-laser	Interference	Friction reduction
Dimples/Grooves	ps-laser	5-Axis micromachining system	
Dimples/Grooves	fs-laser	Auto-stage	
Hexagonal pyramids	ps-laser	5-Axis micromachining system	Material removal
Square pyramids	ps-laser	5-Axis micromachining system	

Special attention has been paid to tribological application of textured surfaces. Line-like patterns, dimples, grooves have been produced for the tribological application to reduce the friction. The surface integrity of all the produced surface patterns has been assessed regarding their geometrical properties and the possible induced surface damages. Frictional performances of line-like patterns and dimples have been compared with other referring surfaces such as polished and EDM machined surfaces. Wear resistance of line-like patterns has been investigated with certain methods, such as Calowear test. In terms of abrasive application, LST is employed to simulate and reproduce the surface topography of a conventional honing stone on the surface of WC-CoNi hardmetal. The honing tool chosen as reference is the one tagged as B151/L2/10/50 (B151). It is aimed to induce simultaneous movement along the X-, Y-, Z- axis of the laser beams, such to remove very tiny volumes of the hardmetal (work-piece) and sculpt grain-like pyramids from the surface. Once aimed surface topography was shaped, geometrical features of LST surface were measured and resulting surface integrity was assessed. Performance of the hardmetal tool with the LST patterned surface was tested in a workbench designed to simulate an external honing (cutting) process. In this chapter, the production of the surface patterns and the surface integrity assessment are presented in detail and the hardmetal tools testing with patterned surfaces will be introduced in Chapter 5.

4.1.1 WC-CoNi Hardmetal surface modification for tribological application

Line-like patterns

Line-like patterns (interference structures) are created by the superposition of two or three pulsed laser beams with the same frequency. Due to the high intensity, energy transformation of the laser beams to the material surface, i.e. melting, recrystallization, phase transformation etc., occurs in the micro- or nanometer scale. This metallurgical process by laser interference structuring is described as Laser-Interference

Metallurgy (LIMET). LIMET is a process, where two or three pulsed laser beams with the identical pulse repetition frequency (PRF) are superimposed on the target surface [97,98]. By means of LIMET, it is possible to produce periodic interference structures on the surface with dimensions on the sub-micron level up to micrometers, depending on the angle between the interfering beams and the thermos-physical properties of the involved materials.

A nanosecond Nd:YAG laser (Spectra Physics Quanta Ray Pro 290) has been used to produce line-like patterns. Table 4-2 lists the parameters of the laser set-up. The laser beams have a PRF of 10 Hz, wavelength of 355 nm, pulse duration of 10 ns. The fluence was kept constant at around 2.3 J/cm². Special configurations of the laser beam trajectories are necessary to obtain the line-like pattern with defined geometry [97,98].

Table 4-2. Parameters of the ns-laser setup for the production of the line-like patterns

Laser type	Laser source	Pulse duration (ns)	Wave length (nm)	PRF (Hz)	Fluence (J/cm ²)
ns-laser	Nd:YAG	10	355	10	2.3

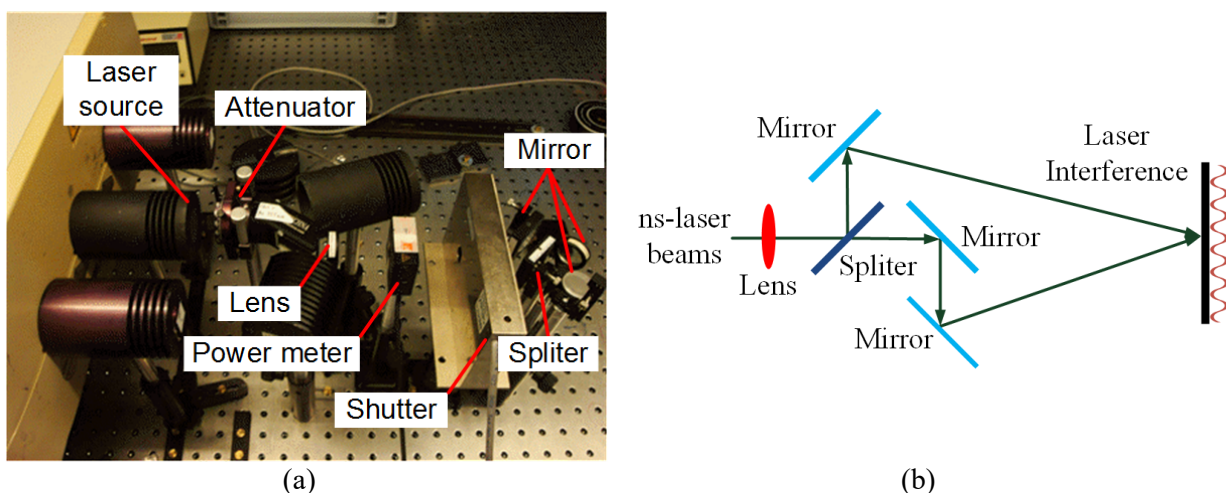


Figure 4-1. (a) Experimental configuration and (b) schematic illustration of LIMET for production of laser interference structure

Figure 4-1(a) shows the special configurations of the laser beam trajectories, which are necessary to obtain the line-like pattern. Figure 4-1(b) shows the schematic illustration of the trajectory of the respective laser beams: the primary beam goes through a lens and is then split into two equal sub-beams by a beam splitter. The sub-beams are reflected by mirrors and finally interfere on the target surface and produce the line-like patterns (interference structure). The trajectory of each sub beam should be equal in order to obtain homogenously symmetric patterns. The superposition of the two sub-beams leads to interference resulting in the line-like pattern (Figure 4-5 on Page 51). Two parameters are used to describe the geometrical properties of the produced patterns: periodicity, defined as the distance between two adjacent peaks or valleys, and height, defined as the distance between the peak and its adjacent

valleys. The periodicity is determined by the trajectory of the laser beams and can be obtained by Equations (4-1) [97]:

$$P = \frac{\lambda}{2\sin(\frac{\theta}{2})} \quad (4-1)$$

λ : Laser wavelength

θ : Angle between two sub-beams

P : Calculated periodicity

Table 4-3. Experimental parameters of the ns-laser setup for the pattern geometry

λ (nm)	Lens (mm)	θ (°)
355	1000	1.8

Table 4-3 shows the experimental parameters of the ns-laser setup. Based on these parameters, the periodicity is calculated to be 11.3 μm . The removed material volume is mainly dependent on the absorption of the laser beam energy [57]. It means that the depth of the line-like pattern depends on the pulse energy and pulse number. In the experiment, single pulse is used.

Dimples

An ultrafast-laser with a picosecond laser system (Nd:YVO₄, HYPER25 Coherent Kaiserslautern GmbH) has been employed to fabricate dimples on the WC-CoNi hardmetal surfaces (Figure 4-2(a)). The picosecond laser system is mounted on the high precision 5-axis laser micromachining system (GL.5, GFH GmbH), which possesses a position accuracy of $\pm 1 \mu\text{m}$ and maximum axis speed of 2 m/s. The used pulse repetition frequency (PRF) is 200 kHz, the wavelength is set to 532 nm, and the pulse duration is 10 ps. The fluence of the laser beams is 0.5 J/cm² at the machining zone. Meanwhile, a femtosecond laser (Ti:Sapphire) in combination with an auto-stage has also been employed to produce dimples (Figure 4-2(b)). The wavelength of the fs-laser is 800 nm, the PRF is 1000 Hz, the pulse duration is 150 fs and fluence is 0.05 J/cm² (Table 4-4). The dimple intervals in X and Y directions are set to be 500 μm for both cases at the mode of single shot (Figure 4-2(c)). Table 4-5 shows the motion control parameters of the micromachining system and the auto stage.

Table 4-4. Laser parameters used for the production of dimples

Laser type	Laser source	Pulse duration (ps)	Wave length (nm)	PRF (Hz)	Fluence (J/cm ²)
ps-laser	Nd:YVO ₄	10	532	200K	0.5
fs-laser	Ti:Sapphire	150 fs	800	1000	0.05

Table 4-5. Motion control parameters for the production of dimples

Laser type	Control mode	v_x (mm/s)	v_y (mm/s)	Interval x (μm)	Interval y (μm)
ps-laser	Single shot	x	x	500	500
fs-laser	Single shot	x	x	500	500

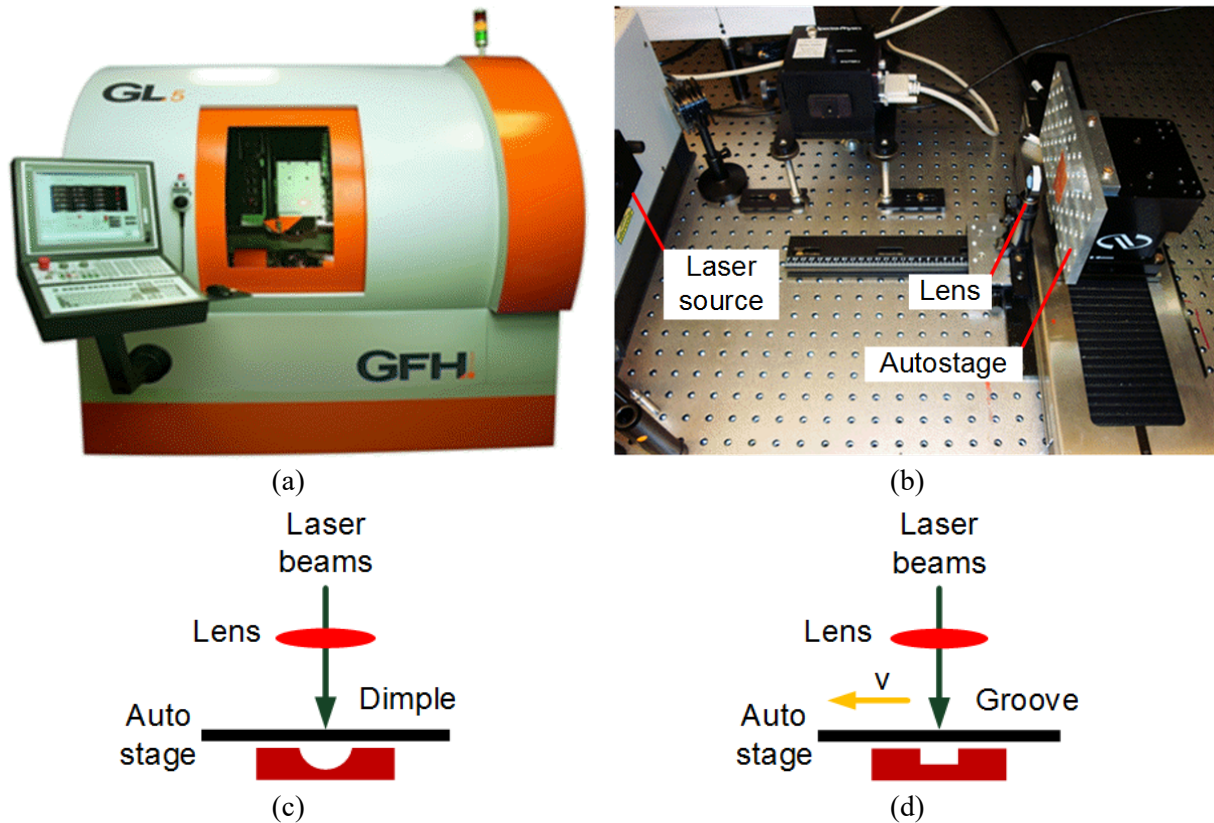


Figure 4-2. (a) High precision 5-axis laser micromachining system (GL.5, GFH GmbH, <http://www.photonik-zentrum.de>), (b) fs-laser set-up with the auto stage, and laser trajectory configurations for the production of (c) dimples and (d) grooves

Grooves

The aforementioned ps-laser and fs-laser with the identical laser processing parameters as the dimples (Table 4-4) have also been used to produce grooves on WC-CoNi hardmetal surfaces. Figure 4-2(d) shows the laser set-up to produce grooves, where the laser beams move constantly along the X- or Y- axis during the machining processes. Therefore, the control mode is different from that of the dimples but set to be continuous: ps-laser beams move along the axis at the speed of 1000 mm/s and fs-laser beams moves at the speed of 20 mm/s (Table 4-6).

Table 4-6. Motion control parameters for the production of grooves

Laser type	Control mode	V_x (mm/s)	V_y (mm/s)	Interval x (μm)	Interval y (μm)
ps-laser	continuous	1000	1000	x	600
fs-laser	continuous	20	20	x	500

4.1.2 WC-CoNi Hardmetal surface modification for abrasive application

Hexagonal pyramids

It aims to simulate and reproduce similar surface topography of the honing stone B151 on the WC-CoNi hardmetal surfaces under the consideration that similar abrasive effects can be achieved for abrasive application. Taking into account of the microstructural assemblage of 151 honing tool, most of the grains emerging on the

cutting surface of the CBN honing stone B151 appear a polygon shape (rectangle-octagon-circle) [99]. Within this context, the ultra-shot pulse laser (picosecond) mounted in the 5-axis micromachining system (Figure 4-2(a)) is implemented to sculpt hexagonal pyramids from the target material surfaces. The processing parameters of ps-laser beams and motion control parameters are shown in Table 4-4 and Table 4-6, respectively. The motion of the laser beams is precisely controlled by the micromachining system. The laser beams can simultaneously move along the X-, Y-, Z- axis and remove tiny volume of the target material per pulse (Figure 4-3(a)). In total 343 hexagonal pyramids are produced on the WC-CoNi hardmetal surface. The following parameters are used to describe the pyramid geometrical properties (Figure 4-3(a) and (b)):

- d_1 : the interval between two adjacent hexagonal pyramids along the x-axis
- d_2 : the interval between two adjacent hexagonal pyramids along the y-axis
- a_1 : the bottom side length of the hexagonal pyramid
- a_2 : the top side length of the hexagonal pyramid
- S_1 : the surface area of the pyramid bottom
- S_2 : the surface area of the pyramid top
- h : the height the hexagonal pyramid
- α : the slope at the measuring position A-A
- β : the slope at the measuring position B-B

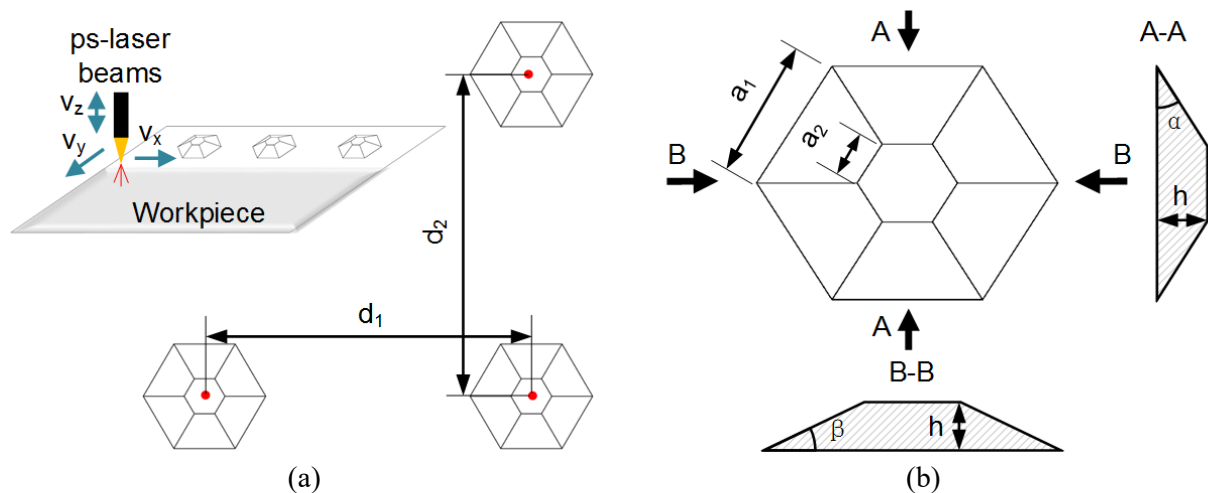


Figure 4-3. (a) Schematic illustration of pyramid production using ultra-short pulse laser beams, (b) geometrical design of single hexagonal pyramid

Table 4-7. Quantification of the honing stone B151 and surface topography design of the WC-CoNi hardmetal sample

Sample	Grain quantity	Sample surface ($\times 10^7 \mu\text{m}^2$)	Total grain surface area ($\times 10^6 \mu\text{m}^2$)	Phase ratio	Grain shape
B151	355	4.2	3.8	8.9%	Most varying from rectangle to hexagon
Hardmetal	343	6	5	8.3%	Hexagon

Table 4-7 compares the grain quantification result of the honing stone B151 with the surface topography design of the WC-CoNi hardmetal sample. There are 355 grains on the honing stone surface of $4.2 \times 10^7 \mu\text{m}^2$. The phase fraction of the grains is 8.9%. Average grain surface area is $10.6 \times 10^3 \mu\text{m}^2$. The majority of the grains have the shape varying from rectangle to hexagon. The surface topography of the WC-CoNi hardmetal sample is simulated from the honing stone B151, therefore, the quantification of the hexagonal pyramids is approximately similar to that of the honing stone B151. The hardmetal sample has a surface area of $6 \times 10^7 \mu\text{m}^2$. Each pyramid has a surface area S_1 of $14.6 \times 10^3 \mu\text{m}^2$ at the bottom and S_2 of $1.6 \times 10^3 \mu\text{m}^2$ at the top. Thus, all the 343 grains account for 8.4% of the entire surface. The hexagonal pyramids are regularly distributed along the X- and Y- axis with the intervals d_1 and d_2 of 400 μm in both directions. They have a side length a_1 of 75 μm at the bottom, a_2 of 25 μm at the top and a height h of 25 μm . The angle α between the bottom and the slope at the measuring position A-A is 30° and the angle β is 26.6° at B-B. The geometrical design of the hexagonal pyramids is shown in Table 4-8.

Table 4-8 Geometrical design of the hexagon pyramids

d_1 (μm)	d_2 (μm)	S_1 ($\times 10^3 \mu\text{m}^2$)*	S_2 ($\times 10^3 \mu\text{m}^2$)*	h (μm)	α ($^\circ$)	β ($^\circ$)
400	400	14.6	1.6	25	30	26.6

$$* S = \frac{3}{2}\sqrt{3}a^2, a_1 = 75 \mu\text{m}, a_2 = 25 \mu\text{m}$$

Square pyramids

Square pyramids with flat top have also been produced on the surfaces of WC-CoNi hardmetal using the identical machining parameters as the hexagonal pyramids (Table 4-4 and Table 4-6). In total 329 square pyramids are produced on the surface of $20 \times 3 \text{ mm}^2$. The geometrical design of the square pyramids is shown in Figure 4-4. The square pyramids have been arranged along the X- and Y- axis with identical intervals d_1 and d_2 of 400 mm, and each square pyramid has the same dimension, described by the following parameters:

- d_1 : the interval between two adjacent hexagonal pyramids along the x-axis
- d_2 : the interval between two adjacent hexagonal pyramids along the y-axis
- a_1 : the bottom side length of the square pyramid
- a_2 : the top side length of the square pyramid
- S_1 : the surface area of the pyramid bottom
- S_2 : the surface area of the pyramid top
- h : the height the square pyramid
- α : the slope at the measuring position A-A
- β : the slope at the measuring position B-B

The geometrical design of the square pyramids is listed in Table 4-9. The lengths of two sides at the bottom and the top a_1 and a_2 are 70 μm and 15 μm , respectively. The height h of the square pyramid is 25 μm and the slop angles α and β at the position A-A and B-B are 42.3° and 32.7° , respectively. Knowing the side lengths, the surface area of the bottom and the top S_1 and S_2 can be obtained: $4.9 \times 10^3 \mu\text{m}^2$ and 0.2×10^3

μm^2 . Table 4-10 shows the surface topography design of the sample. 329 grains should be produced on the surface of $6 \times 10^7 \mu\text{m}^2$, and all the grains have the surface area of $1.6 \times 10^6 \mu\text{m}^2$, and account for 2.7% of the entire sample surface.

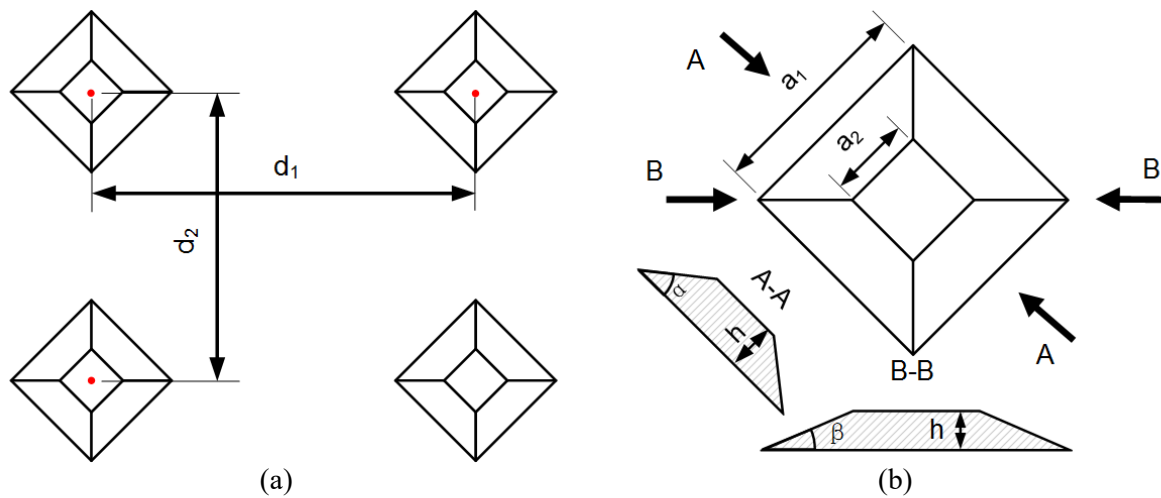


Figure 4-4. (a) Array arrangement of the square pyramids on the hardmetal surface, (b) geometrical design of single square pyramid

Table 4-9. Geometrical properties of single square pyramid

d_1 (μm)	d_2 (μm)	S_1 ($\times 10^3 \mu\text{m}^2$)*	S_2 ($\times 10^3 \mu\text{m}^2$)*	h (μm)	α ($^\circ$)	β ($^\circ$)
400	400	4.9	0.2	25	42.3	32.7

$$* S = a^2, a_1 = 70 \mu\text{m}, a_2 = 15 \mu\text{m}$$

Table 4-10. Surface topography design of the sample with the square pyramids

Grain amount	Grain shape	Sample surface area ($\times 10^7 \mu\text{m}^2$)	Total grain surface area ($\times 10^6 \mu\text{m}^2$)	Phase ratio
329	Square	6	1.6	2.7%

4.2 Surface integrity assessment after surface modification

Surface integrity describes the surface condition of the workpiece after being modified by a manufacturing process [17,100]. The consequence of these modifications might be a mechanical engineering design problem, but the preservation of those properties is considered as a manufacturing issue. Surface integrity can have great impact on the functionality of a component. For example, the alloy Inconel 718 can have a fatigue limit as high as 540 MPa after a gentle grinding or as low as 150 MPa after electrical discharge machining (EDM) [101]. The surface integrity assessment is focused on two aspects: surface topography characterization and microstructural changes within the surface layer (induced damage) [16,102]. The surface integrity assessment of laser-textured surfaces aims to characterize the geometrical properties of the produced structures and to investigate the influence of the treatment on the microstructural changes or to identify the induced surface damages. Laser scanning microscope (LSM) is mainly used to characterize the geometrical properties since it has high three-dimensional imaging capacity. Scanning electron microscopy

(SEM) in combination with focused ion beams (FIB) is used to analyze the surface layer damage.

4.2.1 Surface integrity assessment of the patterns for tribological application

Line-like patterns

Line-like patterns are produced by the two-beam interference using a nanosecond laser (LIMET) and they cover the entire surface of specimen in square arrangement. Three important geometrical properties are characterized: periodicity, height, and peak angle. It is found that the line-like pattern (Figure 4-5) has a periodicity of 11.8 μm and height of 0.6 μm .

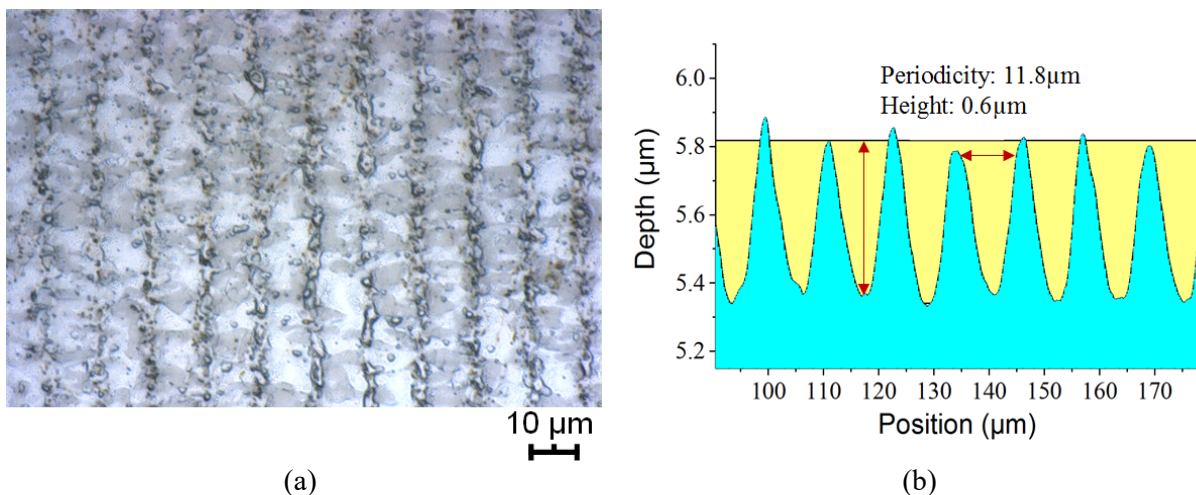


Figure 4-5. (a) LSM image and (b) cross-sectional plots of the line-like pattern

Figure 4-6 shows the microstructural investigation of the line-like patterns. The superposition of the two laser beams leads to a periodical energy input with laser intensity minima and maxima positions. At the position of maximum laser intensity, the underlying material is melted. Due to surface temperature and tension gradient, the material is shifted from the hot to the cold regions (minimum laser intensity). In Figure 4-6(a), the line-like pattern is not continuous, but rather interrupted. The cross-section shows that the patterns have a wavy profile (Figure 4-6(b)). An enlarged view of the cross-section at a topographic maximum position (Figure 4-6(c)) reveals that the lack of binder produces discontinuities. The remaining WC recrystallizes and produces the maxima. This behavior can be traced back to the lower binder melting and vaporization temperatures [54], which lead the binder to be ablated at first. Therefore, the binder is melted and vaporized whereas the WC grains are just slightly melted but not vaporized, since the used fluence 2.3 J/cm² is not sufficient to vaporize both components [55,56]. Cracks as well as some pores, which were formed by the binder vaporization and thermal residual stress, can be observed in Figure 4-6(d). A local cross-section was done by FIB in order to study the micro-structural changes after laser processing. Figure 4-6(e) provides an overview of the cross-section, whereas in the enlarged view (Figure 4-6(f)) no evident thermal defects can be found. Only a very thin film (less than 0.2 μm) is visible at the surface, which differs from the

initial surface morphology. It might be the oxidation layer induced by the thermal diffusion [46, 103]. The oxidation layer appears at the topographic minimum position of the line-like pattern, which suggests that the heat diffusion is more evident at the maximum laser intensity position.

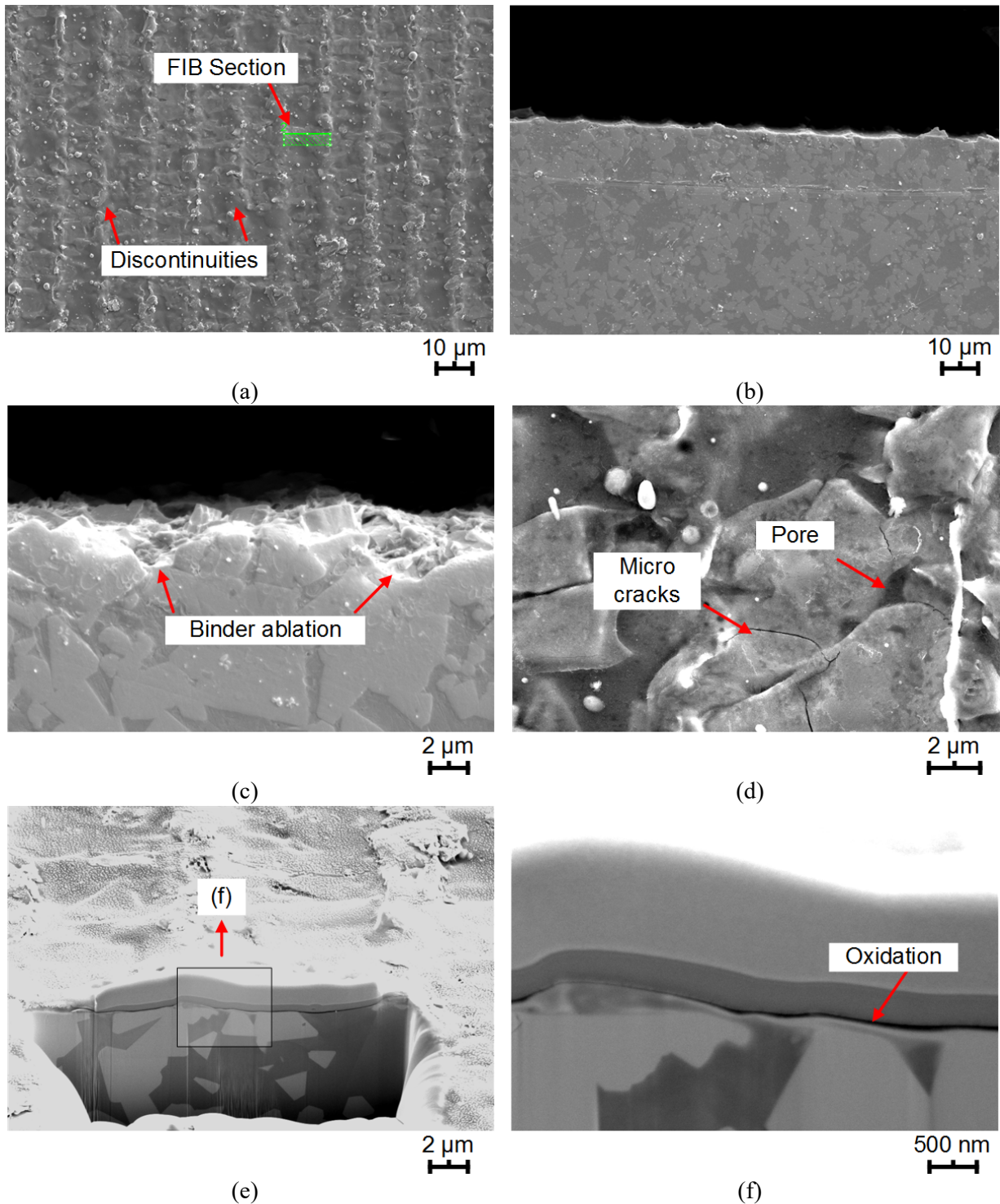


Figure 4-6. Microstructural investigation of the line-like surface pattern: (a) overview, (b) cross-section, (c) enlarged view of the cross-section, (d) induced defects, (e) FIB cross-section, (f) enlarged view of the FIB cross-section

Dimples produced by ps-laser

Three geometrical properties of the dimples produced by ps-laser were characterized (Figure 4-7): interval, defined as the distance between the centers of two adjacent dimples; depth, defined as the distance between the dimple upper surface and its bottom; and dimple diameter. Five measurements were conducted, and it is found that the dimples have an average interval of 505.5 μm , depth of 3.8 μm and diameter of 52.3 μm (Table 4-11).

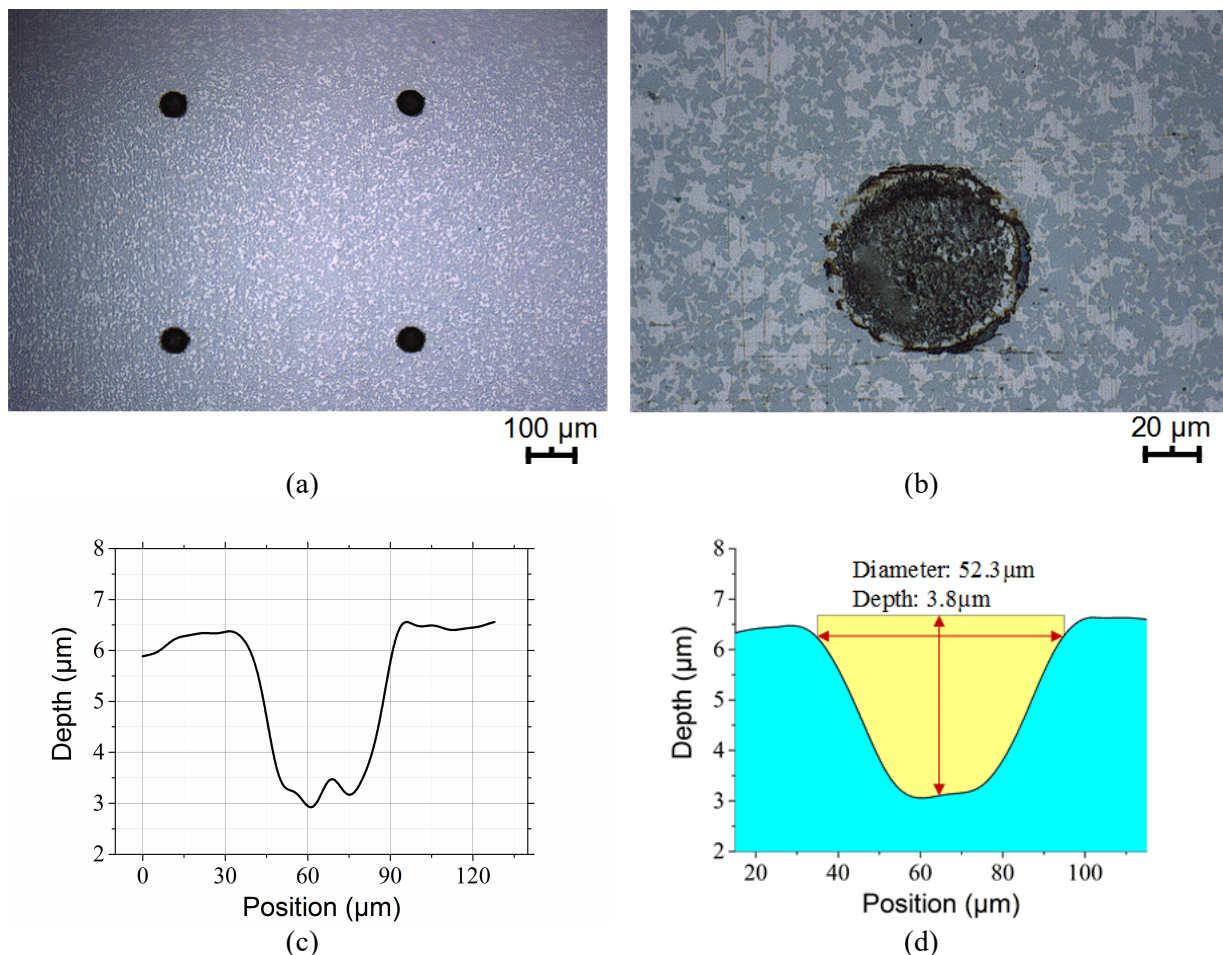


Figure 4-7. LSM images and cross-sectional plots of geometrical properties of surface patterns: (a) arrangement, (b) single dimple, (c) cross section, (d) geometric characterization

Table 4-11. Geometrical property measurements of the dimples produced by ps-laser

Measurement	Diameter (μm)	Depth (μm)	Interval (μm)
1	55.6	3.1	502.5
2	52	3.2	505
3	51.3	3.5	502.5
4	48.6	4.5	507.5
5	53.8	5	510
Average	52.3	3.8	505.5

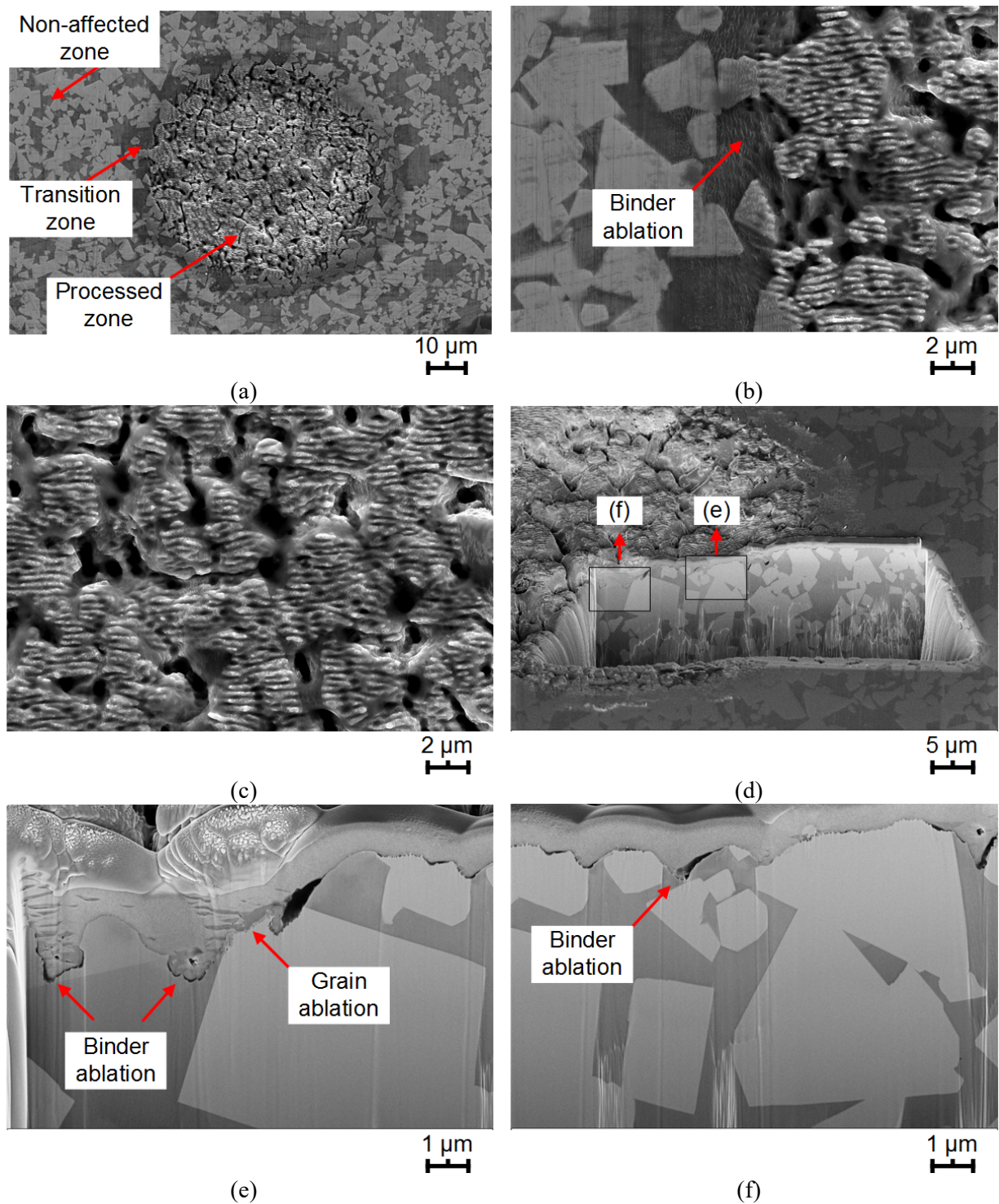


Figure 4-8. Microstructural investigation of the dimples: (a) overview, (b) transition zone, (c) enlarged view of the processed zone, (d) FIB cross-section, (e) enlarged view in the transition zone, (f) enlarged view in the processed zone

Surface integrity of the produced dimples has been assessed by SEM/FIB. Three zones can be discerned (Figure 4-8(a)): non-affected, transition and processed zones. The non-affected zone is situated outside of the laser spot. The transition zone, situated between the non-affected zone and the processed zone (Figure 4-8(b)), is about 3-5 μm wide. The binder is found to have been slightly melted and more affected than WC grains in the transition zone. The material in this zone is not

directly ablated from the laser beams but rather from the thermal effects, such as heat diffusion from the processed zone. The heat affected zone can often be observed in the laser welding processes. The zone width depends on many parameters, such as the material parameters, laser pulse duration, repetition rate, etc. In general, ultra-short pulse can effectively diminish or avoid the heat affected zone [46,104]. In the center of the dimples (Figure 4-8(c)), the binder is completely removed. It is remarkable that the remaining WC grains form a skeleton structure. Thus, some pores can be found between adjacent WC grains. On the WC grains, some stripes can be observed. These stripes are named laser-induced periodic surface structures (LIPPSSs), which are often observed with a period slightly less than the incident laser wavelength for metals. It is reported that they are usually oriented perpendicular to the polarization of the laser beams and produced by the interference of the surface-electromagnetic waves induced by incident laser beams [105-107].

The FIB cross-section reveals the microstructure under the processed surface. The section has a dimension of $60 \times 15 \times 10 \mu\text{m}^3$ (Figure 4-8(d)), covering the aforementioned three zones. In the transition zone (Figure 4-8(e)), the sectional analysis shows that WC grains have been less ablated than the binder under this machining condition. The binder between WC grains is gradually ablated by the laser beams. In the processed zone (Figure 4-8(f)), both binder and WC grains have been ablated and more evidently than in the transition zone. The binder ablation is about $2 \mu\text{m}$ in the processed zone, and less than $1 \mu\text{m}$ in the transition zone. Thus the surface appears a relatively rough topography and a skeleton structure is formed.

Dimples produced by fs-laser

The geometrical properties of the dimpled patterns produced by fs-laser are characterized by LSM (Figure 4-9(a)). The diameter, the depth and the interval between the dimples were measured. It is found that the depth is roughly $3.5 \mu\text{m}$. The distance between two adjacent dimples is approximately $500 \mu\text{m}$. The diameter of the dimple is about $150 \mu\text{m}$ (Figure 4-9(b)).

The surface integrity is assessed by SEM (Figure 4-10), and three zones can be found: non-affected, transition and processed regions (Figure 4-10(a)). It can be observed that the zone boundaries are rather blurred. The dimple border has a circular form, but in some parts, the border is blurred and interrupted (Figure 4-10(b)). In the processed zone, some mixture can be found, and it might be the re-deposition of material after ablation. A well pronounced boundary between the processed zone and the transition zone can be observed in Figure 4-10(c). However, some cracks and pores are still found in this region because the grains are sensitive to the local temperature increase (Figure 4-10(d)).

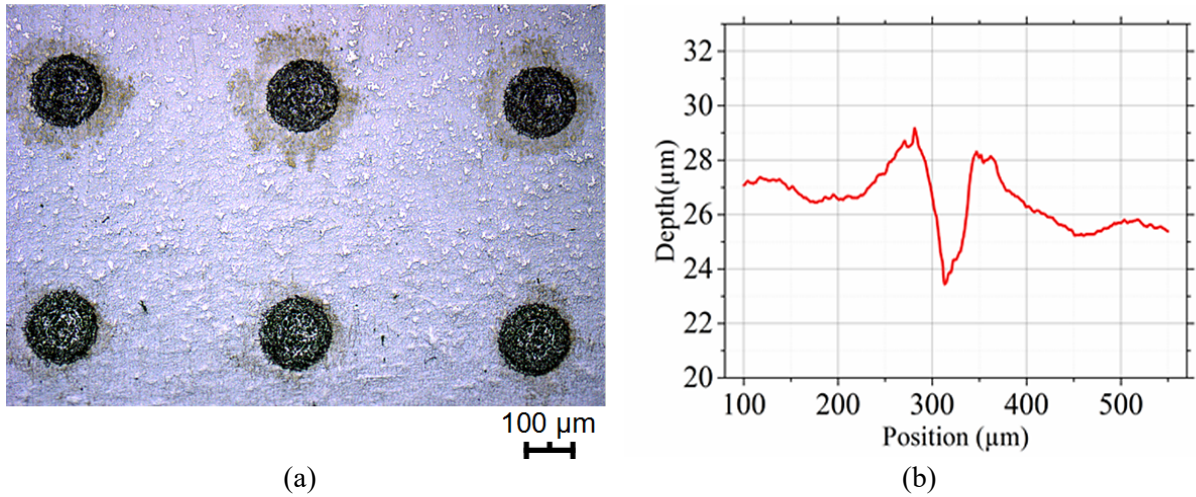


Figure 4-9. Patterned dimples by ultra-short pulsed laser processing on the WC-CoNi surface: (a) arrangement, (b) cross-section

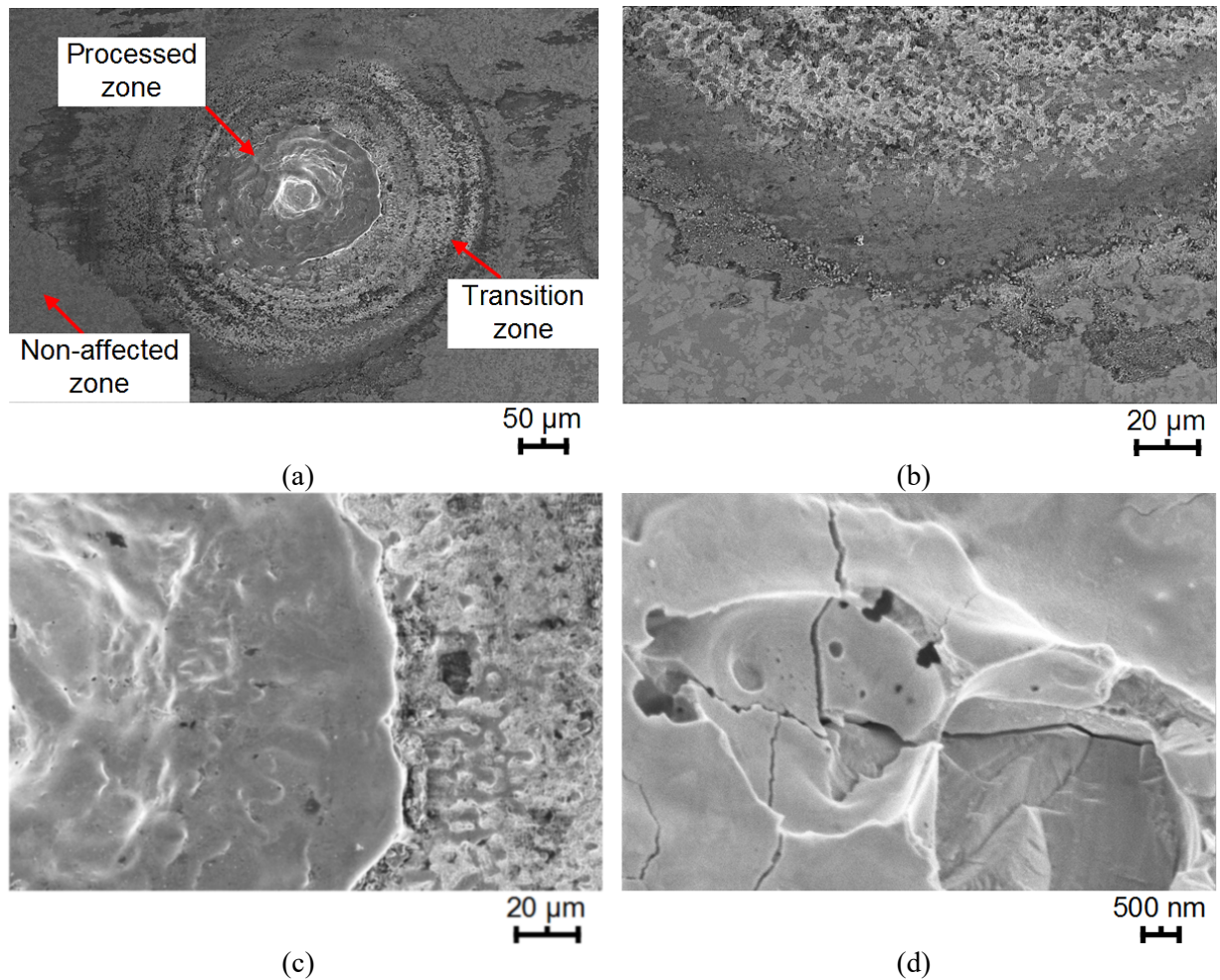


Figure 4-10. Surface integrity investigation of dimples (SEM): (a) overview, (b) non-affected zone, (c) transition zone, (d) processed zone

The morphology of the dimples produced by fs-laser is not as regular as those produced by ps-laser combined with the micromachining center. The observation can be explained by the following reasons. Firstly, the morphological irregularities of the dimples might have been strongly influenced by the homogeneity of the laser spot.

The intensity distribution of the laser beam should usually have a Gaussian profile, and the center of the laser spot should have the highest intensity. However, in practice it is difficult to obtain such highest intensity point locating exactly in the spot center. Secondly, the laser beam should perpendicularly incident the sample surface to obtain a circular form, but it is implicitly difficult to obtain an incident angle of 90° using the auto-stage, which may result in the form deviation. Moreover, the structure can also be influenced by the surface condition which affects the absorption of the energy, e.g., surface impurities or contaminations can also change the absorption characteristic and provoke some unexpected defaults such as cracks.

Grooves produced by ps-laser

The grooves are produced using ps-laser integrated in the 5-axis micromachining system. They are arranged horizontally on the surface of the WC-CoNi hardmetal sample (Figure 4-11(a)). The geometrical properties were characterized using three parameters: width, depth and interval (Figure 4-11(b) and (c)).

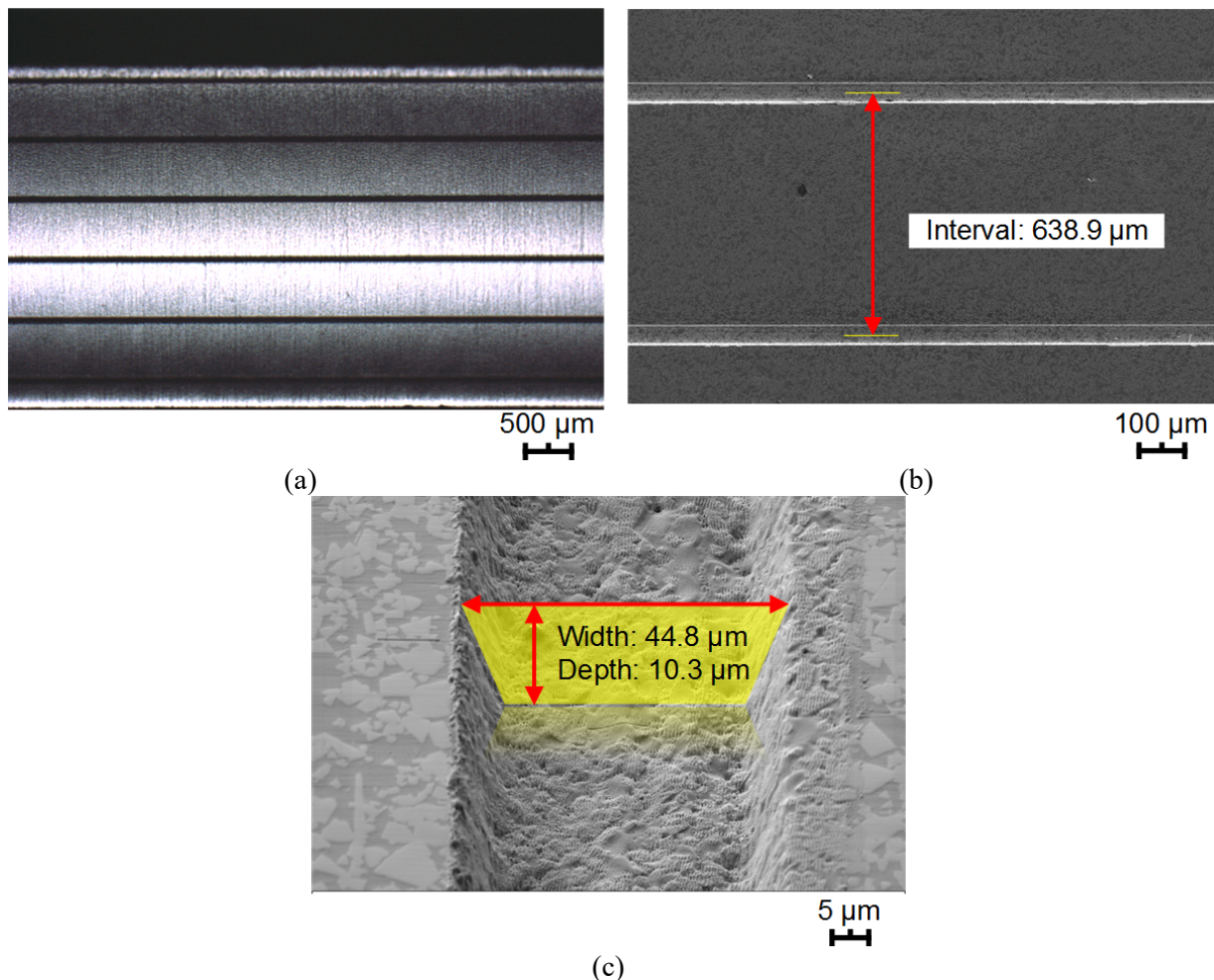


Figure 4-11. Grooves produced on the surface of the WC-CoNi hardmetal sample using ps-laser: (a) horizontal grooves (LSM), (b) and (c) geometric properties (SEM)

Width is the distance between the two borders of the groove. Depth is the distance between the top and the bottom of the groove. Interval is the distance between the middle lines of two adjacent grooves. Five measurements have been carried out. The

geometrical characterization results are shown in Table 4-12. The average value of the interval is 638.9 μm , the average width of the groove is 44.8 μm and the average depth is 10.3 μm .

Table 4-12. Geometrical property measurements of the grooves produced by ps-laser

Measurement	Width (μm)	Depth (μm)	Interval (μm)
1	44.6	9.9	613.4
2	44.3	10.51	629.8
3	44.8	10.2	641.8
4	45.1	10.6	645.4
5	45.4	10.2	663.9
Average	44.8	10.3	638.9

Surface integrity assessment has been conducted using SEM in order to inspect the influences of laser beams at the sublayer. Figure 4-12(a) shows an overview of one groove. Three zones are clearly identified. The processed zone is situated in the middle between two white blur lines. The white blur lines are the borders of the grooves, which are slightly declined from the top to the bottom of the groove. The slopes of the borders and together with their adjacent regions constitute the transition zone. The region, which is not processed by laser, is the non-processed zone. Figure 4-12(b) shows a zoom of the processed zone center. Two phases (WC grains and binder) can be identified. The binder, which filled the gap between the grains, has been ablated, and some stripes are formed on the grain surfaces, and they are the laser-induced periodic surface structures (LIPPSSs) [105-107]. Grain edges are quite clear in this zone, which indicates that the binder and grains were removed differently by the laser beams. It is easier to ablate the binder than the grains, since the binder (Co+Ni) has lower melting and vaporization points [46].

Figure 4-12(c) is a zoomed image of the transition zone, and the image has been taken with a tilted angle to assure that it is perpendicular to the slope surface. The slope surface exhibits a blurred status, where the two phases cannot be discerned any more. The surface is covered by a layer of unclearness situated between two borders of the slopes. The upside of the slope is the top of the groove, and the downside is the bottom of the groove. The blurred surface results from the spot shape of the laser beam, which has a spherical form with a diameter of 11 μm . In the ablation processes, only the edge of the laser spot was contacting the groove borders, which lead the groove border not perpendicular to the bottom. In addition, along with the sinking of the laser beams, the material on the border has been processed repetitively in short time. Binder seems to be not completely vaporized in this region, since the edge of the laser spot has lower energy intensity and this made the surface look rather blurred. The upper part of Figure 4-12(d) shows the details of the non-affected zone and its transition to the processed zone as well. The stripes on the WC grains offer a clear boundary to distinguish the zones.

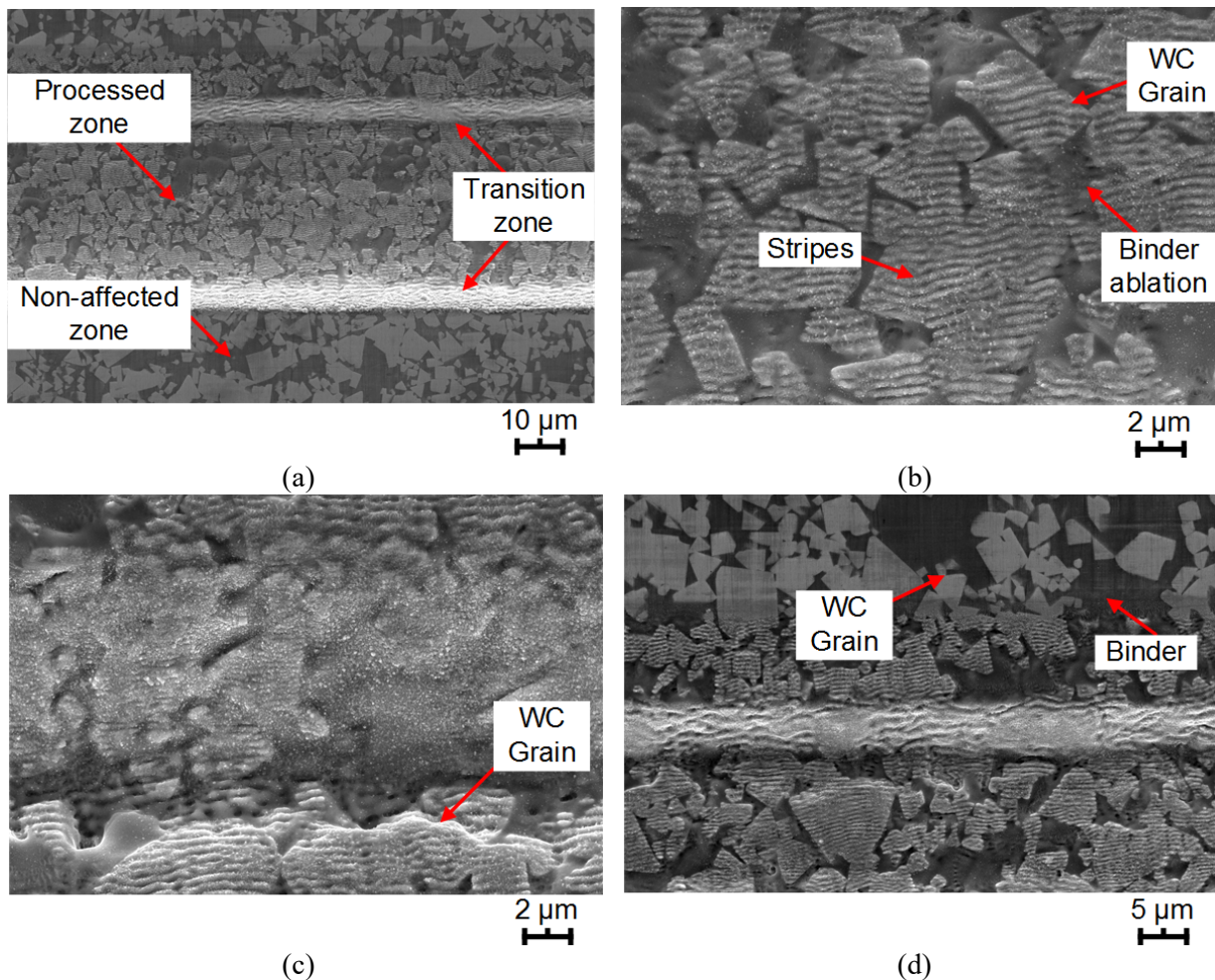


Figure 4-12. Surface integrity assessment of produced grooves (SEM): (a) overview, (b) processed zone, (c) transition zone (d) non-affected zone

Cross sectional analysis using FIB has been conducted on the groove, and the cross section covers the three aforementioned three zones with the dimension of $60 \times 6 \times 10 \mu\text{m}^3$ (Figure 4-13(a)). A thin film of platinum was deposited on the surface in order to offer a reference of the cutting edge. Figure 4-13(b) is a zoomed image of the processed zone. Two phases (grains and binder) can be found clearly at the sub-layer. The ablation of the binder was smooth but serrated forms were produced on the grain surface, which appeared as strips on the SEM image. Figure 4-13(c) shows more details of the transition zone and the non-affected zone. The slope of the groove board is clear to be identified. The boundary between the transition zone and the non-affected zone can also be identified according to the serrated form on the grain surface. In the Figure 4-13(d), the width of the stripes has been measured to be 408.7 nm, smaller than the wavelength 532 nm of laser beams. The surface integrity analysis using SEM and FIB proves that the grooves produced by ps-laser have good geometric precision and continuity, and there is no obvious thermal defects induced in each zone during the laser processing such as cracks and pores. The induced stripes on the WC grains do not penetrate into the sub-layer of the grooves.

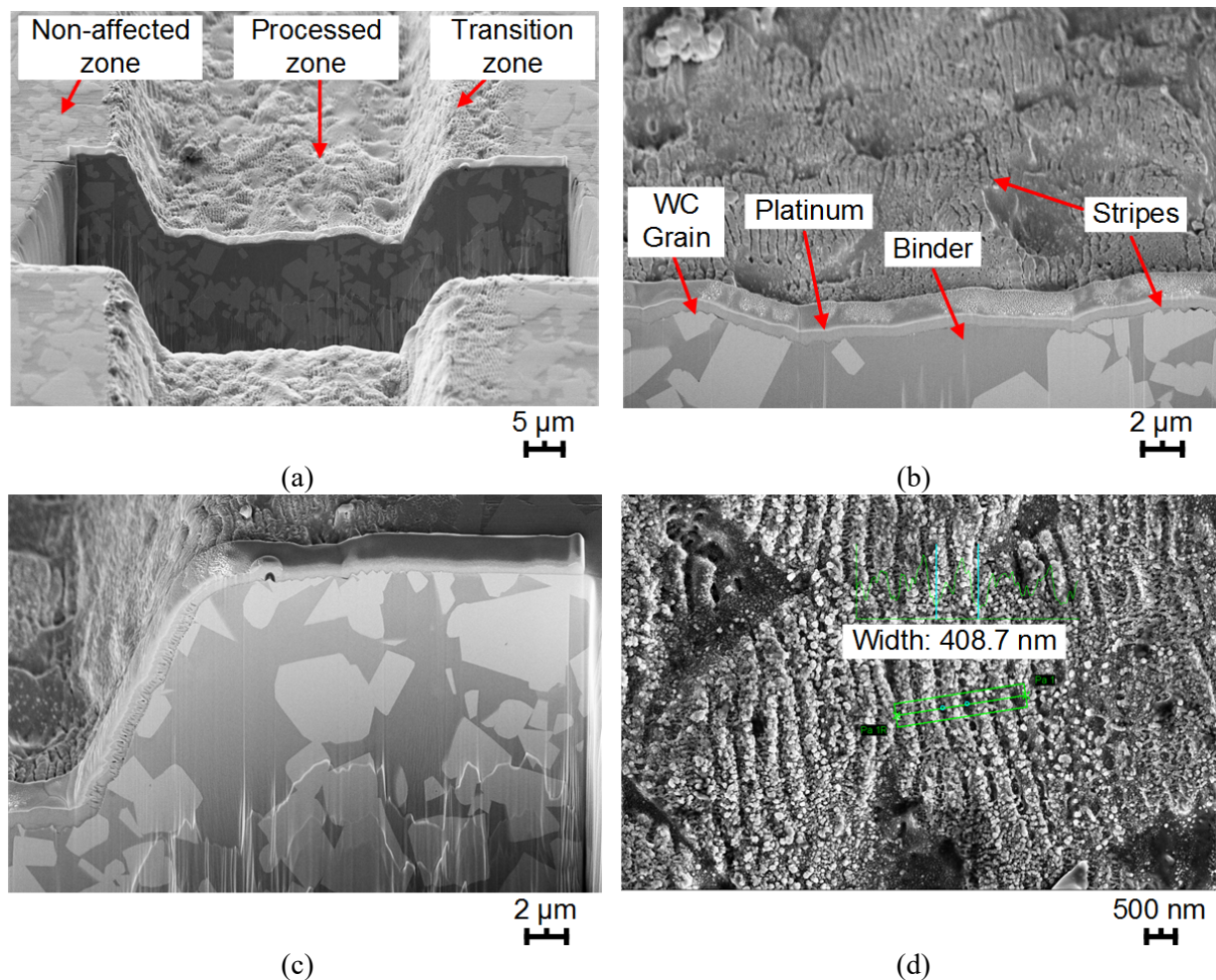


Figure 4-13. FIB cross sectional analysis of produced grooves: (a) cross section, (b) processed zone, (c) transition zone and (d) zoomed processed zone

Grooves produced by fs-laser

The grooves were produced using fs-laser with the auto-stage. The specimen is fixed on the auto-stage which can move at certain speed along the X- and Y- axis. The geometrical properties of the produced patterns have been characterized using LSM. The groove has a width of 100 μm and depth of 1.8 μm (Figure 4-14).

Three zones can be identified from the overview (Figure 4-15(a)). The processed zone is situated in the center and has the width of 100 μm . The affected zones can be found at both sides of the processed zone having a width of 25 μm . The transition zone is much larger than that of grooves produced by the ps-laser, since the laser spot of the fs-laser is not as homogenous as that of the ps-laser and the incident angle of laser beam may have a certain deviation from 90°. In Figure 4-15(b), it can be seen that the processed zone appears to be blurred and to be covered by a layer of unclarity. Figure 4-15(c) shows the FIB cross-section in the processed zone, which has a dimension of 50×10×6 μm^3 . It has been found that a thin oxidation layer covering the processed zone and it has a thickness of about 1 μm in Figure 4-15(d). No obvious defects have been detected under the oxidation layer.

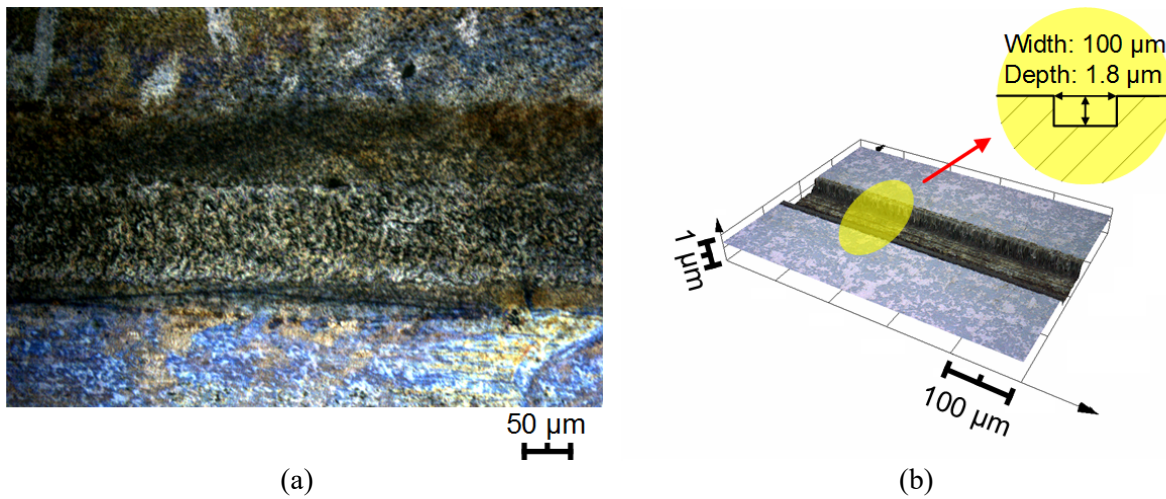


Figure 4-14. (a) LSM image and (b) cross-sectional plots of the groove produced by fs-laser

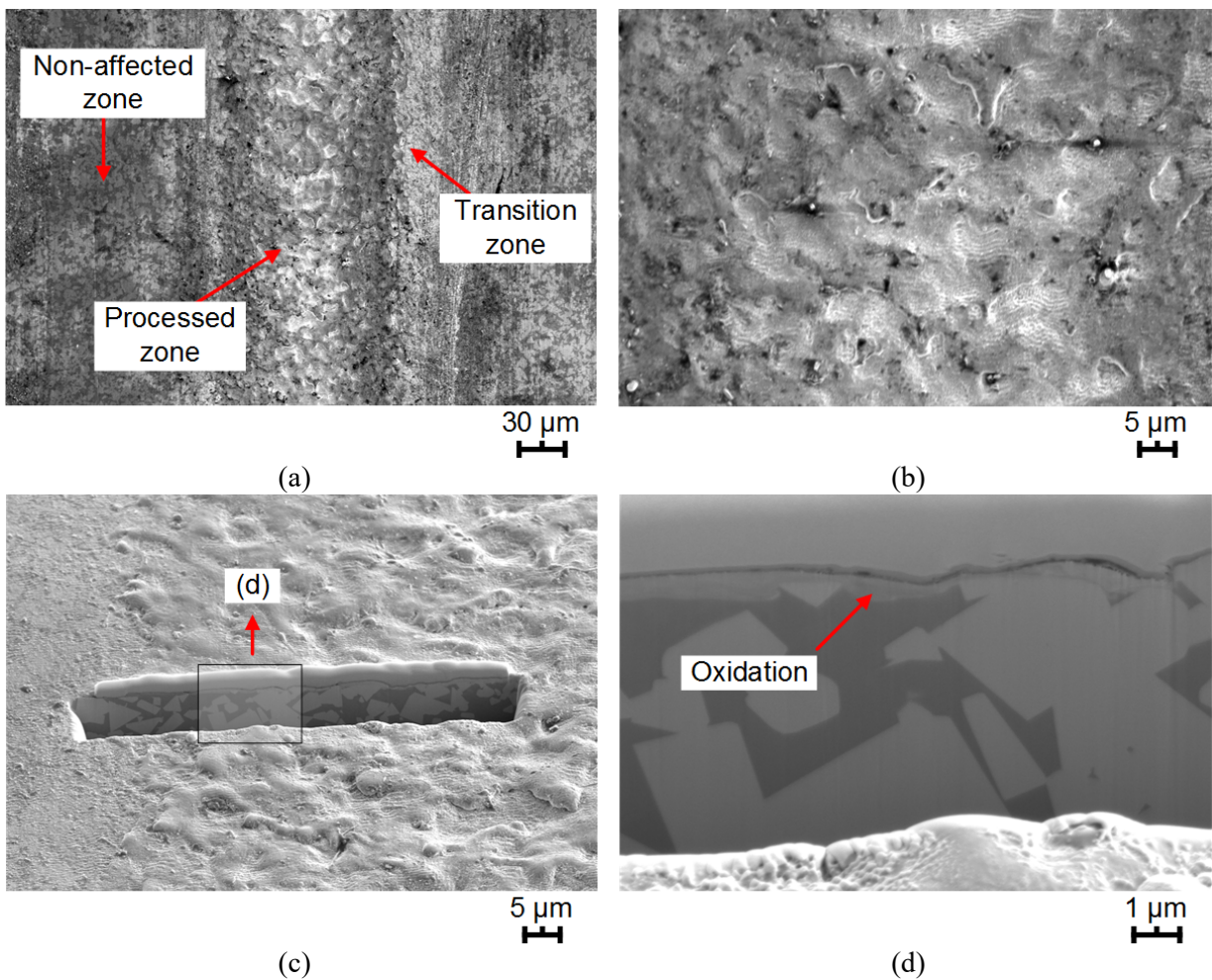


Figure 4-15. Microstructural investigation of the grooves produced by fs-laser: (a) overview, (b) enlarged view of the processed zone, (c) FIB cross-section, (d) enlarged view of the FIB cross-section

4.2.2 Surface integrity assessment of the patterns for abrasive application

Hexagonal pyramids

Hexagonal pyramids have been produced using the ps-laser set-up, aiming towards the reproduction of similar surface topography of a traditional CBN honing stone on WC-CoNi hardmetal surfaces.

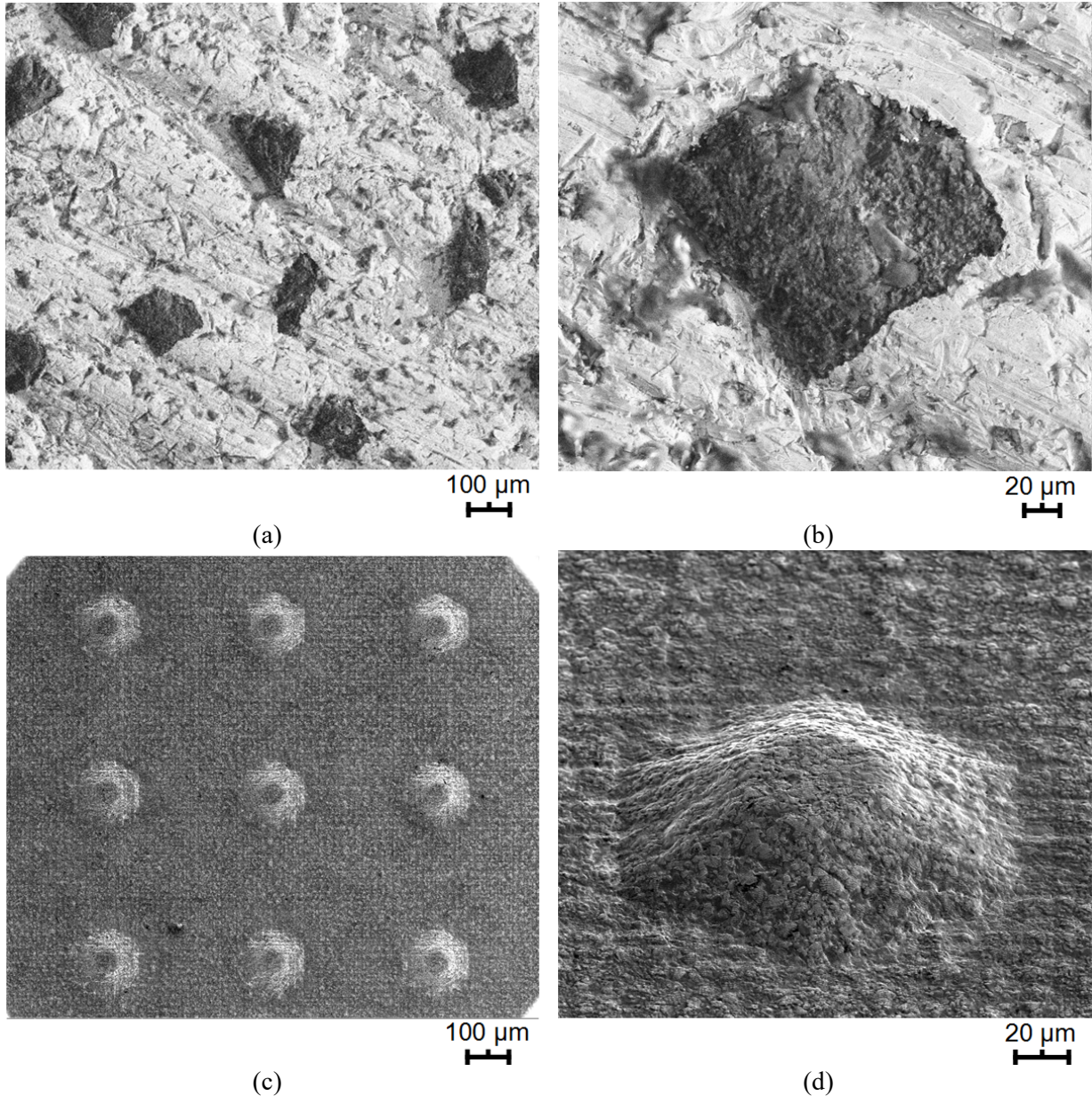


Figure 4-16. Surface inspection of CBN honing stone B151: (a) grain distribution, (b) single CBN grain on the surface; geometrical properties of hexagonal pyramids: (c) arrangement of produced hexagonal pyramids, (d) single hexagonal pyramid (images taken by SEM)

Figure 4-16(a) and (b) show the surface inspection of the CBN honing stone B151 by SEM and one single CBN grain profile. The arrangements of the produced hexagonal pyramids and the profile of one single pyramid on the WC-CoNi hardmetal sample surface are shown in Figures 4-16(c) and (d). These SEM images correspond to the shaped patterns as well as to one specific hexagonal pyramid.

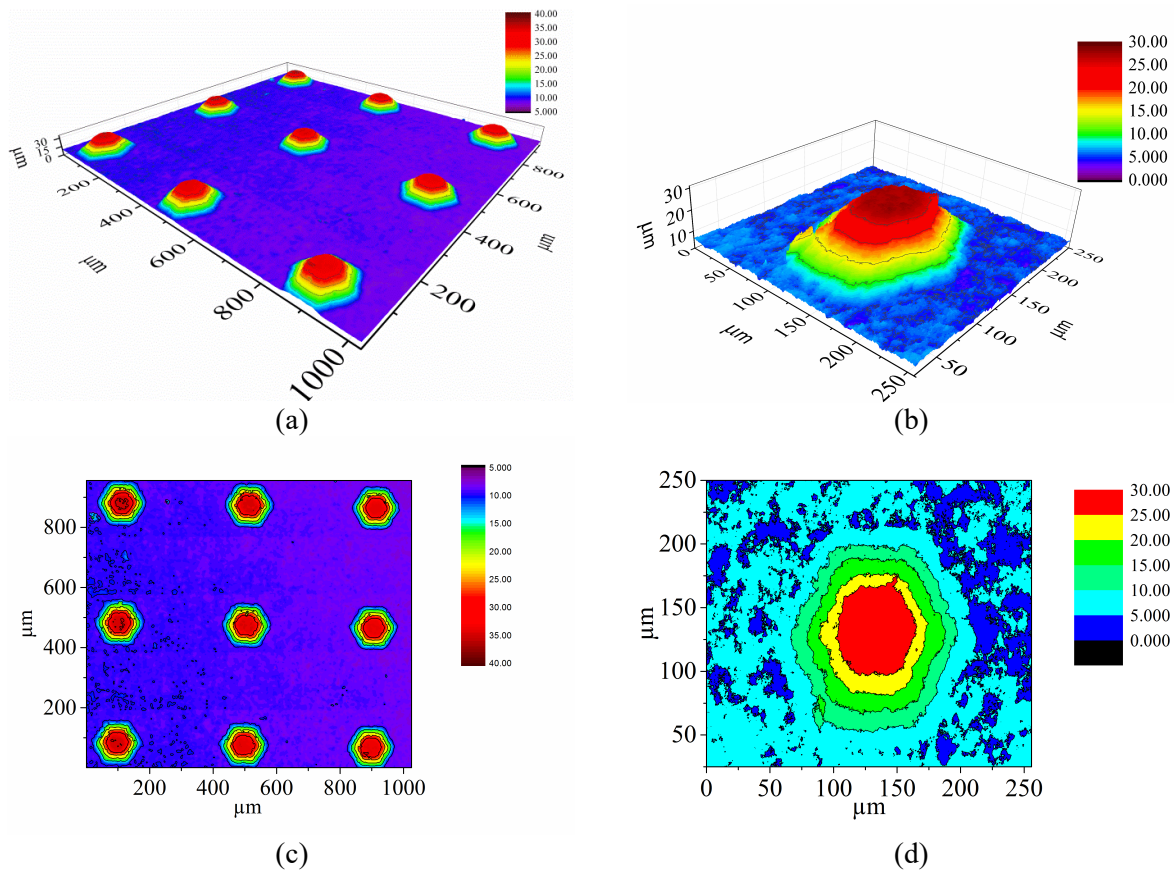


Figure 4-17. Surface topography reconstruction using Origin 9.0: (a) and (c) arrangement and projection of produced hexagonal pyramids, (b) and (d) single hexagonal and its projection

On the other hand, topography reconstructions (on the basis of LSM experimentally gathered data and subsequent analysis using the software Origin 9.0) of the surface features previously shown are given in Figure 4-17. The scanned surface area is $1024 \mu\text{m} \times 1024 \mu\text{m}$, where 9 pyramids have been measured and the coordination of their profiles were recorded (Figure 4-17(a)). The 9 pyramids are evenly distributed on the surface with identical distance, and the hexagonal shapes can be well distinguished according to the contour lines (Figure 4-17(c)). The contour lines indicate that the slopes at each side of the hexagon pyramid are quite smooth. The profile of a single hexagonal pyramid and its projection are shown in Figures 4-17(b) and (d) to explain the measurements of their geometrical properties. It is found that the height h of the pyramid is $25.4 \mu\text{m}$ (measured from the bottom center to the top center). The length of each side of the hexagon pyramid is roughly equal to $75 \mu\text{m}$ at the bottom and $30 \mu\text{m}$ at the top.

Figure 4-18(a) shows the projection of one single hexagonal pyramid. Three regions may be identified: top, inclined (slope) and bottom. Top (red) and bottom (light blue) are flat, and they are connected by an inclined surface (green). Cross-section views at positions A-A and B-B enable to measure slope angles (Figures 4-18(b) and (c)).

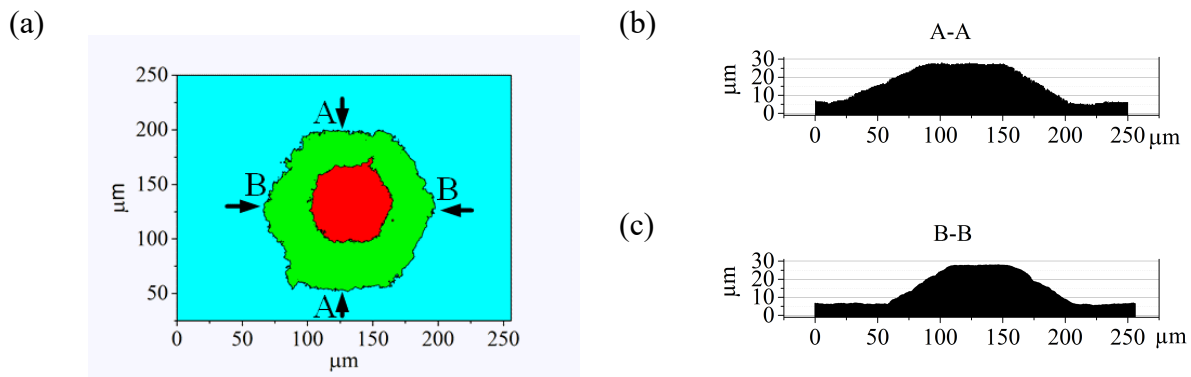


Figure 4-18. (a) Projection of a single hexagonal pyramid, (b) and (c) cross-section views at positions A-A and B-B, respectively

Five measurements were carried out and all the parameters described in Figure 4-3(b) (on Page 48) are determined. Table 4-13 summarizes the geometrical characterization of the produced hexagonal pyramid patterns. Laser-induced patterns consist of hexagonal pyramids located regularly along the X- and Y- axis with average intervals d_1 of 404.5 μm and d_2 of 403.5 μm , as measured between adjacent pyramid centers. Furthermore, hexagonal pyramids exhibit average side lengths a_1 and a_2 of 63.7 μm and 31.1 μm respectively, average height h of 21.6 μm , and areas S_1 of $9.1 \times 10^3 \mu\text{m}^2$ at the bottom and S_2 of $2.3 \times 10^3 \mu\text{m}^2$ at the top. Finally, average slope angles α (cross section A-A) and β (cross-section B-B) are 27.1° and 30.2° respectively.

Table 4-13. Summary of geometrical property measurements of the produced hexagonal pyramids

N°	d_1 (μm)	d_2 (μm)	a_1 (μm)	a_2 (μm)	S_1 (μm^2)	S_2 (μm^2)	h (μm)	α (°)	β (°)
1	401.7	401.7	61.8	30.4	9159.1	1952.4	20.9	26.6	28.8
2	406.0	405.5	68.0	28.5	8990.1	2420.8	19.4	27.0	31.1
3	404.8	403.2	63.7	29.9	8960.6	2173.0	22.3	26.4	30.1
4	406.3	403.0	61.9	33.7	9390.9	2594.0	21.8	27.9	30.7
5	403.6	404.3	63.1	33.0	9020.0	2437.1	23.7	27.7	30.2
Average	404.5	403.5	63.7	31.1	9104.1	2315.5	21.6	27.1	30.2

Figure 4-19 shows a comparison between aimed and experimentally attained surface topography. In general, a satisfactory agreement is found between outcome and aimed geometrical features. Concordance is outstanding regarding pattern geometry, as given by relative matching between aimed and experimental values for intervals d_1 and d_2 of about 99%. On the other hand, relative differences are somehow higher, although still within a range (15% to 25%) that defines agreement as fairly good, when comparing geometry parameters of single hexagonal pyramids. Relative discrepancies observed in surface area and slope values are also a direct consequence of the latter.

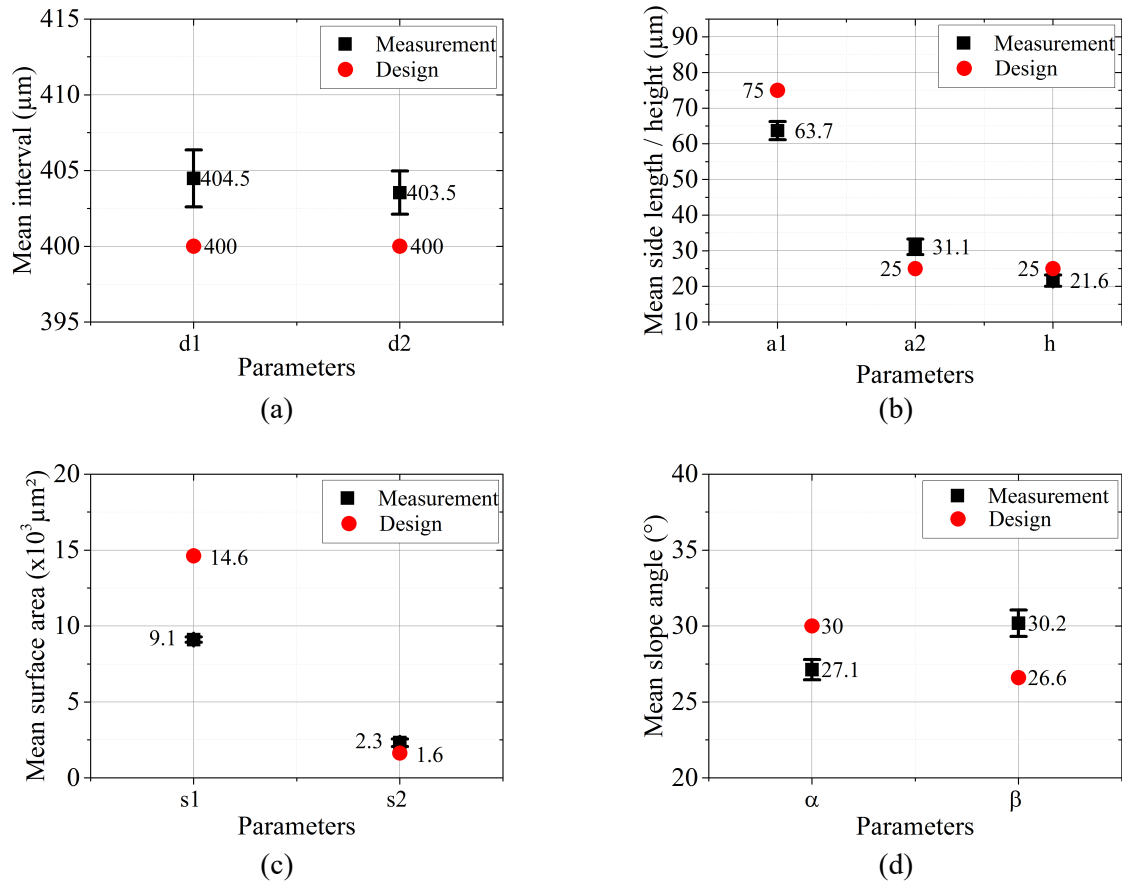


Figure 4-19. Comparison of aimed and experimentally attained surface topography features: (a) interval between adjacent pyramids; (b), (c) and (d) geometrical parameters of a single hexagonal pyramid

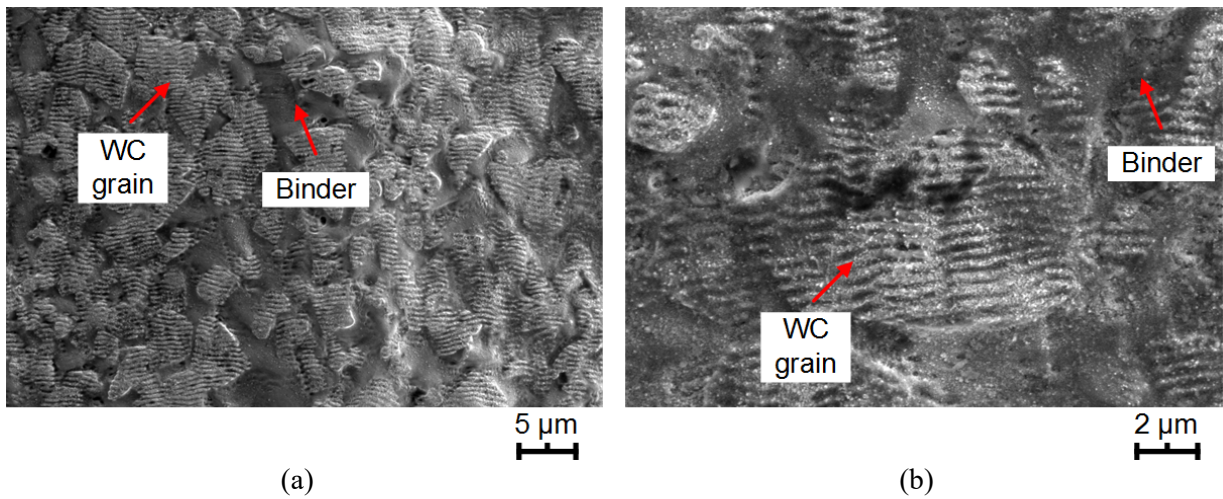


Figure 4-20. Pattern morphology (SEM): (a) pyramid top and slope, (b) pyramid bottom

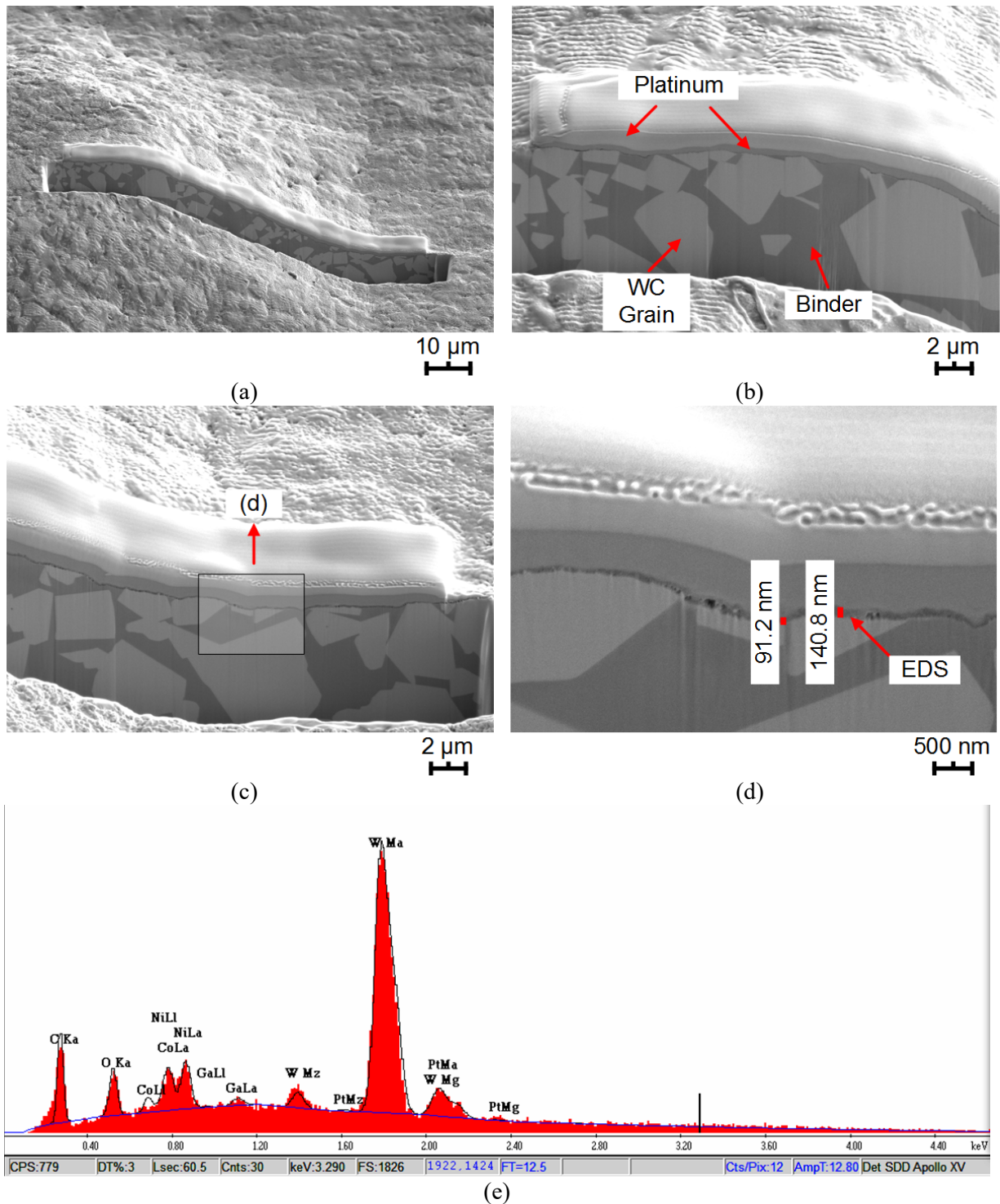


Figure 4-21. Cross sectional investigation of the hexagonal pyramid: (a) cross section position, (b) pyramid top, (c) pyramid bottom, (d) Oxidation layer, (e) EDS analysis of oxidation layer

Figure 4-20 shows the top and the bottom surfaces of a LST shaped hexagonal pyramid. Several observations may be done. First, both ceramic and metallic phases are completely and clearly discerned. This is different from the surface aspect attained after shaping of hardmetals with other conventional non-abrasive machining routes, e.g. EDM. Second, binder is found to have experienced more pronounced ablation than the WC grains. This finding may be rationalized on the basis of the relatively different melting and vaporization temperatures of the two phases (much lower for

the CoNi binder). Third, some stripes on the surface of WC grains are evidenced. These stripes are referred to as laser-induced periodic surface structures (LIPSSs), and they are produced by the interference of the surface-electromagnetic waves induced by incident laser beams. Fourth, coming back to the binder, it is observed that this phase becomes rather blurred especially at the bottom surface due to its melting and incomplete vaporization. This finding points out that some thermal reaction still exists, even under the picosecond mode. However, it is almost negligible, when compared to that documented as consequence of rough and/or fine-shaped EDM of cemented carbides (e.g., see Refs. [16,44]).

Such statement is further supported by the SEM image shown in Figure 4-21(a), corresponding to a FIB cross-section of one laser-shaped hexagonal pyramid. The cross section covers the top, slope and bottom of the pyramid. After the laser processing, the two basic phases of hardmetal (WC and binder) are still discernible according to the SEM image. On the top border, platinum has been deposited to offer the FIB cutting reference. Both WC grains and binder have been continuously ablated from the top of pyramid to its bottom. But it is remarkable that the binder suffered more ablation than the WC grains since the binder has lower melting and vaporization temperatures. It is also observed that the binder became rather blurred due to the thermal reaction. From these images (Figures 4-21(b-c)), it is clear that laser beam action does not affect the hardmetal subsurface. Accordingly, neither damage (cracks or pores) nor microstructural changes are discerned within the material bulk, even in regions just below the shaped surface. Between the platinum deposition and the border, a thin layer of about 100 nm thick has been detected (Figure 4-21(d)). The layer covers the entire top border of the cross section. The chemical composition of the layer has been analyzed by Energy-dispersive X-ray spectroscopy (EDS), indicating that the layer consists of the oxidation of WC grains and binder (Figure 4-21(e)). This observation points out a negligible influence of LST processing on the surface integrity of surface patterned hardmetals.

Square pyramids

Square pyramids have been produced on the surface of the WC-CoNi hardmetal samples using identical conditions of hexagonal pyramids, and they were also regularly distributed along the X- and Y- axis with identical interval. The designed geometrical properties of the square pyramids are listed in Table 4-9 (on Page 50).

Figure 4-22 shows the morphological characterization of the square pyramids using LSM. The arrangement of the pyramids is shown in Figure 4-22(a). Figure 4-22(b) shows the profile of a single square pyramid in 3D, and its square shape can be identified. The geometrical properties of the produced square pyramids have been characterized by means of surface topography reconstruction using Origin 9.0. Figures 4-23(a) and (b) illustrate the reconstructed 3D model of one single square pyramid and its projection along the Z-axis on the XY-plane. The contour lines on the model have square forms with approximately equal interval between each other at any position. This proves that the profile of the square pyramid is smooth. But slight

declination of the pyramid plane is observed in Figure 4-23(b), which could be induced in the polishing process or in the measurement.

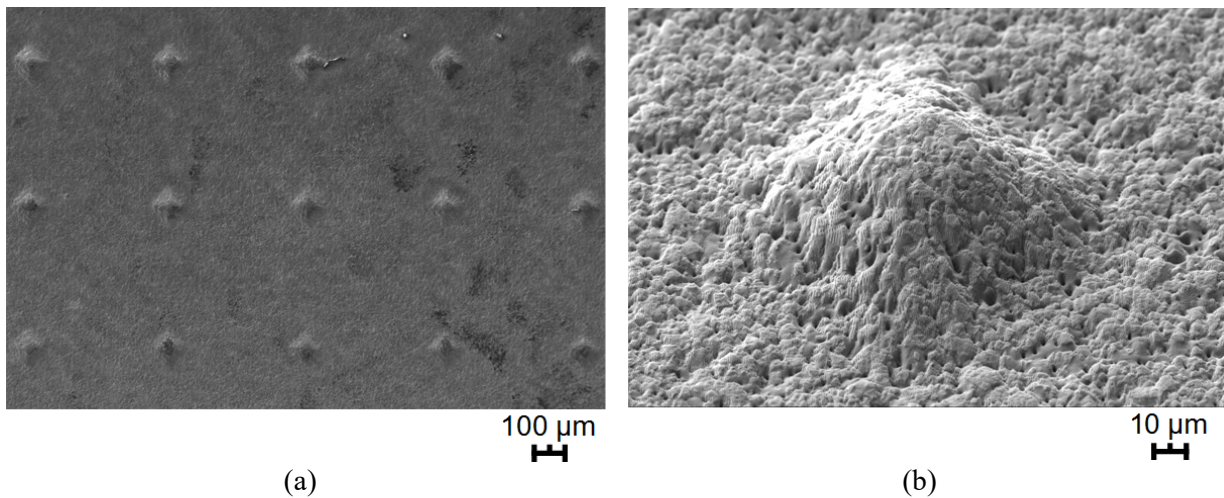


Figure 4-22. Morphological characterization of square pyramids by SEM: (a) arrangement of produced square pyramids, (b) single square pyramid

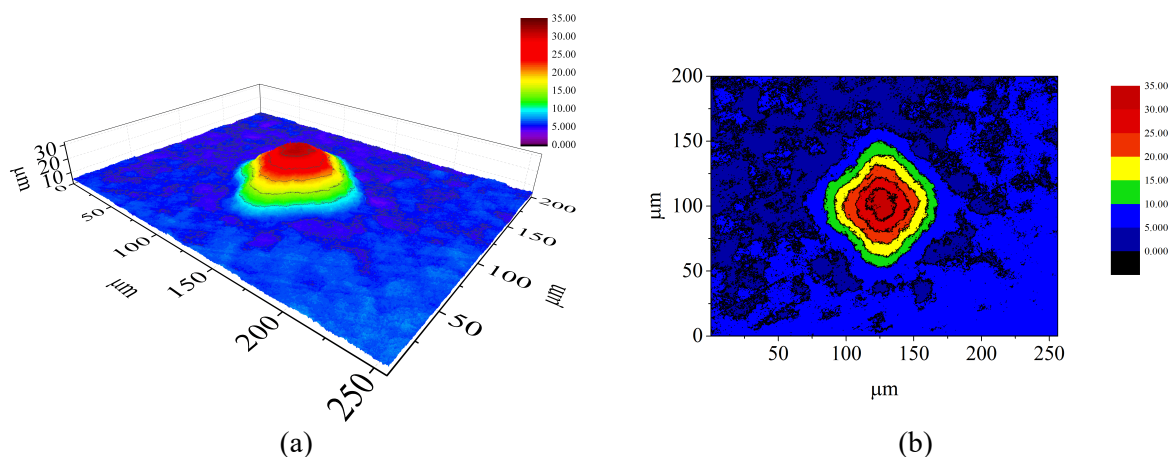


Figure 4-23. (a) 3D model reconstruction of square pyramid and (b) its projection

According to the projection, three zones can be identified: the top, the slope and the bottom. Two cross sections are made at the position A-A (bisector line of the square) and at the position B-B (diagonal of the square) to measure the slope angles. In Figure 4-24(a), the blue phase represents the bottom of the square pyramid, the green phase represents the slope and the red one represents the top. The surface areas at the bottom S_1 and at the top S_1 , the height h , and the angles of the slopes α and β were measured. The cross sections have a profile of symmetrical trapezoid, and the top of the pyramid is flat and smooth (Figures 4-24(b) and (c)).

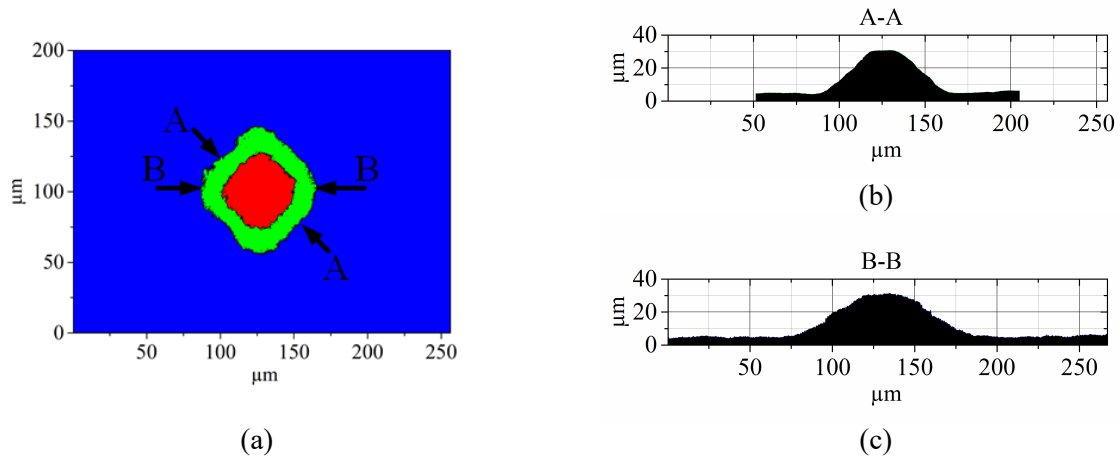


Figure 4-24. (a) Cross sections of the 3D model of the single square pyramid, (b) and (c), cross-sections at position A-A and B-B

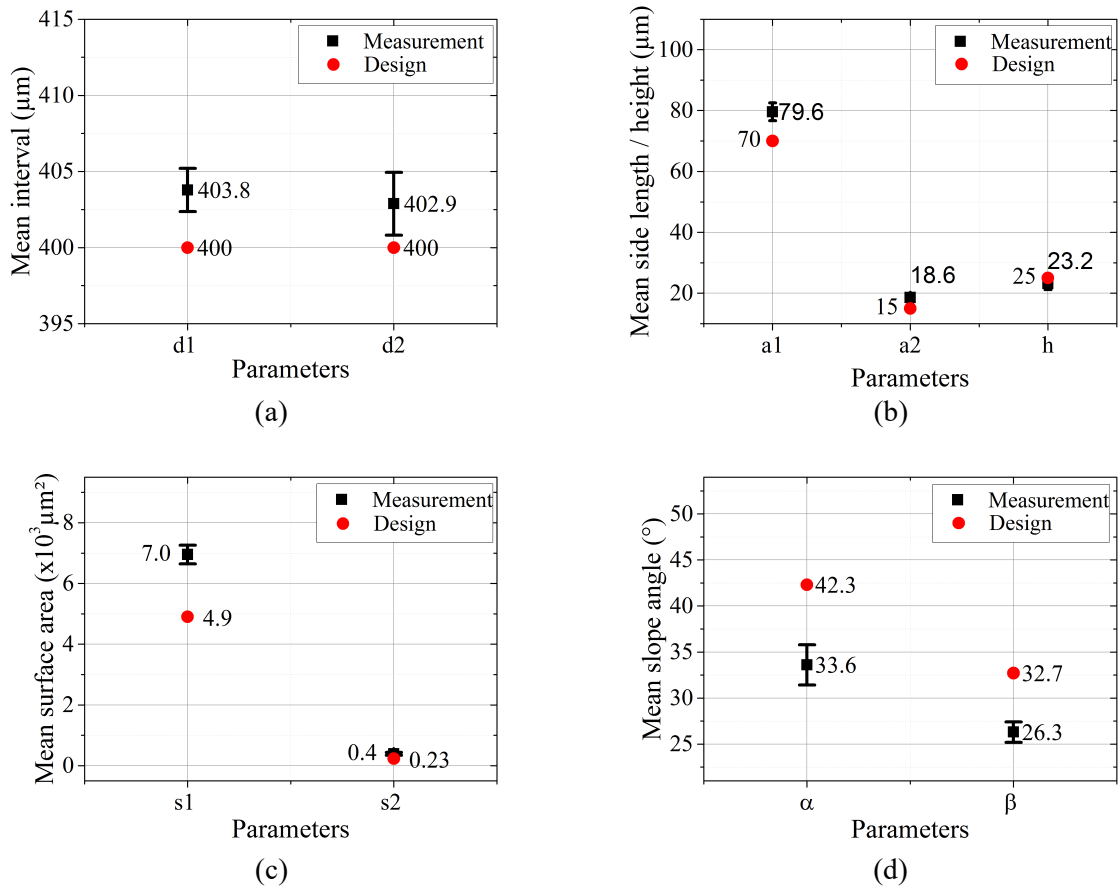


Figure 4-25. Comparison of the geometrical properties between the design and the measurements: (a) interval between the adjacent grains, (b) side lengths and height, (c) surface area and (d) slope angles

Five geometrical property measurements have been carried out (Table 4-14). Figure 4-25 shows the comparison of the geometric properties between the design and the measurements. The intervals d_1 and d_2 between the adjacent pyramids along the X- and Y- axis are 403.8 μm and 402.9 μm, which have a slight deviation about 1% from the design. The side lengths a_1 and a_2 at the bottom and at the top are 79.6 μm and 18.6 μm. The height h is 23.2 μm. Compared with the designed structural geometry

of single square pyramids, a deviation was found from 15% to 25%. Therefore, the resulting surface areas S_1 at the bottom and S_2 at the top, as well as the slope angles α and β at the cross sections A-A and B-B are also deviated from the design.

Table 4-14. Summary of geometrical property measurements of the produced square pyramids

N°	d_1 (μm)	d_2 (μm)	a_1 (μm)	a_2 (μm)	S_1 (μm^2)	S_2 (μm^2)	h (μm)	α ($^\circ$)	β ($^\circ$)
1	402.4	403.6	76.4	17.5	6702.3	368.2	24.1	31.2	26.9
2	404.9	402.3	77.0	19.5	6787.0	419.1	24.7	32.9	27.2
3	405.5	400.5	83.4	19.1	7353.1	432.2	23.0	35.9	26.7
4	402.4	402.0	80.0	20.0	6700.7	403.3	24.1	35.8	26.3
5	403.7	406.0	81.2	16.7	7214.1	313.8	19.9	32.0	24.4
Average	403.8	402.9	79.6	18.6	6951.4	387.3	23.2	33.6	26.3

Table 4-15. Geometrical property comparison of the produced pyramids

Grain amount	Pyramid shape	Sample surface area ($\times 10^7 \mu\text{m}^2$)	Single grain surface area (μm^2)	Total grain surface area ($\times 10^6 \mu\text{m}^2$)	Phase ratio
343	Hexagon	6	9.1×10^3	3.1	5.2%
329	Square	6	7.0×10^3	2.3	3.8%

Table 4-15 summarizes the important geometrical properties of the produced hexagonal and square pyramids. In total 343 hexagonal pyramids were produced on the WC-CoNi hardmetal sample surface within the area of $6 \times 10^7 \mu\text{m}^2$. The total grains have the surface area of $3.1 \times 10^6 \mu\text{m}^2$, about 5.2% of the sample surface area. 329 square pyramids in total have been produced on the surface of $6 \times 10^7 \mu\text{m}^2$, and the total grains account for 3.8% of the surface area, i.e. $2.3 \times 10^6 \mu\text{m}^2$. The obtained phase ratios of the both pyramids are deviated from 1% to 3% compared with the design ones (Figure 4-26).

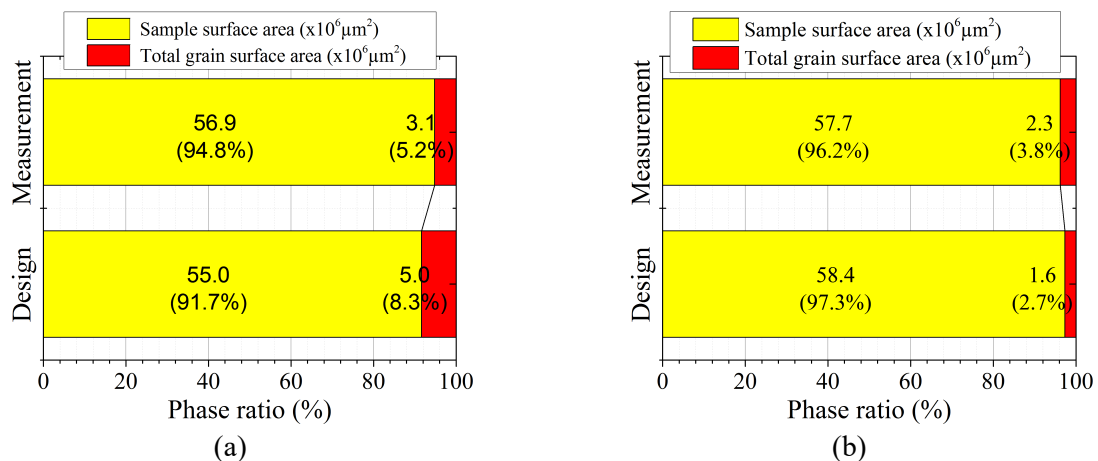


Figure 4-26. Phase ratio comparison between the design and measurement: (a) hexagonal pyramids and (b) square pyramids

The geometrical property characterization of the produced hexagonal and square pyramids on WC-CoNi hardmetal surfaces indicates that high geometrical precision

has been achieved using Laser machining. Hence, LST is an appropriate method to fabricate and produce the designed geometrical properties on the hardmetal surfaces, despite of some slight deviations of the basic pyramid parameters (a_1 , a_2 , h). These deviations are some microns (about 15% to 25%) between the designed and the measured values. There are three main factors which can cause the geometrical deviations. Firstly, the material is shaped by the switch control of the laser beam during the machining process, as the laser beam moves at a constant speed in certain direction. When the laser beam is switched on, the material is ablated. In contrary, no ablation occurs. In order to produce the pyramids, a switch control is necessary according to the geometrical properties. However, a time delay of the switch from the control system is not negligible, and this delay can be the main cause of the geometrical deviation. Secondly, the machining parameters of the laser beams should be correctly configured according to material properties, for example, the machining speed and the correction of spot size etc. Lastly, some errors can also be induced during the measurement operation, for example, the selection of the measurement points of the side length under the microscope etc. Nevertheless, these deviations are still acceptable with regard to machining tolerance, and they can be optimized by the experience accumulations in the future. Within the context that the pyramids are considered similar as CBN grains of the honing stones, the successful production of two different pyramid geometries enables a new approach to reproduce the honing stone surfaces on hardmetal surfaces. This achievement expands definitely the utilization of hardmetal.

5 Tool testing

In this study, the surfaces of hardmetal tools have been modified using LST. Variant defined structures were produced on the tool surfaces, aiming to fulfil two major goals according to their shape features. The concave structures can be applied in a tribological system to reduce friction, and the convex structures can be used to remove the workpiece materials, potentially as an alternative of honing stone. In chapter 4, the production of tool surface patterns and surface integrity assessment were described. Concave structures, such as line-like patterns (interference structure), dimples, grooves, were produced for tribological application. Convex structures (hexagonal and square pyramids) were produced for abrasive application. Accordingly, several approaches are applied to evaluate the different surface patterns regarding frictional, abrasive and wear performances (Table 5-1). In some cases, polished surface and EDM machined rough surfaces are also involved as reference cases. For the tribological application, friction tests are carried out on the in-house workbench, which is an in-situ test similar to the external honing processes. A Nano-tribometer is also employed to evaluate the frictional behavior of the produced patterns in the micrometer scale. Wear resistance of the produced patterns is measured using Calowear test. All the three mentioned evaluation approaches are applied on the line-like patterns. Dimples are tested by the in-situ friction testing on the workbench. Polished surfaces have been tested using the three approaches as reference conditions. Rough surfaces are tested on the workbench as reference condition. For the abrasive application, hexagonal pyramids are tested on the workbench, and the honing stone B151 is also tested as reference. The cutting forces in the tests are recorded and compared. Surface roughness of the workpieces after machining processes is measured. Following the tests, surface integrity of the patterns are assessed using LSM and SEM/FIB.

Table 5-1. Tool testing of different surface patterns for determined applications

Pattern application	Pattern	Tool testing			
		Friction test (Workbench)	Friction test (Nano-tribometer)	Wear test (Calowear)	Abrasive machining test (Workbench)
Friction reduction	Line-like	√	√	√	-
	Dimples	√	-	-	-
	Polished	√	√	√	-
	Rough	√	-	-	-
Material removal	Hexagonal pyramids	-	-	-	√
	B151	-	-	-	√

5.1 Tool testing for tribological application

5.1.1 Friction tests on the workbench

According to Table 2-5 (on Page 18), only the surface patterns and normal forces are set as variables. The test tools are made of The WC-CoNi hardmetal (Table 2-2 on Page 6) with the dimension $20 \times 3 \times 4.95 \text{ mm}^3$. The test counterpart (workpiece) has a rotation speed of 500 r/min (i.e. 40 m/min), and an oscillation speed of 1000 mm/min. The velocity is close to the industrial honing processes (Table 5-2).

Table 5-2. Machining parameters set for the workbench

Rotation speed (rpm)	Oscillation speed (mm/min)	Oscillation number	Feed (μm)	Lubrication viscosity (mm^2/s)
500	1000	10	2	5 or 5.6

For each test, the tool has $2 \mu\text{m}$ feed to the rotating test counterpart (workpiece), which oscillates 10 times in every $1 \mu\text{m}$ feed. Normal loads F_n are chosen and applied according to experimental requirement. Two types of lubricants Kadiol 50 and Kadiol 90 (produced by Kadia GmbH) are used for the experiments (Table 5-3). The working surfaces of the test counterparts have been pre-machined to meet the required roughness (Table 5-4).

Table 5-3. Lubricants used in the experiments

Designation	Application in this study	Type	Viscosity ν at 40°C (mm^2/s)	Utilization
Kadiol 50	Experiment A	synthetic oil	5	for high-alloy and hardened steels
Kadiol 90	Experiment B	synthetic oil	5.6	for high-alloy and hardened steels

Table 5-4. Roughness requirement of pre-machined workpiece

Ra (μm)	Rz (μm)	Rmax (μm)
<0.1	<1.5	<2

Different normal forces and surface patterns are determined for the following two experiments.

Experiment A

Two different surface patterns with deterministic geometries on the micrometer scale are achieved by two distinct LSP methods: line-like patterns by Laser-Interference Metallurgy (LIMET) with ns-laser and dimples by ps-laser. A polished surface has also been tested under the same conditions.

- WC-CoNi part with line-like patterns produced by LIMET;
- WC-CoNi part with dimples produced by ps-laser;

- WC-CoNi part with polished surface.

The dimensions of line-like patterns as well as the dimples are mentioned in Figure 4-5 on Page 51 and in Figure 4-7 on Page 53: the line-like patterns possess a periodicity of 11.8 μm and a height of 0.6 μm , and the dimples possess a diameter of 52.3 μm , a depth of 3.8 μm and an interval between adjacent dimples of 505.5 μm . The COF is measured to evaluate the impact of the surface patterns. Line-like patterns and dimples are tested under the conditions mentioned in Table 5-5 to observe the tribological performances. Normal loads are applied from 15 N to 70 N, corresponding to pressures from 0.25 MPa to 1.2 MPa on the contact surfaces. Kadiol 50 is used as lubricant. Each test has been 10 times repeated.

The tests on the three surface structures have been then conducted with four different normal loads, which were set to 15/30/50/70 N. The obtained COFs are listed in Table 5-5. The surface with the dimples has the smallest COF of 0.13, followed by the polished surface (COF: 0.16) and then the surface with line-like patterns (COF: 0.19). When the normal loads increase, COFs increase as well. The dimples can maintain small friction compared with the other two surfaces.

Table 5-5. COFs obtained in each friction test on the workbench

F_n (N)*	COF		
	Polished	Dimples	Line-like
15	0.13	0.08	0.16
30	0.16	0.12	0.19
50	-	0.14	0.20
70	0.19	0.17	0.21
Average	0.16	0.13	0.19

* These are set values

Figure 5-1(a) shows the COFs for the two surface patterns and a polished reference under lubricated conditions with different normal loads from 15 N to 70 N. The tribological performance of the two patterns varies from each other. Higher friction was obtained with line-like patterns. As the contact pressure increases, the COFs of both patterns also increase. However, the dimples have an increase with greater magnitude than the line-like patterns. Compared with the polished surface, line-like patterns increase the friction but the dimples remarkably diminish the friction.

Regarding the line-like patterns, the micro-asperities increase the surface roughness, which is harmful for the construction of full fluid lubrication [71]. The asperities will increase the amount of solid-solid contact. This explains the friction augmentation compared with the polished surface. In these experiments, the line-like patterns are oriented parallel to the rotation direction, which is favorable for the formation of the lubricant channels (Figure 5-1(b)). The lubricant channels connect the high pressure regions and low pressure regions, and conduct the lubricant to surrounding areas [72,73]. In addition, the discontinuities of the line-like patterns facilitate the lubricant flow from the channels to the contact area. The lubricant channel effects are more

significant under higher contact pressures [74], and this could explain why the friction increase by the line-like patterns is not as much as the dimples when the load increases.

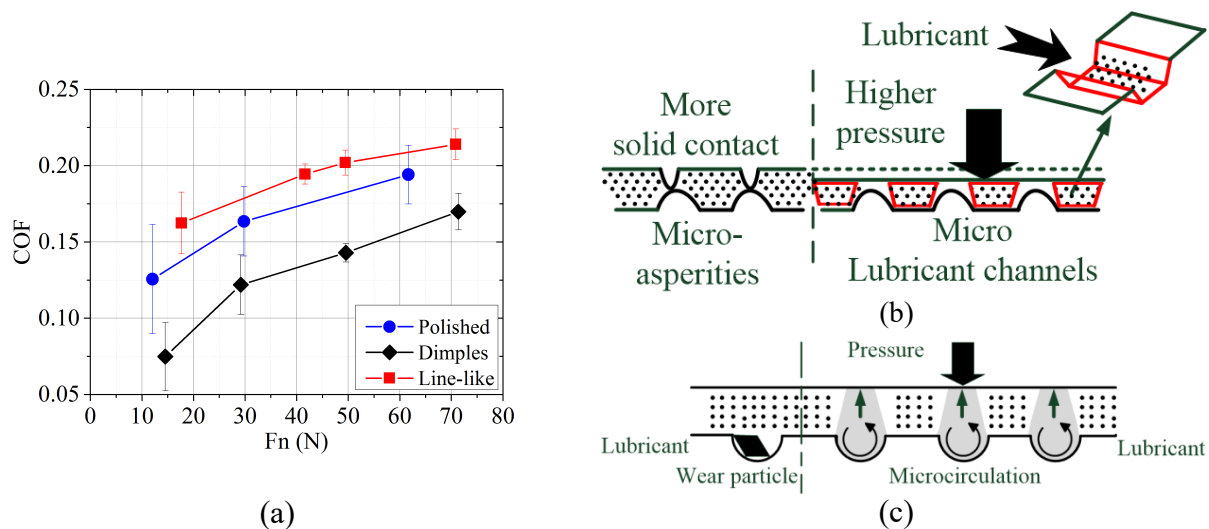


Figure.5-1. (a) Analysis of the COF for line-like patterns and dimples as a function of the normal loads, (b) schematic diagram of the line-like pattern interfaces, (c) schematic diagram of the lubrication microcirculation and the interfacial reaction in the dimples

Regarding the dimples, two observations can be made: lower friction is attained compared with other patterns, and the friction reduction at high load is not as remarkable as that at low load. The observations can be explained by two aspects. On the one hand, the dimples act as the reservoirs in the tribological systems (Figure 5-1(c)). The reservoirs can trap the wear particles to prevent from solid-solid contact [75]. On the other hand, the reservoirs form the microcirculation of the lubricants which generates local pressure. The produced pressure is in favor to increase the thickness of the lubrication film and improve the load-carrying capacity [108,109]. Consequently, hydrodynamic effects are enhanced to ameliorate the frictional conditions. However, the hydrodynamic effects are less pronounced at high load [71,110], owing to the fact that full lubrication is more difficult to establish due to the absence of the lubricant channels which help redistribute the lubricant [72]. Hence the friction of the dimples has an obvious rise when the load increases.

Experiment B

The following specimens with different surface patterns were tested on the work-bench to compare their tribological performances:

- WC-CoNi part with rough surface produced by EDM;
- WC-CoNi part with polished surface;
- WC-CoNi part with laser-patterned surface (dimples produced by fs-laser).

As a common hardmetal machining method, it is interesting to compare the EDM machined surfaces in this study. The quality of the EDM machined surface can be strongly influenced by the thermal reactions. The mechanical strength of the cement-

ed carbides may also be affected by EDM. Characteristics of the eroded surface after the W-EDM process can be observed in Figure 2-3 on Page 8, which reveals material melting, re-deposition, pores, and contamination etc. after the EDM processing. The eroded surface has the roughness less than 10 μm , and is often covered with a layer containing oxides, contaminations, etc. The layer thickness ranges from a few micrometers up to ten micrometers [12,16].

The dimples were created using fs-laser with an auto stage on the hardmetal surface. They possess the diameter of approximately 150 μm and a depth of roughly 3.5 μm (Figure 4-9 on Page 56). Adjacent dimples are approximately 500 μm in both X- and Y- axis direction. The testing program in Table 5-2 is used. Three different normal loads, namely 15, 30 and 50 N, were applied on the contact surfaces. Kadiol 90 was applied with a pressure of 0.07 bar. Each experiment was repeated ten times under the same conditions. The obtained COFs are listed in Table 5-6. The surface with dimples has the smallest average COF of 0.11, and then the polished surface acquires the COF of 0.16, followed by the rough surface with the COF of 0.23. When the normal force is 15 N, all the three surfaces reach the highest friction values.

Table 5-6. Values of COFs obtained in each friction test on the workbench

Fn (N)*	COF		
	Rough	Polished	Dimples
15	0.31	0.22	0.17
30	0.20	0.11	0.07
50	0.18	0.15	0.09
Average	0.23	0.16	0.11

* These are set values

Figure 5-2 shows the COFs of all tested specimens as a function of normal forces. It can be observed that the COFs of the polished, EDM-rough and dimpled surfaces decreases when the normal load increases. However, the descend trend of COFs seems to change for the polished and dimpled surfaces when the normal load passes a certain limit within the observed range. It can be also observed that the surface patterns have significant influence on the COFs. The patterned surfaces show the lowest COF, followed by the polished and the rough ones, since the dimples can trap wear particles thus reducing the COF [75], and the dimples act also as lubricant reservoirs thus providing additional lubricant [109,111]. Figures 5-2(b), (c) and (d) are the schematic illustrations of the interfacial reactions of the three types of surface structures in the tribological systems. For the rough surface, the relative motion between the test samples and test counterparts are limited and hindered by the asperities out of the surfaces or by the wear debris produced by the collisions of the asperities. For the dimples, the wear debris can be seized and stoked in the dimples, which is beneficial for lower friction. In addition, the dimples act also as lubricant reservoirs thus providing additional lubricant and pressure, which is beneficial for the stabilization of the lubrication film.

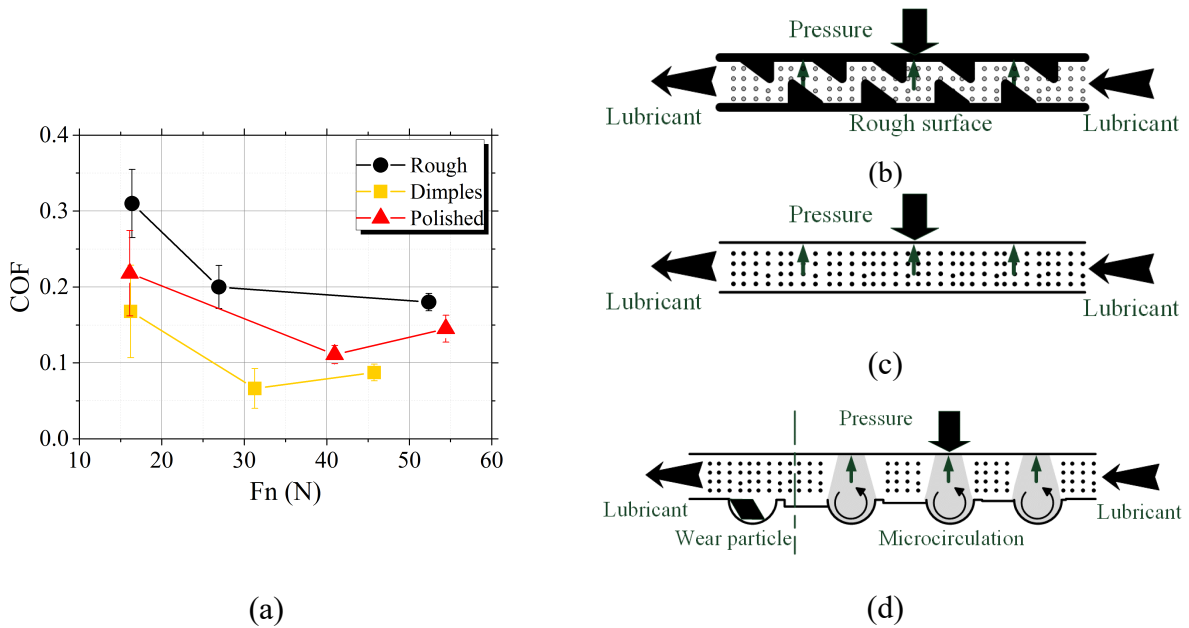


Figure 5-2. (a) COFs as a function of normal loads for all tested specimens, interfacial reactions of (a) rough surface, (b) polished surface, (c) surface with dimples

Noticeable observations

In Experiment A, the friction tests indicate that the dimples can efficiently reduce friction and expand the hydrodynamic effects. Higher friction is obtained by line-like patterns compared with polished surfaces, but only slight friction augmentation has been observed by line-like patterns when the load increases. In Experiment B, the friction tests show that dimples reduced the friction in the tribological system compared with polished and rough surfaces. The dimples can form micro-lubricant reservoirs and supply lubricants as well as store wear particles. Furthermore, the additional lubricant supply might increase film thickness thus contributing also to a reduced friction.

In consideration of both experiments, the surface with dimples proved to be favorable to obtain less friction in the tribological systems, and the line-like patterns are favorable to stabilize the friction as the normal force increases. But the obtained friction levels were different in these two experiments when the normal load was at low level (about 15 N): the friction had the lowest level in Experiment A but highest in Experiment B. This observation can be explained by the difference of the used lubricants. In Experiment A, there are some additives in the used lubricant Kadio 50, which can help rapidly stabilize the lubricant film at the very small normal load and to reach low friction.

5.1.2 Friction tests on Nano-tribometer

Friction tests using Nano-tribometer have been conducted on two types of surfaces (polished surfaces and line-like patterns, Table 5-1). The dimension of test samples and the dimension of the line-like patterns are shown in Figure 2-2(b) on Page 7 and Figure 4-5 on Page 51. Each type of the surface patterns has been tested with and without lubricants for three repetitions under identical conditions shown in Table 5-7.

Identical standard test counterparts are used for each test. The test counterparts are made of Steel 100Cr6 and have the diameter of 3 mm with polished surface. The sample is fixed on the test table and moves reciprocally at a maximal linear speed of 1 mm/s with an amplitude 0.6 mm. 1000 cycle is set to test the frictions with and without lubricants. The lubricant Kadiol 50 is used, which has a kinematic viscosity ν of 5.6 mm²/s at 40 °C. The normal load applied on test sample is 1mN.

Table 5-7. Nano-tribometer configuration

Acquisition rate (Hz)	Trajectory	½ Amplitude (mm)	Max Lin.Speed (mm/s)	Frequency (Hz)	Cycle	Normal load (mN)
100	Sinus	0.3	1	0.53	1000	1

The signals of the normal force F_n and the tangential force F_t for each test are recorded, and the average values of COFs for the entire testing periods are calculated using Equation (2-2) on Page 21. According to the results in Table 5-8, polished & non-lubricated surfaces (P_NL) obtained the highest COF of 0.24, followed by the patterned & non-lubricated surfaces (L_NL), which have the COF of 0.20. The COFs, which are obtained by polished & lubricated (P_L) as well as by patterned & lubricated surfaces (L_L), are 0.14 and 0.13, respectively. It is obvious that the utilization of lubricants can effectively reduce the friction, and the patterns are also beneficial to reduce friction in the case without lubricants.

Table 5-8: Average COFs of the friction tests on Nano-tribometer

COF	Polished & non-lubricated (P_NL)	Polished & lubricated (P_L)	Patterned & non-lubricated (L_NL)	Patterned & lubricated (L_L)
μ	0.24	0.14	0.20	0.13

Figure 5-3 shows the comparison of the COFs for the two types of surface patterns as a function of slide laps. It is found that the frictional performances are not stable at the beginning and at the end of the experiments, since that the contact between the test samples and test counterparts have experienced unstable stages due to the surface deformation and changes at the two periods. Except for the case of polished & non-lubricated surface (P_NL), COFs of the other three cases experienced decrease at the beginning 200 sliding laps, whereby the COF of the patterned & non-lubricated surface (L_NL) had a remarkable drop at the beginning of the contact installation.

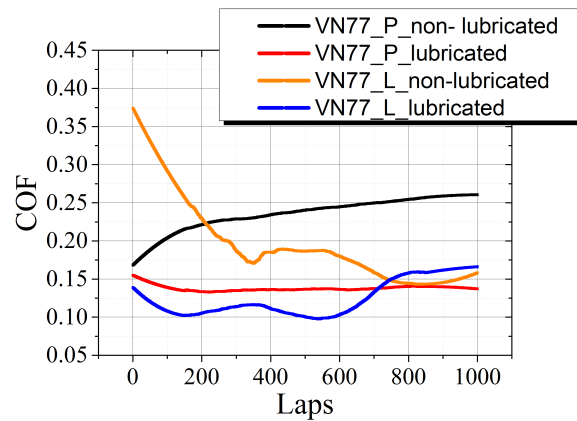


Figure 5-3. Evolutions of COFs for each type of surface patterns as a function of the slide laps

Figures 5-4(a) and (b) show the COF comparison between polished and patterned surfaces in the cases of non-lubricant and with lubricant, respectively. Without lubricants, the frictional performances of the polished and patterned surfaces are quite unstable (Figure 5-4(a)). The friction of the polished surface experienced a remarkable rise along with the slide laps, but the friction of the patterned surface experienced a huge drop at the beginning. This observation can be explained by the changes of surface structural conditions. In the case of polished & non-lubricated surface (P_NL), the materials were compressed and deformed, and the stacked materials hindered the movement of the samples. However, in the case of patterned & non-lubricated surfaces (L_NL), the initial surface structures were relatively rough compared with a polished one, therefore, COF was quite high at the beginning. But the patterns were deformed and even destroyed along with the sliding laps. After the unstable stage, COF of patterned surface was much lower than the one of the polished surface since the tiny debris particles could work as tiny lubricant between the two surfaces, which helped reduce the friction. With lubricants (Figure 5-4(b)), the frictional performances of both two surface patterns were more stable, except that the COF of patterned surfaces has increased between the 600 cycles and 800 sliding laps. It is supposed that the patterns began to destroy at the 600 cycles, and the contact between the two surfaces was becoming less stable till the 800 cycles. Then the friction regained stability after 800 cycles, since the patterns were completely demolished and a new stable contact was re-established. The COFs of polished and patterned surfaces were relatively constant during the whole test except a slight decrease at the very beginning. This observation can be explained by the fact that the lubrication film stabilized the tribological system.

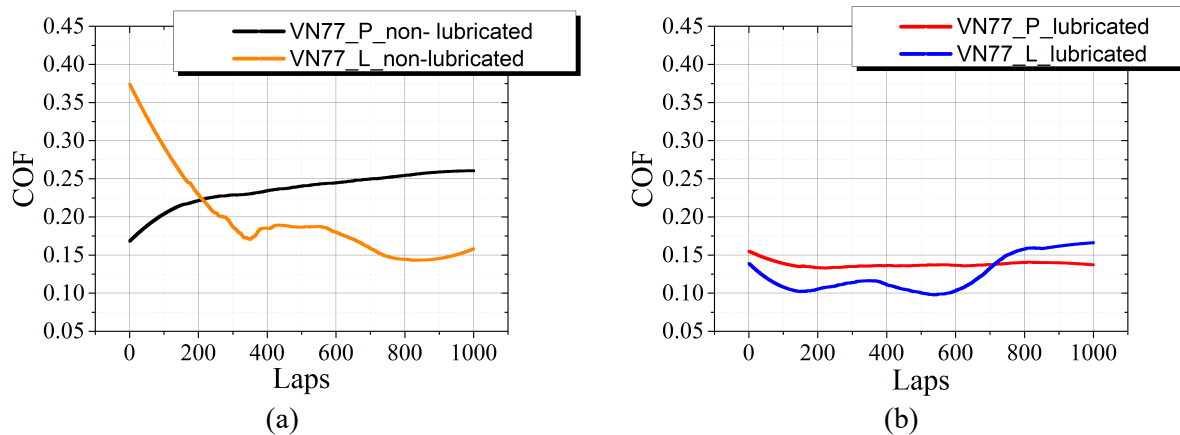


Figure 5-4. COF evolution as a function of slide laps: (a) comparison between polished and patterned surfaces in the non-lubricated case, (b) comparison between polished and patterned surfaces in the lubricated case

Figures 5-5(a) and (b) show the COF comparison on lubricant as a function of slide laps for the two surface patterns. It is found that the use of lubricants could effectively reduce the friction for both polished and patterned surface. A more stable contact between the test samples and the test counterparts could be established, especially in the case of the patterned surfaces before the patterns began to destroy at the 600 cycles.

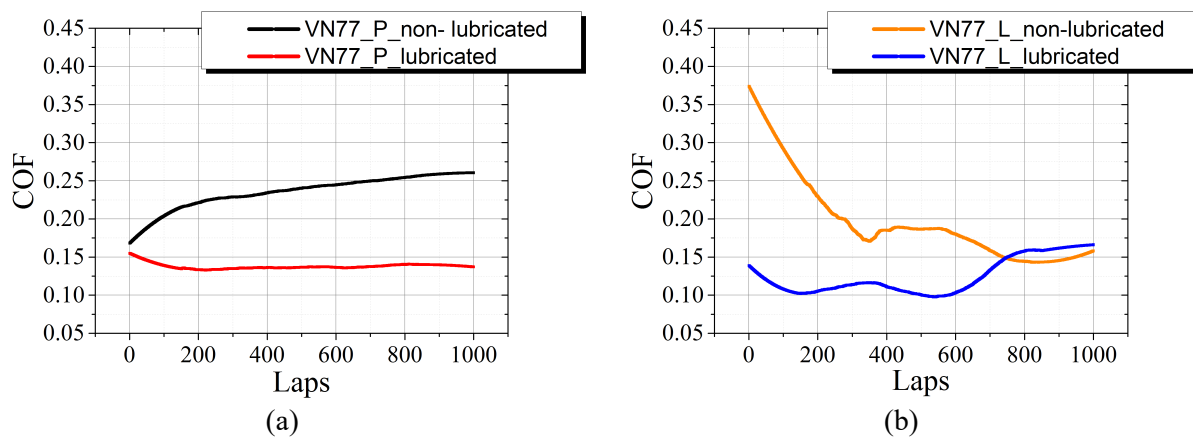


Figure 5-5. COF evolution as a function of slide laps: (a) comparison on lubricants for polished surfaces, (b) comparison on lubricants for patterned surfaces

It is found that the line-like patterns can reduce the friction compared with the polished surfaces in both non-lubricated and lubricated cases, but the patterned surfaces are not as stable as the polished ones in both cases, especially at the beginning (<200 cycles) and at the end (> 800 cycles) of the tests.

The use of the lubricants can improve the frictional performances for both surface patterns and help achieve a more stable contact between the test samples and the test counterparts. It can effectively reduce the friction of the patterned surface at the beginning of the tests (<200 cycles) and extend the life of the patterns, since the lubricant can help rapidly establish the lubricant film.

5.1.3 Wear tests on Calowear set-up

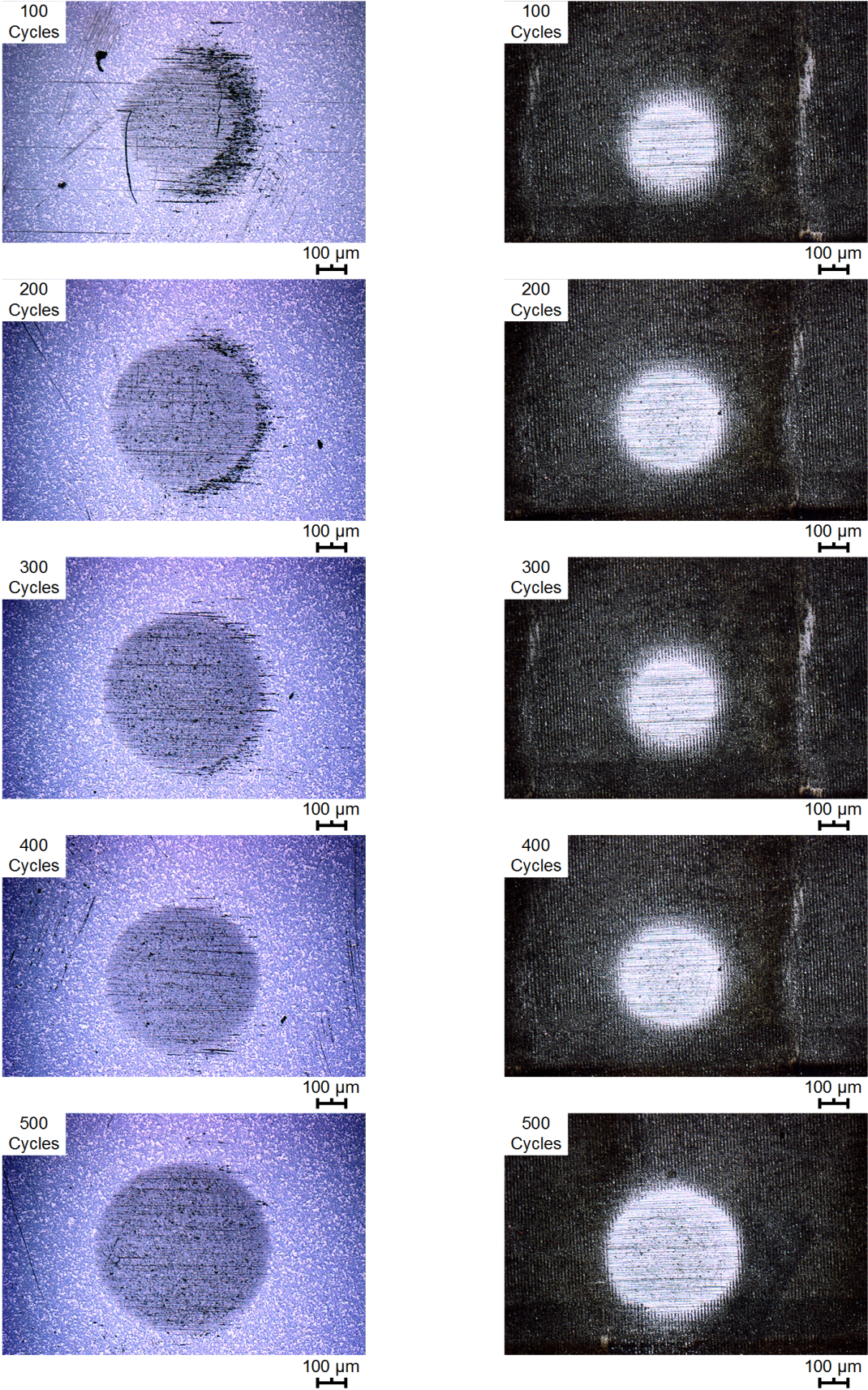
Calowear tests without lubricants

Two different patterns (line-like patterns and polished surface) have been tested on Calowear set-up. The geometrical properties of the line-like patterns are described in Figure 4-5 on Page 51. All the samples in the two groups were tested under the conditions given in Table 5-9. Four important parameters are needed to obtain the wear rate K (Table 2-7 on Page 22). The standard testing counterpart is a ball made of steel with a diameter d of 25.4 mm, which rotates at a constant speed at five different positions with corresponding sliding cycles on the polished and patterned surfaces. Normal force F_n applied on the test sample was set 0.75 N. Diameters b of the sizes of the wear craters were measured and recorded at the cycles of 100/200/300/400/500, respectively. The corresponding sliding distances L were calculated according to the rotation cycles and the ball diameter d . The tests were carried out without lubricants. Knowing all the four parameters, the wear rate K can be then calculated using Equation (2-3) on Page 21.

Table 5-9. Calowear test instrument configuration

Testing counterpart diameter d (mm)	F_n (N)	Measurements at the cycle of	Lubricant
25.4	0.75	100/200/300/400/500	-

Figures 5-6(a) and (b) show the diameter changes of the wear craters on the polished and patterned surfaces as a function of the sliding cycles. The contact areas have circular profiles and the edges of the contact areas can be clearly identified. In the middle of the circle, previous structures are not discernable any more due to the material removals. For both surface conditions, the wear craters expand with the sliding distance and the diameters of the wear craters are approximately proportional to the sliding cycles. At the same sliding cycles, the patterned surfaces have smaller craters than the polished ones.



(a)

(b)

Figure 5-6. Wear crater evolution as a function of sliding cycles on the surfaces with different patterns: (a) polished surfaces, (b) line-like patterns

The diameters of the wear craters were measured using LSM. The diameter values and the calculated corresponding wear rates K are shown in Table 5-10 as well as in Figure 5-7. It is found that the diameter difference between the two surfaces remains constant of about 100 μm to 150 μm at each measurement cycle. The wear rates of both surface conditions have a slight increase as a function of the sliding cycles. The mean values of the wear rates K of polished surface and the patterned are $1.85 \times 10^{-2} \mu\text{m}^2/\text{N}$ and $0.73 \times 10^{-2} \mu\text{m}^2/\text{N}$ respectively. The results prove that the wear rate of the patterned surface is two times lower than that of the polished surface, and the line-like patterned can obviously reduce the wear rate.

Table 5-10. Measurement results on the polished and patterned surfaces

Cycles	Polished surface		Line-like patterns	
	Crater diameter b (μm)	Wear rate K ($\times 10^{-2} \mu\text{m}^2/\text{N}$)	Crater diameter b (μm)	Wear rate K ($\times 10^{-2} \mu\text{m}^2/\text{N}$)
100	400.7	1.73	290.0	0.46
200	508.5	2.19	370.0	0.59
300	554.5	2.06	456.4	0.92
400	547.2	1.43	488.5	0.92
500	621.4	1.85	497.0	0.77
Average	526.5	1.85	420.4	0.73

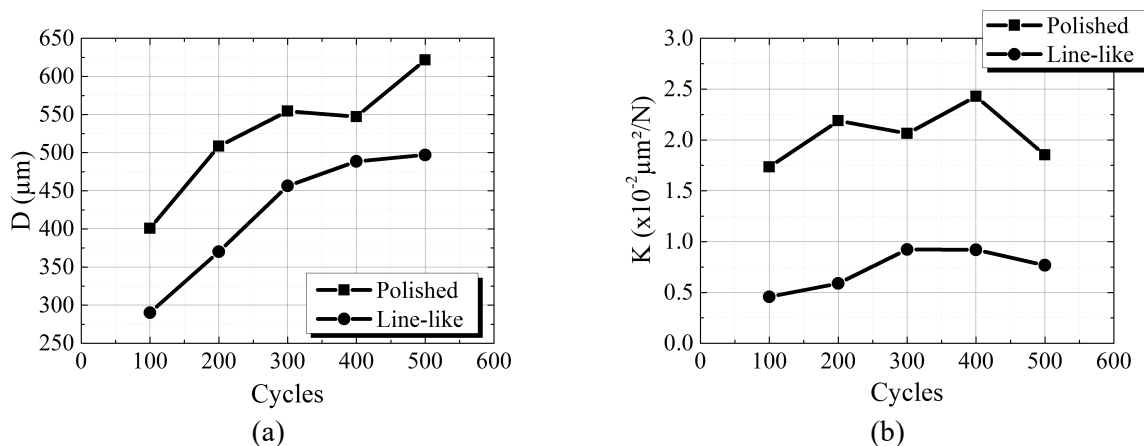


Figure 5-7. Calowear test results of polished surface and line-like patterns: (a) diameter (D) vs. sliding cycles, (b) wear rate (K) vs. sliding cycles

With the line-like patterns, the contact surface area between the test sample and the test counterpart is reduced: the diameter of the wear crater produced on the patterned surface is about 100-150 μm less than that produced on the polished surface at the same sliding distance. The wear rate is reduced by a half by the line-like patterns.

Calowear tests with lubricants

The mechanical contact responses to the two types of surface conditions are also subject to be investigated with lubricants. The lubricant Kadiol 50 with a kinematic

viscosity ν of 5 mm²/s at 40 °C was used to conduct the experiments. In the experiments (Table 5-11), the counterpart (steel ball with a diameter d of 25.4 mm) was placed on the surfaces of testing samples, which were fixed on the sample support table. The table has been adjusted in order to obtain the desired normal force F_n of 0.44 N. The counterpart rotated at a constant speed and produced craters on the sample surfaces. The crater diameters, b , were noted at the cycles of 100/200/300/400/500, respectively. In order to offer reference conditions, the experiments have also been conducted without lubricants.

Table 5-11. Calowear test instrument configuration

Testing counterpart diameter d (mm)	F_n (N)	Measurements at the cycle of	Lubricant
25.4	0.44	100/200/300/400/500	Kadiol 50

The crater sizes were measured using LSM. Their diameters, b , were recorded in Table 5-12, and the corresponding wear rates K were obtained according to Equation (2-3) on Page 21. It is found that the average wear rates K of the polished surfaces are $4.01 \times 10^{-2} \mu\text{m}^2/\text{N}$ and $6.21 \times 10^{-2} \mu\text{m}^2/\text{N}$ for the non-lubricated and lubricated cases, respectively. For the patterned surfaces, the wear rates K are $1.22 \times 10^{-2} \mu\text{m}^2/\text{N}$ and $5.84 \times 10^{-2} \mu\text{m}^2/\text{N}$ for the non-lubricated and lubricated cases, respectively.

Table 5-12. Measurement results on the polished and patterned surfaces

Cycles	Polished surface				Line-like patterns			
	Crater diameter b (μm)		Wear rate K ($\times 10^{-2} \mu\text{m}^2/\text{N}$)		Crater diameter b (μm)		Wear rate K ($\times 10^{-2} \mu\text{m}^2/\text{N}$)	
	Non-Lubri-cated	Lubri-cated	Non-Lubri-cated	Lubri-cated	Non-Lubri-cated	Lubri-cated	Non-Lubri-cated	Lubri-cated
100	312.6	462.7	1.05	5.05	364.9	415.0	1.95	3.27
200	550.0	590.0	5.04	6.67	427.2	618.8	1.83	8.07
300	570.4	629.0	3.88	5.74	500.8	607.5	2.31	5.00
400	644.4	697.8	4.75	6.53	547.0	657.1	2.46	5.13
500	701.2	752.9	5.32	7.07	637.7	769.4	3.64	7.72
Average	555.7	626.5	4.01	6.21	495.5	613.6	1.22	5.84

Figure 5-8 shows the crater diameters and the wear rates as a function of slide cycles in the four different cases (polished and non-lubricated, polished and lubricated, patterned and non-lubricated, patterned and lubricated). It is obvious that the crater sizes are increasing along with the cycles (sliding distance) in all the cases.

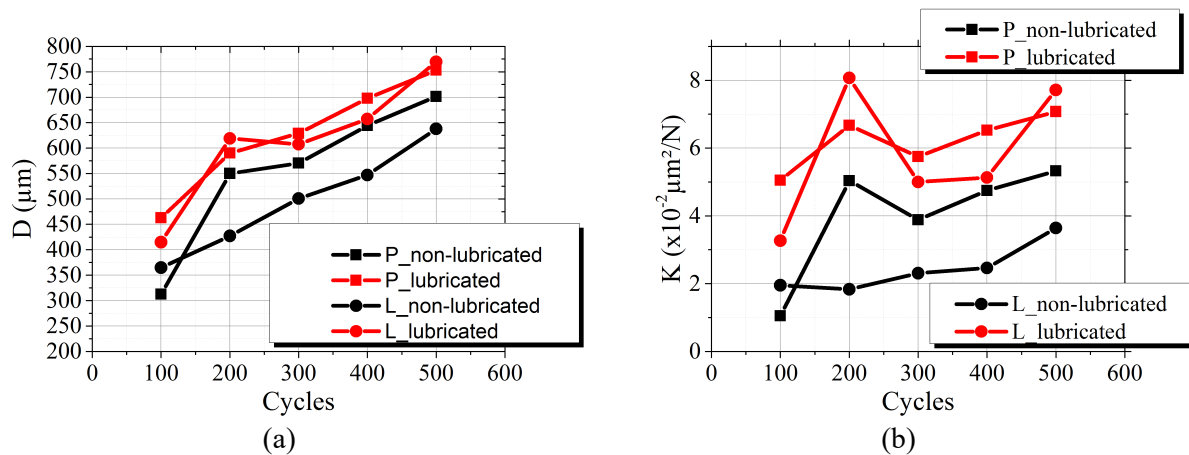


Figure 5-8. Calowear test results of polished and patterned surfaces with/without lubricant: (a) diameter (d) vs. sliding cycles, (b) wear rate (K) vs. sliding cycles

Figure 5-8(a) shows the diameters of the wear craters as a function of the sliding cycles. Concerning the influences of the patterns on the crater size, two observations can be made:

- craters produced on the patterned surfaces are smaller than those produced on the polished surfaces under both non-lubricated and lubricated conditions;
- in consideration of the absolute values of the crater diameters, the patterns can reduce the crater size compared with the polished surfaces, especially in the non-lubricated case.

Concerning the influences of the lubricant on the crater size, the lubricated surfaces can obtain larger craters than the non-lubricated ones but:

- in the case of polished surfaces, the crater under lubrication is about $70 \mu\text{m}$ larger than that without lubricant;
- in the case of patterned surfaces, the crater under lubrication is about $120 \mu\text{m}$ larger than that without lubricant.

The wear rate exhibits an increasing tendency along with the cycles (sliding distance), except some singular points in all the four cases (Figure 5-8(b)), but:

- less wear is achieved on the patterned surfaces than on the polished ones under the both lubricated and non-lubricated conditions;
- however, the reduction of the wear rate on the patterned surface becomes less remarkable with lubricants;
- the wear rate is more pronounced in the lubricated case for both polished and patterned surfaces than for those in the non-lubricated case.

Figure 5-9 shows the surface integrity assessment after the Calowear tests. The SEM images were taken at the cycle of 300 for each test. Figure 5-9(a) and (b) exhibit the imprints on the polished surfaces tested with lubricant and without lubricant, respectively. The crater imprints can be clearly observed and it is proved that the crater produced with lubricant is larger than that produced without lubricant. The

zoomed images show more details about the occurrences on the contact area. Some scratches are found on the both non-lubricated and lubricated surfaces, but they are more pronounced on the lubricated surfaces. Both the WC grains and binder suffered from wear: the binder was mainly removed by abrasion, and the WC grains were removed not only by abrasion but also by the cleavage due to its high hardness and the extrusion. Therefore, some tiny grains were produced and stocked around big grains. This tiny debris can erupt in the tests.

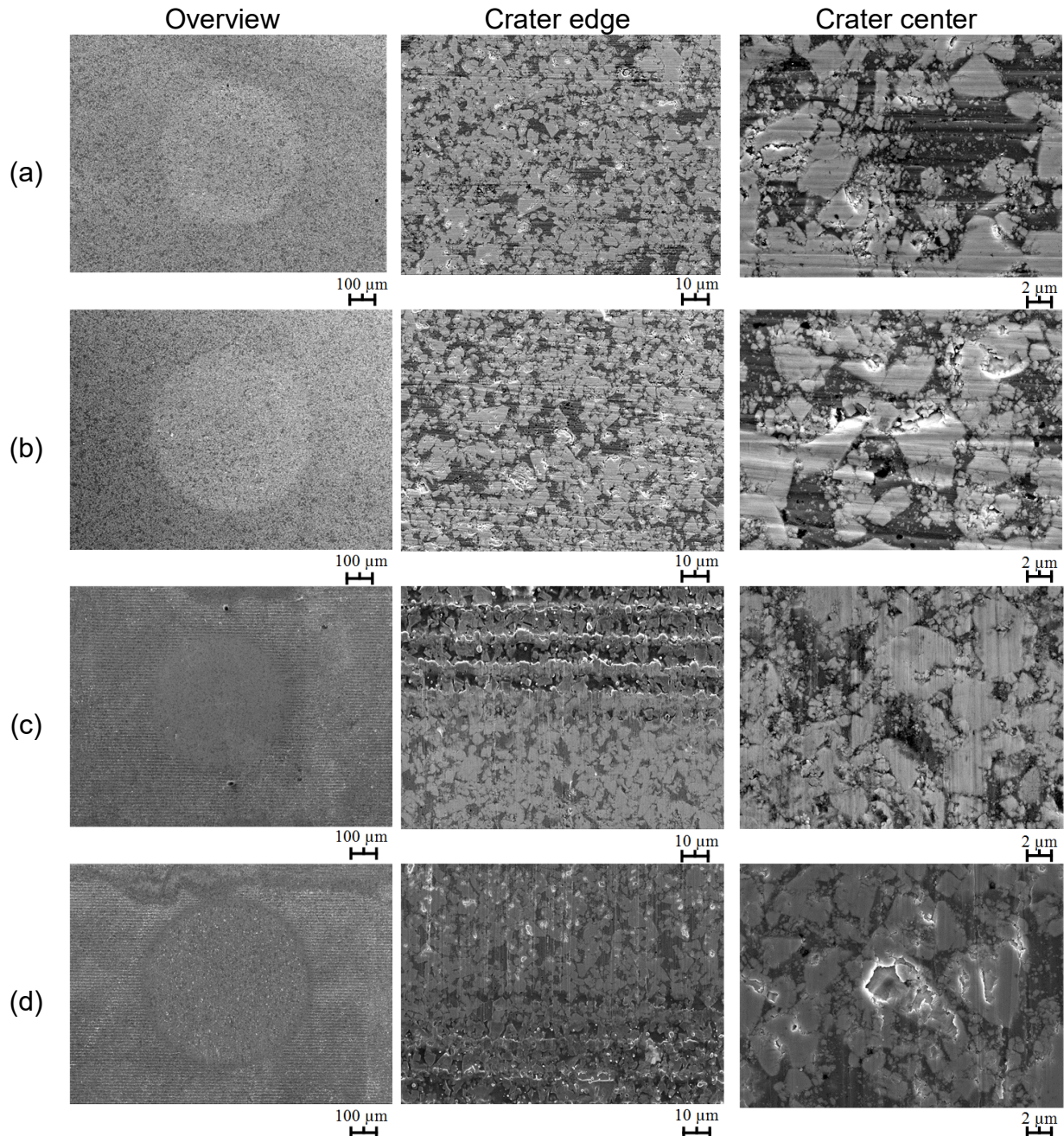


Figure 5-9. SEM investigation of wear craters produced on different surfaces and under different conditions: (a) polished and non-lubricated, (b) polished and lubricated, (c) patterned and non-lubricated, (d) patterned and lubricated

Figures 5-9(c) and (d) demonstrate the patterned surfaces after the Calowear tests without lubricants and with lubricants, respectively. The lubricated surface has the

crater larger than the non-lubricated surface. In the center of imprints, the patterns were destroyed by the rotating balls. Scratches are observed on the contact surface area, and tiny grains are found and filled in the gap between WC grains due to the extrusions and cleavage. However, fewer scratches are found compared with the non-lubricated surface. Compared with the polished surface, fewer scratches are observed for both lubricated and non-lubricated cases. It is proved that the line-like patterns can improve the lubrication distribution and reduce the abrasion between the counterpart and the sample surface.

It is noticeable that the line-like patterns can reduce the crater size and wear rate under both lubricated and non-lubricated testing conditions, but it seems that the wear reduction is less pronounced under the lubricated conditions. The utilization of lubricant increases the wear rate for both the polished and patterned surfaces. However, with the patterns, the increasing of wear rate is still less remarkable than that of a polished surface. The patterns can improve the lubrication distribution and reduce the scratch appearances on the contact surfaces.

5.2 Tool testing for abrasive application

5.2.1 Experimental parameters

The tests aim to measure and assess the cutting ability of the produced structures on WC-CoNi hardmetal surfaces. The surface quality of the workpieces is inspected before and after the tests, and it is considered as an important indicator to assess the cutting quality of the new tool. The cutting force, i.e. the force coefficient, is another indicator to examine the cutting processes. The surface integrity assessment, i.e. wear of the surface structures is an indicator to evaluate the tool life. The tests are conducted on the workbench for abrasive machining processes (Figure 2-9 on Page 19). The test procedure includes four basic steps (Figure 5-10). At first, the tool and workpiece are placed to the initial position, and then slightly touch each other. During the machining processes, the workpiece rotates and oscillates at certain speed, meanwhile the tool moves towards to the rotating workpiece at certain feed. In the end, the tool and the workpiece are separated and move back to the initial positions. For each tool, TFCs are measured and obtained from ten repetitions under identical conditions.

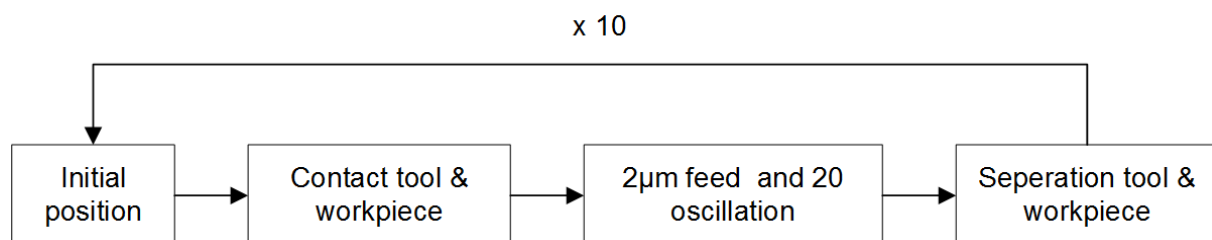


Figure 5-10. Flow chart of the test procedure

In order to compare different surface patterns, machining parameters and workbench configuration are kept identical (Table 5-13). Workpieces rotate at the speed of 500

rpm and oscillate at the speed of 1000 mm/min. Meanwhile, the tool moves with a stepping feed of 2 μm . The used lubricant Kadio50 has a kinematic viscosity ν of 5 mm^2/s at the temperature of 40°C. The flow rate of the lubricant is set to 0.07 Bar.

Table 5-13. Machining parameters and workbench configuration

Rotation speed (rpm)	Oscillation speed(mm/min)	Oscillation number	Feed(μm)	Flow rate(bar)	Lubricant viscosity (mm^2/s)	Temperature ($^{\circ}\text{C}$)
500	1000	20	2	0.07	5	30

The testing sample, made of WC-CoNi hardmetal with defined surface structures (hexagonal pyramids, Figure 5-11(a)), was tested. The honing stone B151/L2/10/50 (B151) was also tested as the reference sample (Figure 5-11(b)). The tests were carried out under the aforementioned machining conditions in Table 5-13. The honing stone has been dressed before the test to reveal the cutting edges. Both of the samples have the same dimension of $20 \times 3 \times 4.95 \text{ mm}^3$ (Figure 2-2 on Page 7). Their microstructural properties of the hardmetal tool and the honing stone B151 have been characterized and described in the previous chapters. Brief information is also given in Table 5-14. 343 pyramids with the mean surface area of $9.1 \times 10^3 \mu\text{m}^2$ are situated on the WC-CoNi hardmetal tool surface, and all the pyramids account for 5.2% of the tool surface. On the surface of the honing stone B151, in total 355 grains are found, and their mean surface area is $10.6 \times 10^3 \mu\text{m}^2$, which account for 8.9% of the entire tool surface. The CBN grains are distributed randomly, and their shapes can vary from circle to elongated, but most of them vary from rectangle to hexagon.

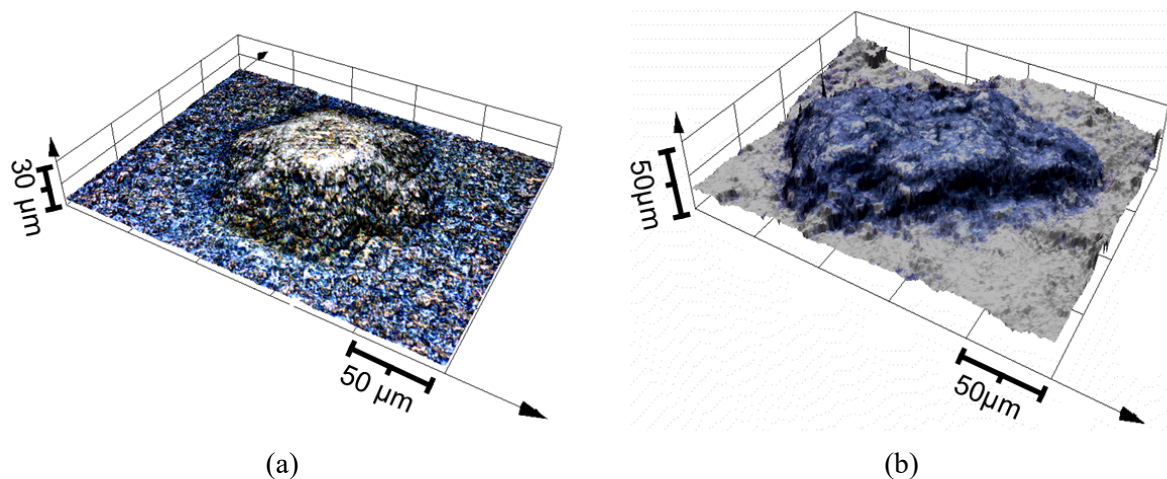


Figure 5-11. Profile of (a) one single hexagonal pyramid on the WC-CoNi hardmetal tool, (b) one single CBN grain on the honing stone B151 (images taken by LSM)

Table 5-14. Quantification of the hardmetal tool

Sample	Grain amount	Mean grain surface area (μm^2)	Phase ratio	Grain shape
Hardmetal tool	343	9.1×10^3	5.2%	Hexagon
B151	355	10.6×10^3	8.9%	Most varying from rectangle to hexagon

The workpieces have been fine turned before testing. Figures 5-12(a) and (b) show the surface inspection of the two workpieces after the fine turning. The strips were induced in the turning processes, and some cracks can also be detected. R_a , R_z and R_{max} are selected to describe the surface conditions of the workpieces and the roughness of the workpieces is given in Table 5-15. Workpiece 1 was machined by the honing stone B151 and Workpiece 2 was machined by the hardmetal tool.

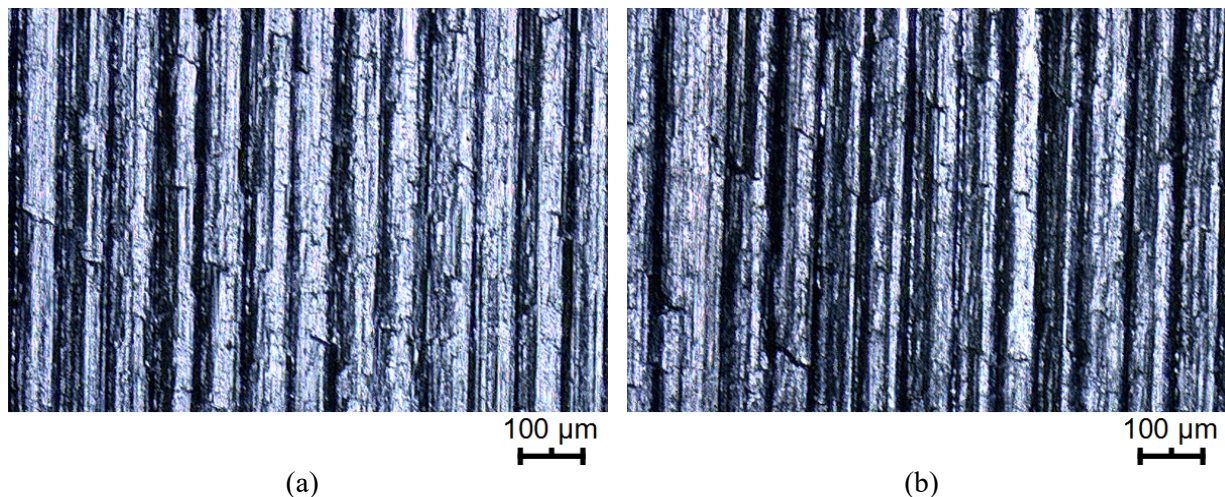


Figure 5-12. Surface characterization (LSM) and profiles of (a) workpiece 1, (b) workpiece 2

Table 5-15. Roughness measurements of workpiece 1 and workpiece 2 before testing

Workpiece	Corresponding tool	R_a (μm)	R_z (μm)	R_{max} (μm)
1	B151	3.2	17.7	24.4
2	Hardmetal	3.7	20.1	22.0

5.2.2 Testing results and discussion

The tool cutting quality can be assessed by the roughness measurement. Figure 5-13(a) and (b) show the surface characterization of the workpiece surfaces. Compared with Figures 5-12(a) and (b), the large strips and cracks have been removed and the workpiece surfaces became smooth, but Workpiece 2 is slightly rougher than Workpiece 1.

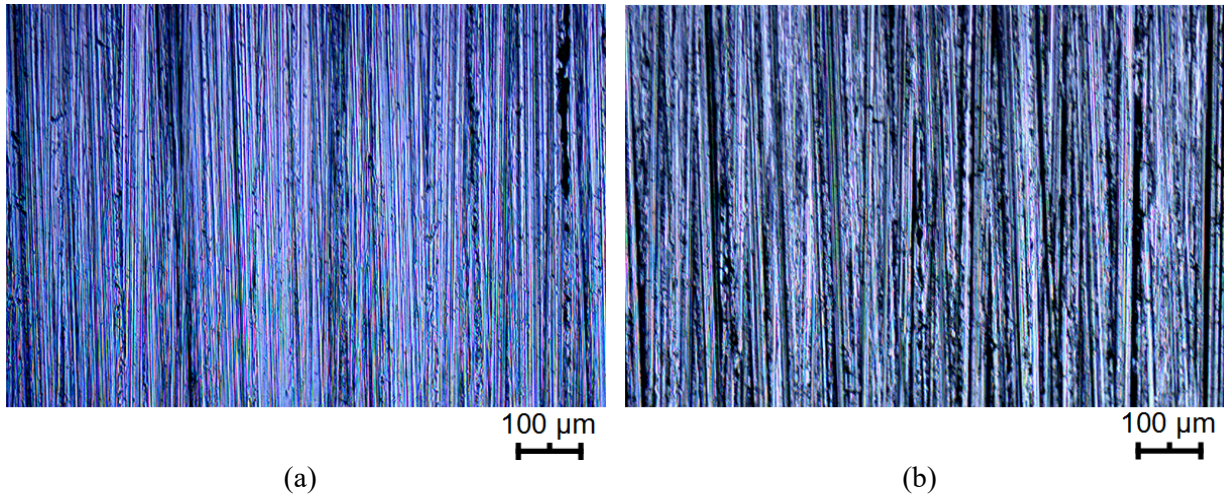


Figure 5-13. Surface characterizations after testing (LSM): (a) workpiece 1, (b) workpiece 2

Table 5-16 shows the roughness measurement results after the tests. R_a , R_z and R_{max} of Workpiece 1 are 0.4 μm , 3.4 μm and 6.1 μm , respectively. R_a , R_z and R_{max} of Workpiece 2 are 0.7 μm , 5.7 μm and 7.7 μm , respectively. Both of the two tools ameliorated the surface quality of the workpieces.

Table 5-16. Roughness measurement of workpiece 1 and workpiece 2 after testing

Workpiece	Corresponding tool	R_a (μm)	R_z (μm)	R_{max} (μm)
1	B151	0.4	3.4	6.1
2	Hardmetal	0.7	5.7	7.7

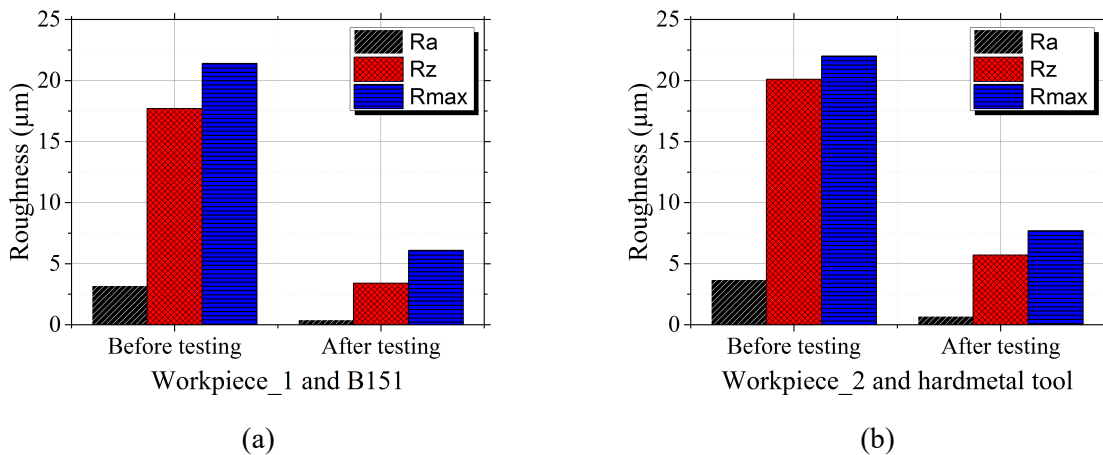


Figure 5-14. Roughness improvement of the workpieces: (a) Workpiece 1 machined by the honing stone B151, (b) Workpiece 2 machined by the hardmetal tool

Figure 5-14 shows the comparison of workpiece roughness, where R_a , R_z and R_{max} of Workpiece 1 have been improved of 87.5%, 80.7% and 75.0%, respectively, and those of Workpiece 2 have been improved of 81.1%, 71.6% and 65.0%, respectively. Although the roughness improvement by hardmetal tool is not as satisfactory as that by the honing stone B151, the improvement is still effective and obvious.

Cutting force analysis enables to understand the material removal mechanism of the cutting tools. Figure 5-15 shows the record of tool force signals of one test. The test lasted 42 s and included 20 wave profiles, corresponding to 20 times oscillations. Each oscillation lasted 2.1 s, corresponding to 17.5 rotations of the workpiece. During the test, three force components applied by the honing stone B151 on Workpiece 1 was relatively stable (Figure 5-15(a)), but F_n and F_t applied by the hardmetal tool on Workpiece 2 had a descent tendency (Figure 5-15(b)).

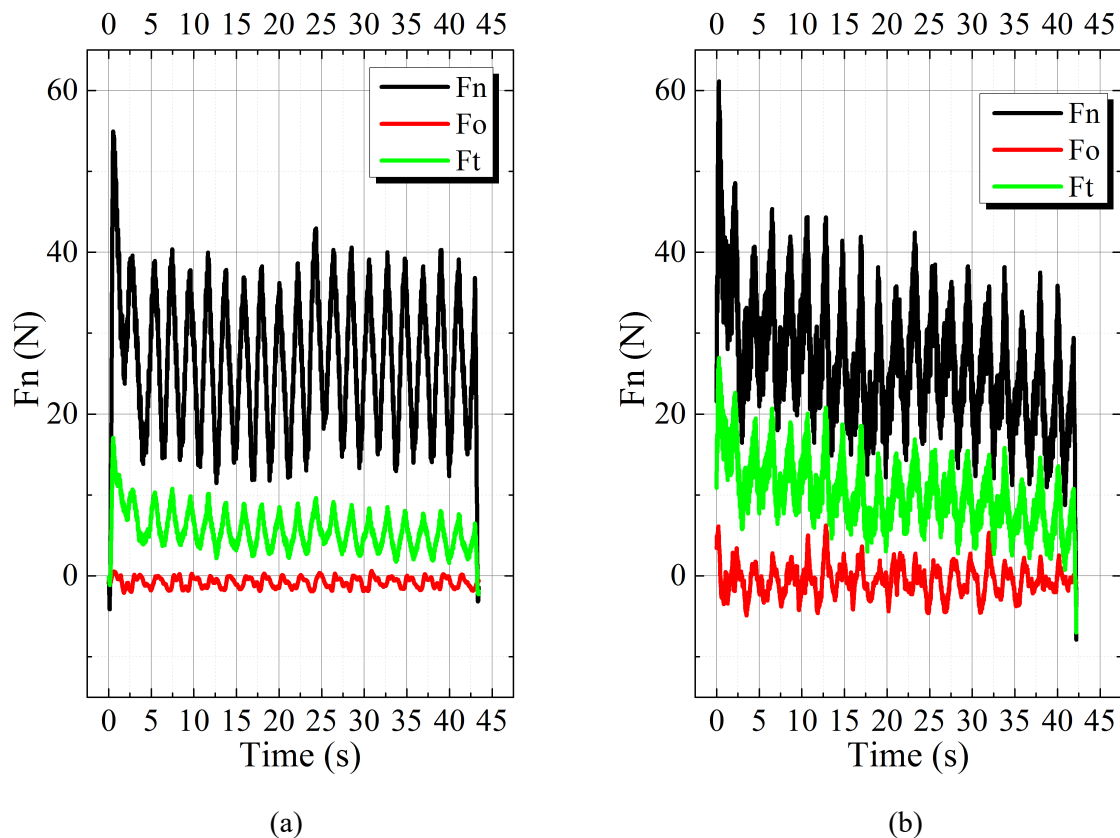


Figure 5-15. Cutting force signal record of one test: (a) workpiece 1 machined by the honing stone B151, (b) workpiece 2 machined by the hardmetal tool

The average values of the normal force F_n and the tangential force F_t as well as its ratio TFC for each repetition were obtained and plotted in Figure 5-16 for both cases:

- Case 1: Workpiece 1 machined by the honing stone B151;
- Case 2: Workpiece 2 machined by the hardmetal stone.

The force evolution of the two cases was different from each other: F_n and F_t fluctuated stably around 22.5 N and 3.5 N in Case 1, but in Case 2, F_n and F_t decreased dramatically in the first three repetitions then maintained a slight fluctuation at a low level. These observations can be explained by the wear mechanism of tools. The two basic components of honing stone (CBN grains and binder) had approximately the same wear speed in the tests, which ensured the continuous generation of new cutting edges. Therefore, the cutting layer could be macroscopically considered to maintain unchanged and cutting forces could then maintain stable during the whole tests.

However, the hexagonal pyramids on the hardmetal stone surface firstly suffered strong pressure due to the limited contact areas. The pyramids penetrated into the workpiece and removed a great amount of materials. As consequence of stepping feed and the wear of pyramids, the contact areas became larger, and the penetrations of pyramids became smaller. Large quantity of materials was removed at the first three repetitions and less material was removed in the following repetitions. Thus, small forces were recorded in the last repetitions in Case 2.

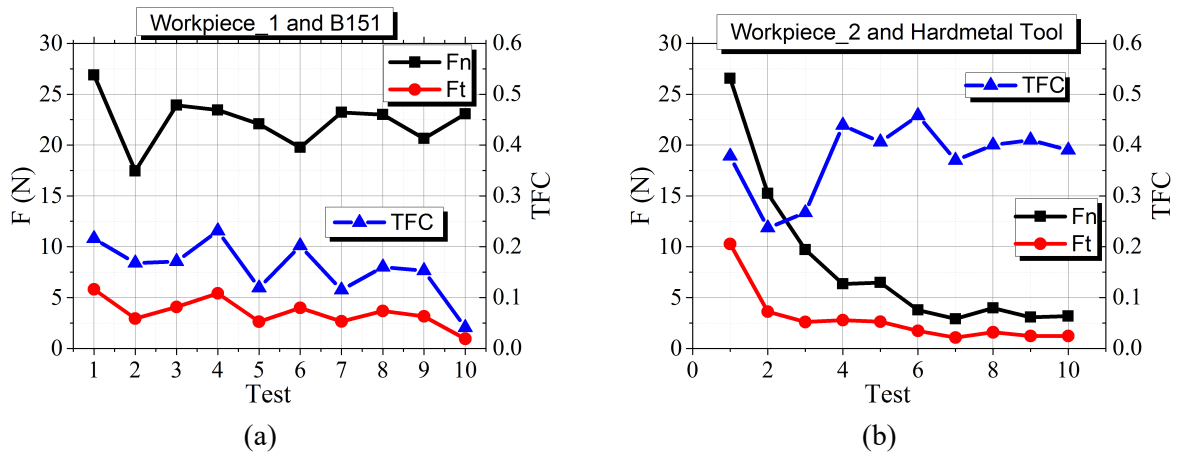


Figure 5-16. Cutting force and TFC evolution: (a) workpiece 1 machined by the honing stone B151, (b) workpiece 2 machined by the hardmetal tool

Table 5-17. TFCs obtained with different tools

Tests	TFC	Deviation
Workpiece_1 and B151	0.16	0.06
Workpiece_2 and Hardmetal	0.38	0.07

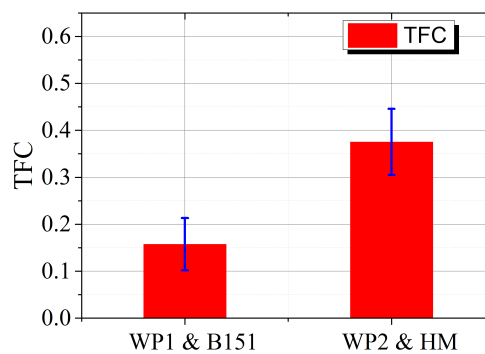


Figure 5-17. Comparison of TFC mean values

The TFCs were calculated and compared in Table 5-17 and Figure 5-17. In Case 1, TFCs were stable and fluctuated around 0.16. In Case 2, TFCs were not stable in the first three repetitions, but fluctuated around 0.38 in the following receptions. After the tests, the geometrical properties of the hexagonal pyramids have been measured using LSM in order to assess the tool wear. The surface topography was recon-

structured with the obtained coordination using the software Origin 9.0. The parameters mentioned in Figure 4-3(a) on Page 48 were measured on five different hexagonal pyramids. The obtained geometrical properties were compared with the ones before machining. Figure 5-18 shows the LSM and SEM images of the hexagonal pyramids. The hexagonal shape at the bottom of the pyramid can still be clearly distinguished, but the profile becomes blurred at the top and at the slopes. The observation suggests that the top platform was demolished during the machining processes; the wear of the pyramid began from the top and went deep as a consequence of the sliding against the workpiece.

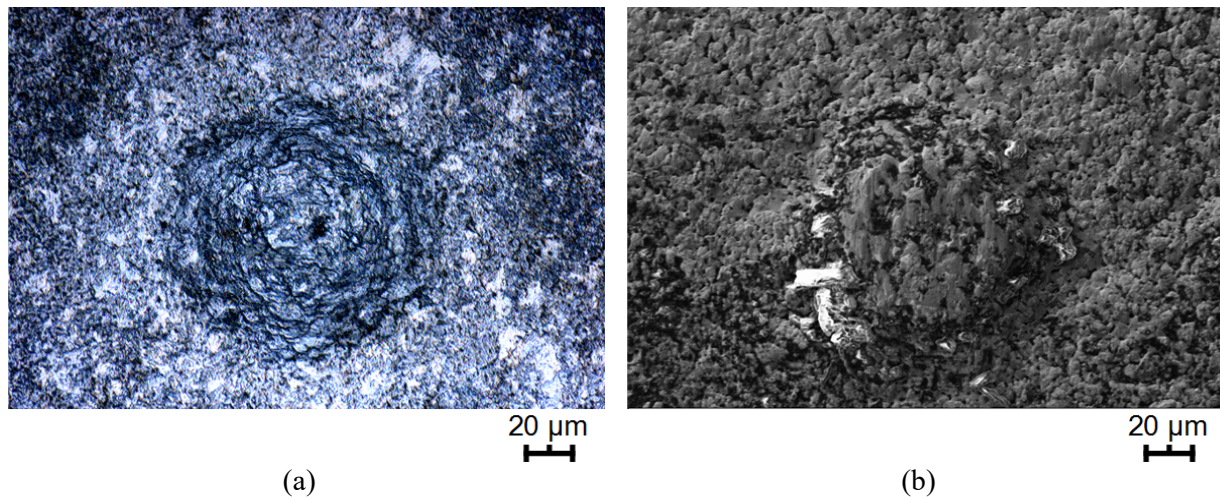


Figure 5-18. Hexagonal pyramids characterized by (a) LSM and (b) SEM after testing

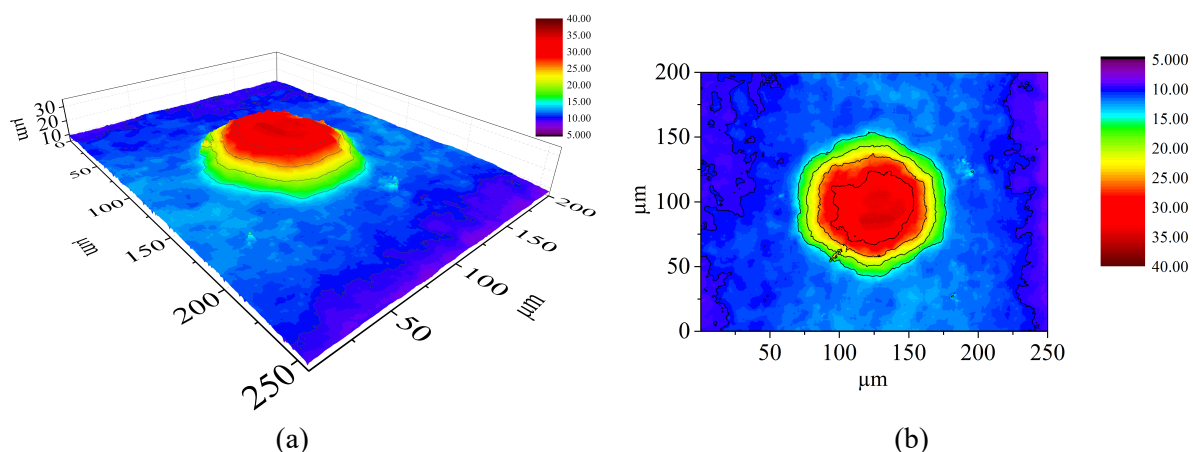


Figure 5-19. Pyramid reconstruction after machining using Origin 9.0: (a) reconstructed 3D model and (b) its projection

The surface coordination information obtained by LSM was recorded and exported to reconstruct the 3D model of the hexagonal pyramid. Figure 5-19 illustrates the reconstructed 3D model of a single pyramid and its projection. The contour lines and the corresponding colors indicate the profiles and the height of the pyramid. The 3D model proves the observation from the LSM and SEM image: the top of the pyramid suffered obvious damage but the hexagonal shape maintained unchanged at the bottom. The structure was gradually worn out from the top to the bottom. The 3D

model enables to precisely measure the geometrical properties of the pyramids, especially the slope angles at the positions A-A (bisector line) and B-B (diagonal line) by the cross-sectional measurements (Figure 5-20).

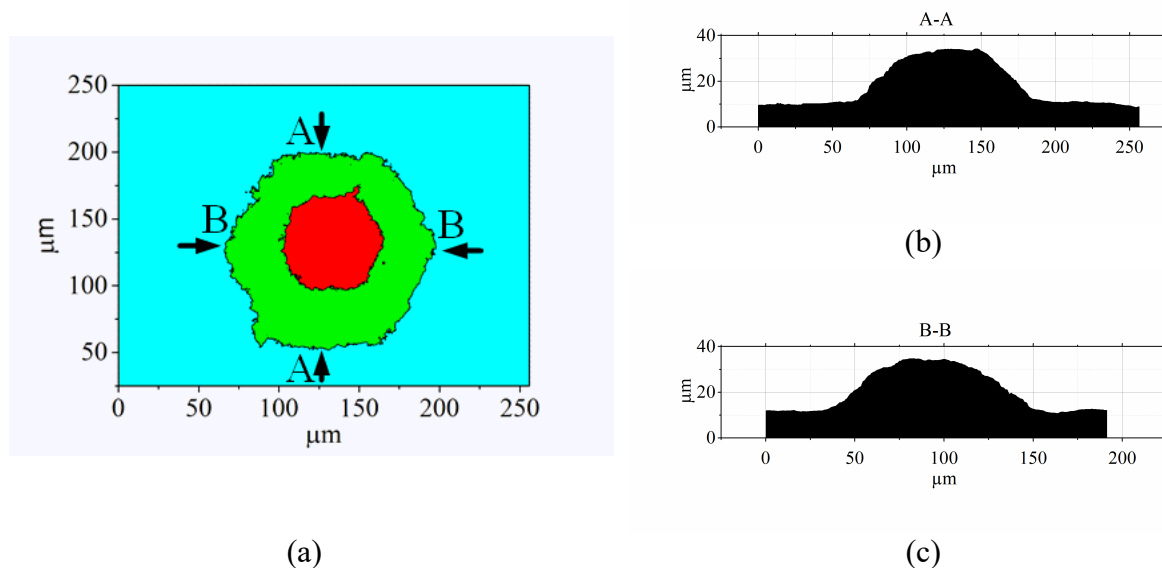


Figure 5-20. (a) Projection of a single hexagon pyramid, (b) and (c) cross-sections at position A-A and B-B, respectively

The measurement results are summarized in Table 5-18. The average side length a_1 at the top is $61.7 \mu\text{m}$, and the one at the bottom a_2 is $28.1 \mu\text{m}$. The surface area S_1 at the bottom is $9.1 \times 10^3 \mu\text{m}^2$ and S_2 at the top is $2.4 \times 10^3 \mu\text{m}^2$. The height h of the pyramid is $17.7 \mu\text{m}$ and the slope angles α and β are 24.8° and 27.4° , respectively.

Table 5-18. Summary of geometrical properties of the hexagonal pyramids after tests

N°	a_1 (μm)	a_2 (μm)	S_1 (μm^2)	S_2 (μm^2)	h (μm)	α ($^\circ$)	β ($^\circ$)
1	59.8	27.4	9407.8	2264.2	21.5	21.1	29.1
2	68.2	26.1	10899.7	2353.6	16.3	25.9	26.7
3	62.9	26.6	8218.6	2158.8	16.0	24.3	26.1
4	54.5	30.2	8718.7	3224.6	16.4	21.5	27.7
5	63.1	30.2	8360.4	1924.7	18.5	31.3	27.2
Average	61.7	28.1	9121.0	2385.2	17.7	24.8	27.4

Figure 5-21 and Table 5-19 show the comparison of the geometrical properties of the hexagonal pyramids before and after the tests. It is observed that the side length a_1 and a_2 are slightly changed (Figure 5-21(a)), indicating the slight deformation of the pyramids. The surface areas S_1 and S_2 at the pyramid bottom and top maintain approximately constant (Figure 5-21(b)), indicating the basic pyramid shape maintains generally unchanged. The slope angles α and β became slightly smaller also due to the deformation of the pyramids (Figure 5-21(c)). The height of the pyramid decreased about $3.9 \mu\text{m}$, corresponding to a wear speed of $1.1 \times 10^{-3} \mu\text{m}/r$, knowing the workpiece had the rotation of 3500 during the tests (Figure 5-21(d)).

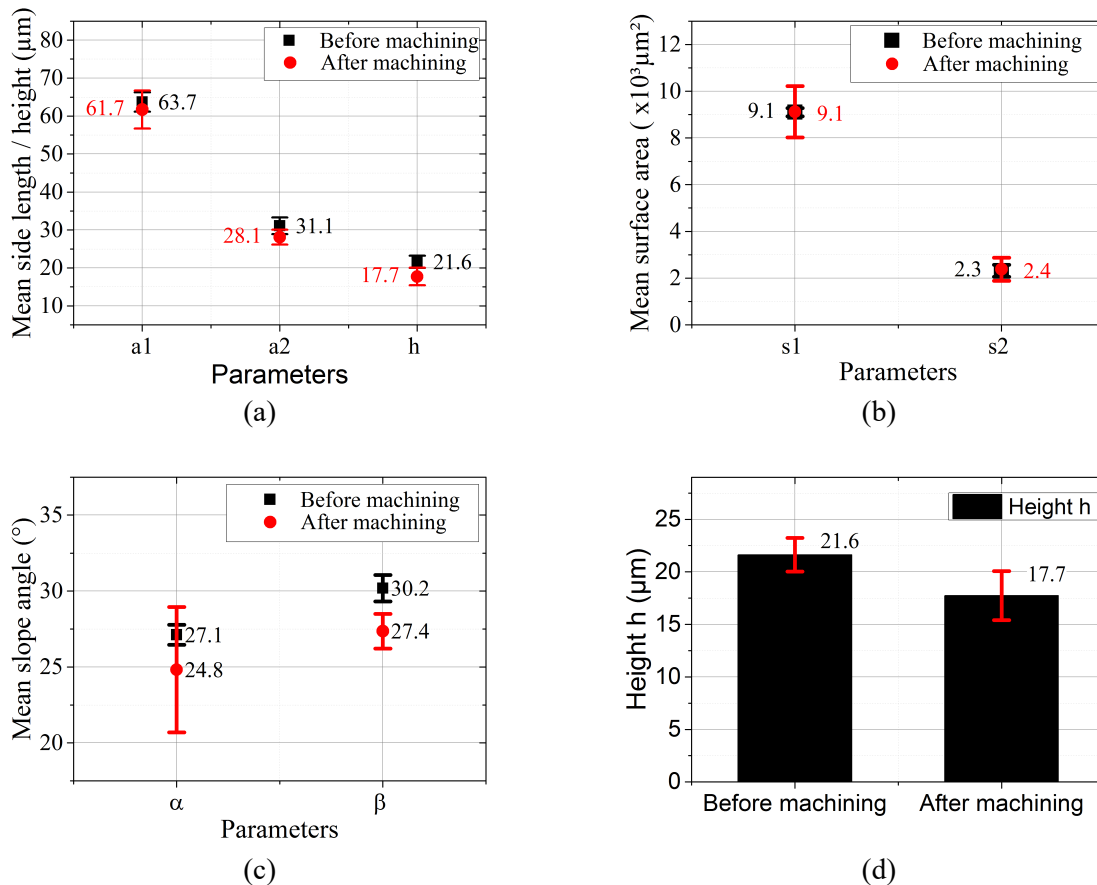


Figure 5-21. Comparison of the geometrical properties of the hexagonal pyramids before and after machining: (a) side lengths and height, (b) surface area, (c) slope angles and (d) height evolution

Table 5-19. Comparison of geometrical properties

Properties	a_1 (μm)	a_2 (μm)	S_1 ($\times 10^3 \mu\text{m}^2$)	S_2 ($\times 10^3 \mu\text{m}^2$)	h (μm)	α ($^\circ$)	β ($^\circ$)
Before testing	63.7	31.1	9.1	2.3	21.6	27.1	30.2
After testing	61.7	28.1	9.1	2.4	17.7	24.8	27.4

5.2.3 Noticeable observations

Tested under the same conditions on the workbench, the workpiece surface machined by the hardmetal tool with the hexagonal pyramids obtained similar surface quality compared to the one machined by the honing stone B151. The surface roughness obtained by the hardmetal tool is only slightly deviated from that obtained by the honing stone B151.

The cutting force analysis indicates that the cutting mechanisms of the two tools are quite different. For the honing stone B151, the grains and the binder have approximately identical wear rate, so they wear out at the same time due to their self-generating nature. Therefore, the removal of the material is rather stable and a stable cutting force is obtained during the whole machining processes. For the hardmetal tool, the pyramids remove a large quantity of materials and suffer great wear at the very beginning since the contact areas are quite small, but the wear becomes less important when the pyramids penetrate deeper. Therefore, the cutting force is rather

high at the beginning, then gradually diminishes and maintains at a weak level till the end of the tests.

The geometrical property measurements of the pyramids testify that the pyramids wear out gradually from the top to the bottom in the machining process. The shape of the pyramids maintain unchanged except for some slight deformation.

6 Conclusion and prospective work

In this study, the goal of designing and producing defined structures on WC-CoNi hardmetal surfaces for abrasive machining processes has been fulfilled. Two types of surface structures (concave and convex) were successfully produced on the WC-CoNi hardmetal surfaces using laser surface texturing, taking into account the following considerations:

- cemented carbide: it is produced by sintering, has adequate hardness and toughness, and is usually used as tool material for chip-removal machining processes but not for abrasive machining processes;
- defined structures: traditional abrasive tools don't possess regular surface structures, so the defined structures should be creatively produced on the tool surface, and their geometrical properties can be modified;
- tool: the produced structures should be useful or beneficial for tool applications as abrasive part for material removal or as wear resistant part for grinding assistance.

The study has been focused on three major aspects: abrasive tool characterization, tool surface modification and tool testing. The main achievements of this study can be summarized as follows:

- an effective approach has been developed to systematically and statistically quantify the surfaces of traditional abrasive tools, which is necessary to simulate their surface structures on WC-CoNi hardmetal surfaces;
- short/ultra-short pulse laser have been successfully used to produce defined surface structures, and high geometrical precision and good surface integrity have been achieved;
- it is proven that the concave structures on cemented carbide can improve the tribological performances, and the convex structures can efficiently remove materials, which could be potentially used as cutting tool.

The conclusion of the work is then made in these three aspects.

Abrasive tool characterization

The honing stones (CBN composites) have been characterized using 2D surface topography quantification and 3D volume characterization. The characterization protocols standardize the procedures from the sample preparation to the selection of analysis parameters, and the grain quantification.

For the CBN composite, two different honing stones B151 and B91 were characterized using LSM and digital image processing. Their quantitative, dimensional and form parameters have been analyzed, and positional properties of the CBN grains on the surface have also been described. 3D volume characterization of the honing stone B151 was carried out using CT scan and 3D modelling method. The quantity, dimension and shape of the grains in the volume were quantified. The obtained in-

formation of the 2D surface topography quantification was used for the surface topography design of the hardmetal tool surface.

The 2D characterization results meet in the mass the nominal information given by the producers, except that some slight deviations exist by the honing stone B91. It is recommended to use higher resolution to measure the B91 surface, acquire more precise images and avoid excessive image processing. Three-dimensional volume characterization enabled to get more precise grain quantification from a statistical point of view, but the grain shape characterization was limited due to the large data and the complicity of grain shape definitions. Compared to the 3D volume characterization, the 2D surface characterization still has many advantages: it needs much less time than 3D characterization and it has less implicit requirements to the equipment.

Tool surface modification

Laser beam machining was selected to modify the WC-CoNi hardmetal surface and produce surface structures. Short/ultra-short pulse laser beams were used in combination with LIMET, auto-stage and micromachining system in order to achieve high geometrical precision. Two major applications of the surface structures were determined. The concave structures were used in the tribological system to reduce the friction and the convex structures were used as abrasive tool to remove materials.

The laser-hardmetal reaction mechanism has been investigated in the work. It is proven that the thermal defects can be effectively avoided by changing the laser pulse duration. The hardmetal components can be selectively ablated by changing the fluence of the laser beams. The machining depth depends of the laser pulse number or laser machining time.

Three sorts of surface structures were produced for the tribological application: line-like patterns, dimples and grooves. Hexagonal pyramids and square pyramids were produced for the abrasive application as a simulation of the surface topography of the honing stone B151. Surface integrity assessment demonstrates that the produced structures have high geometrical precision on micrometer scale and match the design requirement. No evident thermal defects were induced by the laser beams except some ignorable defects in some cases.

LIMET was successfully used to produce interference structures on micrometer scale. The application of the auto-stage and micromachining system facilitates the motion control of the laser beams or the workpieces, and ameliorates the machining precision. It is proven that laser is a suitable machining method to simulate and reproduce the abrasive tool surface topography on the hardmetal surface.

Tool testing

The produced surface structures have been tested according to their applications. A workbench was designed and constructed with the concept of external honing processes in order to offer real testing environment. On the workbench, the friction test and abrasive test were standardized, and COFs and TFCs were obtained by force

measurements. Moreover, Calowear test and Nano-tribometer were also implemented to evaluate certain surface structures.

Regarding the tribological application, it is found that the dimples can effectively reduce the friction, but the line-like patterns are more capable to maintain the stability of the tribological system. Regarding the abrasive application, hexagonal pyramids efficiently removed the materials of the workpiece, and achieved similar surface quality as the honing stone B151 under the same machining conditions. The wear investigation of the pyramids shows that the structures could maintain the shape and have enough wear resistance in the machining processes.

The future work can be carried out from two aspects: deepen the research on the existing abrasive tools and extend the development of the functional tool surfaces, with the focus on the tool surface modification and tool application. On one hand, it is significant to improve the volume quantification method for CBN composites, especially to find out suitable mathematic algorithms to classify the grain shape and effectively describe the grain mutual positions in the studied volume. The method can be also implemented to characterize other abrasive tools such as those made of diamond, corundum etc. Taking into account that the resolution of CT scan might be not enough to analyze the grains with small size, other advanced image acquisition method could be necessary to use. On the other hand, it is interesting to investigate and measure the surface topography of the tool cutting surface using laser scanning microscopy. The reconstructed surface topography of the tool cutting surface can be used not only to understand the cutting mechanisms, but also to reproduce the cutting surface topography on the hardmetal surfaces using laser machining.

In this study, only one hardmetal grade has been studied, therefore, the future research work should cover other hardmetal grades regarding the composition and content. In this regard, it is interesting to quantitatively and systematically investigate the ablation of different hardmetal grades using ultra-short pulse, aiming to compose technical protocols covering different hardmetal grades. Moreover, important parameters of the laser, such as wavelength, pulse duration and fluence, are subject to vary in the research, aiming to optimize the laser-matter reaction and the surface integrity. In combination with micromachining system, it is possible to fabricate more complex surface structures on the hardmetal surfaces, even to reproduce the exact cutting surface topography of the abrasive tool, which can be measured using laser scanning microscopy. The main goal is to offer more texture types for the tribological and abrasive applications.

The produced surface textures should be assessed regarding their geometrical properties and surface integrity. The efficiency of the friction reduction or cutting ability of the produced structures should be quantitatively characterized. Based upon the tool testing results, the structures can be optimized by modifying the structural geometry for certain specific utilization.

References

- [1] H. K. Tönshoff, C. Arendt, and R. Ben Amor, "Cutting of hardened steel," *CIRP Ann. - Manuf. Tech-nol.*, vol. 49, no. 2, pp. 547–566, 2000.
- [2] S. N. Monteiro, A. L. D. Skury, M. G. de Azevedo, and G. S. Bobrovnitchii, "Cubic boron nitride competing with diamond as a super hard engineering material – an overview," *J. Mater. Res. Technol.*, vol. 2, no. 1, pp. 68–74, 2013.
- [3] R. H. Wentorf, "Synthesis of the cubic form of boron nitride," *J. Chem. Phys.*, vol. 34, no. 3, p. 809, 1961.
- [4] P. Loginov, L. Mishnaevsky, E. Levashov, and M. Petrzhik, "Diamond and cBN hybrid and nanomodified cutting tools with enhanced performance: Development, testing and modelling," *Mater Des*, vol. 88, pp. 310–319, 2015.
- [5] S. Saketi, S. Sveen, S. Gunnarsson, R. M'Saoubi, and M. Olsson, "Wear of a high cBN content PCBN cutting tool during hard milling of powder metallurgy cold work tool steels," *Wear*, vol. 332–333, pp. 752–761, 2015.
- [6] Y. Wang, K. Lei, Y. Ruan, and W. Dong, "Microstructure and wear resistance of c-BN/Ni–Cr–Ti composites prepared by spark plasma sintering," *Int. J. Refract. Met. Hard Mater.*, vol. 54, pp. 98–103, 2016.
- [7] VDI 3394-1980, Aufbau und Anwendung von Schleifkörpern mit Diamant und kubisch kristallinem Bornitrid (CBN) für die Metallbearbeitung (Arrangement and use of diamond and CBN grinding devices for metal working), Hrsg.vom Verein Deutscher Ingenieure Ausg.Düsseldorf, Germany, Juni 1980.
- [8] FEPA standard 64-1992, Shapes and dimension for diamond & CBN grinding wheels, Federation of European Producers of Abrasives, Paris, France, 1992
- [9] F. Gerhard, Grundlagen und Anwendungen des Honens (Fundamentals and applications of honing), Vulkan-Verl.,Essen, Germany, p.73.1992.
- [10] F. Klocke, W. König, Fertigungsverfahren 2: Schleifen, Honen, Läppen (Manufacturing processes 2: grinding, honing, lapping), Springer-Verlag, Berlin and Heidelberg, Germany, pp. 58-60, 2005.
- [11] T. A. Wolfe, T. J. Jewett, and R. P. Singh Gaur, "Powder synthesis," in *Comprehensive Hard Materials*, vol. 1, pp. 185–212, 2014.
- [12] B. Casas, U. Wiklund, S. Hogmark, and L. Llanes, "Adhesion and abrasive wear resistance of TiN deposited on electrical discharge machined WC-Co cemented carbides," *Wear*, vol. 265, no. 3–4, pp. 490–496, 2008.
- [13] H. E. Exner, "Physical and chemical nature of cemented carbides," *Int Met Rev*, vol. 24, no. 1, pp. 149–173, 1979.

- [14] J. Gurland, "New scientific approaches to development of tool materials," *Int Mater Rev*, vol. 33, no. 1, pp. 151–166, 1988.
- [15] K. Egashira, S. Hosono, S. Takemoto, and Y. Masao, "Fabrication and cutting performance of cemented tungsten carbide micro-cutting tools," *Precis Eng*, vol. 35, no. 4, pp. 547–553, 2011.
- [16] L. Llanes, B. Casas, E. Idanez, M. Marsal, and M. Anglada, "Surface integrity effects on the fracture resistance of electrical-discharge-machined WC-Co cemented carbides," *J Am Ceram Soc*, vol. 87, no. 9, pp. 1687–1693, 2004.
- [17] R. M. Saoubi, J. C. Outeiro, H. Chandrasekaran, O. W. D. Jr., and I. S. Jawahir, "A review of surface integrity in machining and its impact on functional performance and life of machined products," *Int J Sustain Manuf*, vol. 1, no. 1/2, pp. 203–236, 2008.
- [18] L. Llanes, E. Mart, E. Ida, B. Casas, and J. Esteve, "Influence of electrical discharge machining on the sliding contact response of cemented carbides," *Int J Refract Met Hard Mater*, vol. 19, pp. 35–40, 2001.
- [19] T. Balaud, Abrasive cutting tool characterization, Internship report, LFT, Saarland University, 2015.
- [20] S. N. Monteiro, A. L. D. Skury, M. G. de Azevedo, and G. S. Bobrovnitchii, "Cubic boron nitride competing with diamond as a super hard engineering material – an overview," *J. Mater. Res. Technol.*, vol. 2, no. 1, pp. 68–74, 2013.
- [21] A. McKie, J. Winzer, I. Sigalas, M. Herrmann, L. Weiler, J. Rödel, and N. Can, "Mechanical properties of cBN–Al composite materials," *Ceram. Int.*, vol. 37, no. 1, pp. 1–8, 2011.
- [22] T. Sugihara and T. Enomoto, "High speed machining of Inconel 718 focusing on tool surface topography of CBN tool," *Procedia Manuf.*, vol. 1, pp. 675–682, 2015.
- [23] G. Zhi, X. Li, W. Bi, J. Tang, and Y. Rong, "The measurement and analysis of micro bonding force for electroplated CBN grinding wheels based on response surface methodology," *Eng. Fail. Anal.*, vol. 57, pp. 377–388, 2015.
- [24] H. N. Li and D. Axinte, "Textured grinding wheels: a review," *Int J Mach Tools Manuf*, vol. 109, pp. 8–35, 2016.
- [25] G. Burkhard, F. Rehsteiner, and B. Schumacher, "High efficiency abrasive tool for honing," *CIRP Ann - Manuf Technol*, vol. 51, no. 1, pp. 271–274, 2002.
- [26] B. Kirsch and J. C. Aurich, "Influence of the macro-topography of grinding wheels on the cooling efficiency and the surface integrity," *Procedia CIRP*, vol. 13, pp. 8–12, 2014.

- [27] J. C. Aurich, P. Herzenstiel, H. Sudermann, and T. Magg, "High-performance dry grinding using a grinding wheel with a defined grain pattern," *CIRP Ann - Manuf Technol*, vol. 57, no. 1, pp. 357–362, 2008.
- [28] Y. Ichida, R. Sato, and H. Kajino, "Development of ultrafine-crystalline cbn abrasive grains for innovative grinding technology," in *Manufacturing Systems and Technologies for the New Frontier: the 41st CIRP Conference on Manufacturing Systems May 26--28, 2008, Tokyo, Japan*, M. Mitsuishi, K. Ueda, and F. Kimura, Eds. London: Springer London, pp. 463–466, 2008.
- [29] T. Dahmen, M. Engstler, C. Pauly, P. Trampert, N. de Jonge, F. Mücklich, and P. Slusallek, "Feature adaptive sampling for scanning electron microscopy," *Sci Rep*, vol. 6, p. 25350, May 2016.
- [30] P. Rossi, M. Engstler, and F. Mücklich, "Quantitative classification and assessment of Sr modification in hypoeutectic Al-Si and Al-Si-Mg alloys," *Pract Metallogr*, vol. 52, no. 10, pp. 571–589, Oct. 2015.
- [31] T. A. Mahmoud, J. Tamaki, and J. W. Yan, "Three-dimensional shape modeling of diamond abrasive grains measured by a scanning laser microscope," *Key Eng Mater*, vol. 238–239, pp. 131–136, 2003.
- [32] W. Kaplonek and K. Nadolny, "Laser methods based on an analysis of scattered light for automated, in-process inspection of machined surfaces: a review," *Optik (Stuttg)*, vol. 126, no. 20, pp. 2764–2770, 2015.
- [33] J. Xie, F. Wei, J. H. Zheng, J. Tamaki, and A. Kubo, "3D laser investigation on micron-scale grain protrusion topography of truncated diamond grinding wheel for precision grinding performance," *Int J Mach Tools Manuf*, vol. 51, no. 5, pp. 411–419, 2011.
- [34] M. Geiger, U. Popp, and U. Engel, "Excimer laser micro texturing of cold forging tool surfaces - influence on tool life," *CIRP Ann - Manuf Technol*, vol. 51, no. 1, pp. 231–234, 2002.
- [35] Etsion, "State of the art in laser surface texturing," *J Tribol*, vol. 127, no. 1, p. 248, 2005.
- [36] S. Jacobson and S. Hogmark, "Surface modifications in tribological contacts," *Wear*, vol. 266, no. 3–4, pp. 370–378, 2009.
- [37] J. Yang, F. Garcia Marro, T. Trifonov, M. Oden, M. P. Johansson-Joesaar, and L. Llanes, "Contact damage resistance of TiN-coated hardmetals: Beneficial effects associated with substrate grinding," *Surf Coatings Technol*, vol. 275, pp. 133–141, 2015.
- [38] J. Yang, M. Odén, M. P. Johansson-Jõesaar, and L. Llanes, "Influence of substrate microstructure and surface finish on cracking and delamination response of TiN-coated cemented carbides," *Wear*, vol. 352, pp. 102–111, 2016.

- [39] W. König, D. F. Dauw, G. Levy, and U. Panten, "EDM-future steps towards the machining of ceramics," *CIRP Ann - Manuf Technol*, vol. 37, no. 2, pp. 623–631, 1988.
- [40] A. M. Gadalla and W. Tsai, "Machining of WC–Co composites," *Mater Manuf Process*, vol. 4, no. 3, pp. 411–423, 1989.
- [41] M. P. Jahan, M. Rahman, and Y. S. Wong, "A review on the conventional and micro-electrodischarge machining of tungsten carbide," *International Journal of Machine Tools and Manufacture*, vol. 51, no. 12, pp. 837–858, 2011.
- [42] E. Lenz, E. Katz, W. König and R. Wertheim, "Cracking behavior of sintered carbides during EDM," *CIRP Ann - Manuf Technol*, vol. 24, pp. 109–114, 1975.
- [43] S. M. Pandit, K. P. Rajurkar, and M. C. Shaw, "Analysis of electro discharge machining of cemented carbides," *CIRP Ann - Manuf Technol*, vol. 30, no. 1, pp. 111–116, 1981.
- [44] L. Llanes, E. Mart, E. Ida, B. Casas, and J. Esteve, "Influence of electrical discharge machining on the sliding contact response of cemented carbides," *Int J Refract Met Hard Mater*, vol. 19, pp. 35–40, 2001.
- [45] T. Li, Q. Lou, J. Dong, Y. Wei, and J. Liu, "Selective removal of cobalt binder in surface ablation of tungsten carbide hardmetal with pulsed UV laser," *Surf Coatings Technol*, vol. 145, no. 1–3, pp. 16–23, 2001.
- [46] G. Dumitru, B. Lüscher, M. Krack, S. Bruneau, J. Hermann, and Y. Gerbig, "Laser processing of hardmetals: physical basics and applications," *Int J Refract Met Hard Mater*, vol. 23, no. 4–6 SPEC. ISS., pp. 278–286, 2005.
- [47] Z. Wu, J. Deng, Y. Xing, H. Cheng, and J. Zhao, "Effect of surface texturing on friction properties of WC/Co cemented carbide," *Mater Des*, vol. 41, pp. 142–149, 2012.
- [48] S. Fang, T. Herrmann, A. Rosenkranz, C. Gachot, F. G. Marro, F. Mücklich, L. Llanes, and D. Bähre, "Tribological performance of laser patterned cemented tungsten carbide parts," *Procedia CIRP*, vol. 42, no. Isem Xviii, pp. 439–443, 2016.
- [49] C. Momma, B. N. Chichkov, S. Nolte, F. von Alvensleben, A. Tünnermann, H. Welling, and B. Wellegehausen, "Short-pulse laser ablation of solid targets," *Opt Commun*, vol. 129, no. 1–2, pp. 134–142, 1996.
- [50] B. W. Geiger M, S. Roth, "Influence of laser-produced microstructures on the tribological behavior of ceramics," *Surf Coat Technol*, vol. 100, pp. 17–22, 1998.
- [51] G. Dumitru, V. Romano, H. P. Weber, H. Haefke, Y. Gerbig, and E. Pflüger, "Laser microstructuring of steel surfaces for tribological applications," *Appl Phys A Mater Sci Process*, vol. 70, no. 4, pp. 485–487, 2000.

- [52] O. Rashwan, Micro surface texturing for friction control, Dissertion, University of Windsor, 2013.
- [53] X. C. Wang, T. Laoui, J. Bonse, J. P. Kruth, B. Lauwers, and L. Froyen, "Direct selective laser sintering of hard metal powders: experimental study and simulation," *Int J Adv Manuf Technol*, vol. 19, no. 5, pp. 351–357, 2002.
- [54] D. Baeuerle, W. Dieter, Laser processing and chemistry. Springer Berlin Heidelberg, pp. 760-767, 2011.
- [55] T. Li, Q. Lou, J. Dong, Y. Wei, and J. Liu, "Modified surface morphology in surface ablation of cobalt-cemented tungsten carbide with pulsed UV laser radiation," *Appl Surf Sci*, vol. 172, no. 3–4, pp. 331–344, 2001.
- [56] T. Li, Q. Lou, J. Dong, Y. Wei, and J. Liu, "Phase transformation during surface ablation of cobalt-cemented tungsten carbide with pulsed UV laser," *Appl Phys A*, vol. 73, no. 3, pp. 391–397, 2001.
- [57] G. Dumitru, V. Romano, H. P. Weber, M. Sentis, and W. Marine, "Ablation of carbide materials with femtosecond pulses," *Appl Surf Sci*, vol. 205, no. 1–4, pp. 80–85, 2003.
- [58] B. N. Chichkov, C. Momma, S. Nolte, F. von Alvensleben, and a. Tuennermann, "Femtosecond, picosecond and nanosecond laser ablation of solids," *Appl Phys A Mater Sci Process*, vol. 63, no. 2, pp. 109–115, 1996.
- [59] M. Baucchio, ASM engineered materials reference book. Materials Park, OH: ASM International, 1994.
- [60] R. C. Weast, M. J. Astle, and C. R. Company., CRC Handbook of chemistry and physics: a ready-reference book of chemical and physical data. Ed. 62 (1981-1982) Ed. 62 (1981-1982). Cleveland, Ohio: CRC Press, 1981.
- [61] E. Saljé and M. von See, "Process-optimization in honing," *CIRP Ann - Manuf Technol*, vol. 36, no. 1, pp. 235–239, 1987.
- [62] H. W. Hoffmeister, B. Menze, "Einsatz von Sensorik beim Honen und Regelung von Honprozessen (Use of sensors for honing and control of honing process)," in *Jahrbuch Schleifen, Honen, Läppen und Polieren (Yearbook grinding, honing, lapping and polishing)*, 61. Ausgabe, Vulkan Verlag, Essen, Germany, 2004.
- [63] I. Marinescu, W. Rowe, B. Dimitrov, H. Ohmori, *Tribology of abrasive machining Processes*, William Andrew Publishing, Oxford, 2013.
- [64] B. K. Sharma and A. J. Stipanovic, "Development of a new oxidation stability test method for lubricating oils using high-pressure differential scanning calorimetry," *Thermochim Acta*, vol. 402, no. 1–2, pp. 1–18, 2003.

- [65] K. Dröder, H.-W. Hoffmeister, T. Große, M. Winter, C. Herrmann, "Untersuchungen zum Einsatz alternativer Kühlschmierstoffe beim Honen (Investigations on the use of alternative coolants in honing)," in *Jahrbuch Schleifen, Honen, Läppen und Polieren* (Year book: grinding, honing, lapping and polishing), 66. Ausgabe, Vulkan Verlag, Essen, Germany, pp. 343-349, 2013.
- [66] C. Schmitt and D. Bähre, "An approach to the calculation of process forces during the precision honing of small bores," *Procedia CIRP*, vol. 7, pp. 282–287, 2013.
- [67] J. A. Williams, "Wear and wear particles—some fundamentals," *Tribol Int*, vol. 38, no. 10, pp. 863–870, 2005.
- [68] M. Woldman, E. Van Der Heide, T. Tinga, and M. A. Masen, "The influence of abrasive body dimensions on single asperity wear," *Wear*, vol. 301, no. 1–2, pp. 76–81, 2013.
- [69] R. Nilsson, F. Svahn, and U. Olofsson, "Relating contact conditions to abrasive wear," *Wear*, vol. 261, no. 1, pp. 74–78, 2006.
- [70] R. C. Cozza, "Influence of the normal force, abrasive slurry concentration and abrasive wear modes on the coefficient of friction in ball-cratering wear tests," *Tribol Int*, vol. 70, pp. 52–62, 2014.
- [71] S. Yuan, W. Huang, and X. Wang, "Orientation effects of micro-grooves on sliding surfaces," *Tribol Int*, vol. 44, no. 9, pp. 1047–1054, 2011.
- [72] K. Steinhoff, W. Rasp, and O. Pawelski, "Development of deterministic-stochastic surface structures to improve the tribological conditions of sheet forming processes," *Journal of Materials Processing Technology*, vol. 60, no. 1–4, pp. 355–361, 1996.
- [73] U. Pettersson and S. Jacobson, "Friction and wear properties of micro textured DLC coated surfaces in boundary lubricated sliding," *Tribol Lett*, vol. 17, no. 3, pp. 553–559, 2004.
- [74] H. L. Costa and I. M. Hutchings, "Hydrodynamic lubrication of textured steel surfaces under reciprocating sliding conditions," *Tribol Int*, vol. 40, no. 8, pp. 1227–1238, 2007.
- [75] N. P. Suh, M. Mosleh, and P. S. Howard, "Control of friction," *Wear*, vol. 175, no. 1–2, pp. 151–158, 1994.
- [76] D. Bähre, S. Fang, J. Gliche, and K. Trapp, "Set-up of a test bench for the investigation of single parameter effects in abrasive processes by force measurements," *Adv Mater Res*, vol. 1052, pp. 441–446, 2014.
- [77] *A4i Micro/Quant Benutzerhandbuch (a4i Micro/Quant User Guide)*, Aquinto AG, Berlin, p.48, 2003.

- [78] Malvern Instruments Ltd, "A basic guide to particle characterization," Inf. White Pap., pp.1–26, 2012.
- [79] E. Olson, "Particle shape factors and their use in image analysis – Part 1 : Theory," J. GXP Compliance, vol. 15, no. 3, pp. 85–96, 2011.
- [80] L. R. Feret, "La Grosseur Des Grains Des Matières Pulvérulentes (Particle size of pulverulent materials)", congress in Zurich, Assoc. Internat. pour l'Essai des Mat. (International Association for the Testing of Materials), vol. 2, p.428, 1931.
- [81] W. H. Walton, "Feret's statistical diameter as a measure of particle size," Nature, vol. 162, pp. 329–330, 1948.
- [82] E. E. Underwood, "Stereology, or the quantitative evaluation of microstructures," J. Microsc., vol. 89, no.2, November 1968, pp. 161–180, 1969.
- [83] P. E. Danielson, "A new shape factor," Comput. Graph. Image Process, vol. 7, no. 2, pp. 292–299, Apr. 1978.
- [84] H. G. Merkus, Particle size measurements: fundamentals, practice, quality, Springer, New Your, vol. 17, pp.28-34, 2009.
- [85] F. Akbaripanah, F. Fereshteh-Saniee, R. Mahmudi, and H. K. Kim, "Microstructural homogeneity, texture, tensile and shear behavior of AM60 magnesium alloy produced by extrusion and equal channel angular pressing," Mater. Des., vol. 43, pp. 31–39, 2013.
- [86] L. Ceriani and P. Verme, "The origins of the Gini index: extracts from Variabilità e Mutabilità by Corrado Gini," J. Econ. Inequal., vol. 10, no. 3, pp. 421–443, 2012.
- [87] P. Rossi, M. Engstler, and F. Mücklich, "Homogeneity quantification method and its application to microstructure assessment," Practical Metallography, vol. 51, No. 3, pp. 180-199, 2014.
- [88] J. L. Gastwirth, "The estimation of the Lorenz curve and Gini Index," Rev. Econ. Stat., vol. 54, no. 3, pp. 306–316, 1972.
- [89] M. Novak and S. Deepak, "comparing 3d optical microscopy techniques for metrology applications," Bruker Nano Surfaces Div. Appl. Note, 2013.
- [90] A. Velichko, M. Engstler, C. Selzner, and F. Mücklich, "3D quantitative characterization of local structure and properties of contact materials," Mater Res Soc Symp Proc, vol. 1184, pp. 145–150, 2009.
- [91] J. Ohser, F. Mücklich, Statistical analysis of microstructures in materials science, John Willey & Sons, Chichester, New York, 2000.

- [92] J. Ohser, W. Nagel, and K. Schladitz, "The euler number of discretised sets – surprising results in three dimensions," *Image Anal & Stereol*, Vol. 22, No 1, pp.11-19, 2011.
- [93] A. Velichko, C. Holzapfel, A. Siefers, K. Schladitz, and F. Mücklich, "Unambiguous classification of complex microstructures by their three-dimensional parameters applied to graphite in cast iron," *Acta Mater*, vol. 56, no. 9, pp. 1981–1990, 2008.
- [94] D. Stoyan, W. S. Kendall, J. Mecke, *Stochastic geometry and its applications*. J. Wiley & Sons, Chichester, New York, p.436, 1995.
- [95] T. Zingg, "Beitrag zur Schotteranalyse (Contribution to the gravel analysis)," *Schweizerische Mineralogische Petrogr Mitteilungen*, vol. 15, pp. 39–140, 1935.
- [96] I. Vecchio, K. Schladitz, M. Godehardt, and M. J. Heneka, "3D Geometric Characterization of Particles Applied To Technical Cleanliness," *Image Anal Stereol*, vol. 31, no. 3, pp. 163–174, 2012.
- [97] F. Mücklich, A. Lasagni, and C. Daniel, "Laser interference metallurgy—periodic surface patterning and formation of intermetallics," *Intermetallics*, vol. 13, no. 3–4, pp. 437–442, 2005.
- [98] M. Duarte, A. Lasagni, R. Giovanelli, J. Narciso, E. Louis, and F. Mücklich, "Increasing lubricant film lifetime by grooving periodical patterns using laser interference metallurgy," *Adv Eng Mater*, vol. 10, no. 6, pp. 554–558, 2008.
- [99] S. Fang, L. Llanes, M. Engstler, D. Baehre, F. Soldera, F. Muecklich, "surface topography quantification of super hard abrasive tools by laser scanning microscopy," *Materials Performance and Characterization*, vol.5, pp.1–20, 2016.
- [100] M. Field, J. F. Kahles, "The surface integrity of machined and ground high strength steels," *DMIC Report 210*, pp. 54-77, 1964.
- [101] E. P. DeGarmo, *Materials and processes in manufacturing*. Hoboken, N.J.: Wiley, 2003.
- [102] L. Llanes, E. Mart, E. Ida, B. Casas, and J. Esteve, "Influence of electrical discharge machining on the sliding contact response of cemented carbides," *Int J Refract Met Hard Mater*, vol. 19, pp. 35–40, 2001.
- [103] M. D'Alessandria and F. Mücklich, "Tailoring the chemical behavior of aluminum for selective etching by laser interference metallurgy," *Appl Phys A*, vol. 98, no. 2, pp. 311–320, 2009.
- [104] D. Bäuerle, W. Dieter, *Laser processing and chemistry*, Springer Berlin Heidelberg, pp. 279–313, 2011.
- [105] J. Bonse, J. Krüger, S. Höhm, and A. Rosenfeld, "Femtosecond laser-induced periodic surface structures," *J Laser Appl*, vol. 24, no. 4, p. 42006, 2012.

- [106] J. Bonse, A. Rosenfeld, and J. Krüger, "On the role of surface plasmon polaritons in the formation of laser-induced periodic surface structures upon irradiation of silicon by femtosecond-laser pulses," *J Appl Phys*, vol. 106, no. 10, 2009.
- [107] K. Okamuro, M. Hashida, Y. Miyasaka, Y. Ikuta, S. Tokita, and S. Sakabe, "Laser fluence dependence of periodic grating structures formed on metal surfaces under femtosecond laser pulse irradiation," *Phys Rev B - Condens Matter Mater Phys*, vol. 82, no. 16, pp. 1–5, 2010.
- [108] D.B. Hamilton, J.A Walowit, C.M. Allen, "A theory of lubrication by micro irregularities," *Wear*, vol. 10, no. 5, p. 412, Sep. 1967.
- [109] M. Nakano, A. Korenaga, A. Korenaga, K. Miyake, T. Murakami, Y. Ando, H. Usami, and S. Sasaki, "Applying micro-texture to cast iron surfaces to reduce the friction coefficient under lubricated conditions," *Tribol Lett*, vol. 28, no. 2, pp. 131–137, 2007.
- [110] X. Wang, W. Liu, F. Zhou, and D. Zhu, "Preliminary investigation of the effect of dimple size on friction in line contacts," *Tribol Int*, vol. 42, no. 7, pp. 1118–1123, 2009.
- [111] F. Meng, R. Zhou, T. Davis, J. Cao, Q. J. Wang, D. Hua, and J. Liu, "Study on effect of dimples on friction of parallel surfaces under different sliding conditions," *Appl Surf Sci*, vol. 256, no. 9, pp. 2863–2875, 2010.
- [112] M. Stafe, A. Marcu, and N. N. Puscas, *Pulsed Laser Ablation of Solids*. Springer Berlin Heidelberg, pp.17-21, 2014.
- [113] N. B. Dahotre, "Laser Surface Engineering," *Advanced Materials and Processes*, vol. 160, no. 7. pp. 35–39, 2002.